SUBSIDIARY FAULT KINEMATICS AND DISPLACEMENT TRANSFER AT THE MILL CREEK-MISSION CREEK FAULT STEPOVER, SAN BERNARDINO MOUNTAINS, CALIFORNIA

A Thesis

by

DANIEL FERNANDO ELIZONDO UGARTE

Submitted to the Office of Graduate and Professional Studies of
Texas A&M University
in partial fulfillment of the requirements for the degree of

MASTER OF SCIENCE

Chair of Committee,	Judith S. Chester
Committee Members,	Luciana R. Barroso
	Fredrick M. Chester
	Carlos A. Dengo
Head of Department,	Michael C. Pope

December 2016

Major Subject: Geology

Copyright 2016 Daniel Fernando Elizondo Ugarte

ABSTRACT

The geometry of principal slip zones and the structures of their damage zones can affect earthquake nucleation, propagation, and arrest. Geometric irregularities, such as bends and segmented faults (stepovers), can modify the far-field stress state locally, both on and off principal slip surfaces, and promote or inhibit rupture though these complexities. The broad, multi-fault system of complex kinematics that is the San Gorgonio Pass region in Southern California represents a perfect area to study earthquake rupture through geometrically complex regions. The objective of this study is to characterize the surface, brittle deformation within the damage zone of the Mill creek fault in order to better understand the role that this fault has played in accommodating the overall right-lateral shear along the San Andreas system within the San Bernardino Mountains.

This study identified three deformation events on the basis of fault fabrics and cross-cutting relationships. The earliest deformation is associated with movement along the Mill Creek fault from straight segments into a restraining bend. A younger deformation event relates to the development of right-lateral oblique-normal transfer faults, which is recorded by the overprinting of epidote-mineralized faults by iron-oxide stained faults associated with the formation and movement along those faults. The youngest deformation event consists of reactivation of subsidiary faults due to shortening associated with the steep topography and mass wasting processes during rapid uplift and exhumation.

The subsidiary fault fabric of the damage zone of the Mill Creek fault indicates that the trend of the maximum principal compressive stress is oriented at a relatively low angle to the fault trace. This observation contrasts to that of other faults in the San Andreas system which document large angles to the main fault. This may indicate that the Mill Creek fault operated at a higher apparent friction than the other faults.

The restraining bend of the Mill Creek fault modifies the local stress state such that the maximum principal compressive stress steepens from nearly horizontal to approximately a 45° plunge to the NW as the bend is approached. These observations imply a significant component of 3D deformation when compared to a similar-shaped, but relatively isolated, fault-bend along the North Branch San Gabriel fault.

DEDICATION

This thesis is dedicated to my loving parents. They have been able and willing to provide me with financial, moral, and spiritual support since the day I started on this journey. The sacrifices they have made for myself and my siblings cannot be thanked enough with words. And with the same joy I started this journey, I commence the next one.

ACKNOWLEDGEMENTS

I would like to thank my committee chair, Dr. J. Chester, for her unwavering diligence in teaching and advising. Her philosophical research approach has helped me develop as a scientist and her advise has had impact in other areas of my life as well as academic. Also, I want to thank committee members, Dr. F. Chester, Dr. C. Dengo, and Dr. L. Barroso for their time and feedback throughout the course of this research.

I am grateful to my friends and diligent field assistants, Jake Hervey and Ivan Maulana, for committing to provide company during my time in the field. My research wouldn't have been possible without them. I would also like to thank Alex Morlean and Dr. Mike Oskin from the University of California at Davis for sharing their ideas and offering invaluable assistance in the field. Also, thanks to my best friend Ivan Vazquez for his encouragement during hard times. His motivation towards his own goals is admirable, but even more is his willingness to help others.

Thanks also go to my friends, colleagues, and the department faculty and staff for making my time at Texas A&M University a great experience.

CONTRIBUTORS AND FUNDING SOURCES

Contributors

This work was supported by a thesis committee consisting of Professor Dr. J. Chester [advisor], Dr. F. Chester, and Dr. C. Dengo of the Department of Geology and Geophysics and Dr. L. Barroso of the Department of Civil Engineering.

Collection of a significant portion of the data analyzed in Section 4 was made possible with the help of field assistants Jake Hervey and Ivan Maulana. Also, our University of California at Davis colleagues, Dr. M. Oskin and Alex Morelan, helped us tremendously by sharing their ideas and offering invaluable assistance in the field. A significant portion of the data presented in this thesis would not have been possible to collect without them.

All work for the thesis was completed by the student, in collaboration with Dr. J. Chester of the Department of Geology and Geophysics.

Funding Sources

This work was made possible in part by the Southern California Earthquake Center (SCEC), National Science Foundation, and United States Geological Society under SCEC awards #16263, 15202, and 14135.

NOMENCLATURE

SGP	San Gorgonio Pass
SCEC	Southern California Earthquake Center
SFSA	Special Fault Study Area
MCF	Mill Creek Fault
MiCF	Mission Creek Fault
GPF	Galena Peak Fault
MCC	Mill Creek Canyon
BC	Banning Canyon
RWF	Raywood Flat
YR	Yucaipa Ridge

TABLE OF CONTENTS

Page

ABSTRACT ii

DEDICATION iv

ACKNOWLEDGEMENTS v

CONTRIBUTORS AND FUNDING SOURCES vi

NOMENCLATURE vii

TABLE OF CONTENTS viii

LIST OF FIGURES x

LIST OF TABLES xii

1. INTRODUCTION 1

2. BACKGROUND 5

2.1. Fault Zones Structure 5
2.2. Modeling of Earthquake Rupture through Geometrically Complex Fault Systems 9
2.3. Geology of the San Gorgonio Pass Region 11

3. METHOD OF STUDY 21

3.1. Field Observations and Data Collection 21
3.2. Data Analysis 24

4. RESULTS 26

4.1. Major Faults and Lithology 26
4.2. Mesoscale Structure of Major Faults 31
4.3. Mesoscale Subsidiary Fault Fabrics 40
4.4. Distribution of Mineral-filled Subsidiary Faults 52

5. DISCUSSION 56

5.1. Deformation and Stress Along the Mill Creek and Galena Peak Faults 59
5.2. The Role of Fault Geometry on Stress and Strain in the Damage Zone 63
5.3. Effects on the Subsidiary Fault Fabric 66
5.4. Comparison to Other Fault Zone Studies 73
5.5. Displacement Transfer on the Mill Creek – Mission Creek Stepover 75
5.6. Implications to Future Earthquake Rupture Modeling and Seismic Hazard .79

6. SUMMARY AND CONCLUSIONS 81

REFERENCES 84

APPENDIX A 101

APPENDIX B 121

LIST OF FIGURES

Page

Fig. 1. Geologic map of San Gorgonio Pass that shows the major faults of the San Andreas system within this region, and distribution of four major crystalline basement terrains. 3

Fig. 2. Simplified block diagram illustrating the different structural domains often found in a mature strike-slip fault 6

Fig. 3. Geometry of different faults within the San Andreas fault system....8

Fig. 4. Right-lateral slip rate along the surface trace of the San Andreas fault along a 180 km traverse south from Cajon Pass 13

Fig. 5. Regional cross section through San Gorgonio Pass. Bold numbers represent Helium ages, and suggest rapid uplift in Yucaipa Ridge relative to the surrounding structural blocks....15

Fig. 6. Estimates of activity and displacement magnitudes on faults within the San Bernardino Mountains and surrounding areas. 16

Fig. 7. Fault map within the San Gorgonio Pass "structural knot" 19

Fig. 8. Diagram of the different regions of the study area 23

Fig. 9. Topographic map of the study area showing the major fault traces 29

Fig. 10. View perpendicular to strike of the Mill Creek fault damage zone....30

Fig. 11. View parallel to strike of the Mill Creek fault core and damage zone 32

Fig. 12. Second view parallel to strike of the Mill Creek fault core and damage zone....33

Fig. 13. Outcrop photographs of other fault exposures in the Raywood Flat region 34

Fig. 14. View parallel to the strike of the Transfer fault core and damage zone 37

Fig. 15. Outcrop photograph of subsidiary faults....41

Fig. 16. Additional outcrop photograph of subsidiary faults 42

Fig. 17. Subsidiary fault orientations and kinematics in the Mill Creek canyon region 43

Fig. 18. Subsidiary fault orientations and kinematics in the Yucaipa Ridge region 49

Fig. 19. Subsidiary fault orientations and kinematics in the Raywood Flat region 50

Fig. 20. Distribution of mineral-coated subsidiary faults in the Mill Creek canyon region 53

Fig. 21. Overprinting relationships in the Mill Creek canyon region 54

Fig. 22. Synoptic diagram example of a fabric distribution 57

Fig. 23. Synoptic diagram of the subsidiary fault orientations and kinematics in the Mill Creek Canyon region 58

Fig. 24. Map view and schematic cross sections perpendicular to the Mill Creek fault in Mill Creek canyon 67

Fig. 25. Map of the Brawley and Imperial faults in Imperial Valley, southern California 77

Fig. 26. Schematic diagram of a horsetail splay on a right-lateral fault 78

LIST OF TABLES

Page

Table 1. Outcrop size, lithology, and measurements by structural domain in the Mill Creek canyon region 27

Table 2. Rock type and thickness of fault core exposures by structural domain in the study area 38

Table 3. Outcrop size and measurements by structural domain in the Raywood Flat and Yucaipa Ridge regions 39

1. INTRODUCTION

Large displacement, plate boundary faults are complex systems often composed of multiple principal slip zones that have straight, curved, and segmented patches (e.g., Crowell, 1979; Sylvester, 1988; Norris and Cooper, 2001). The principal slip zones are bounded by damaged host rock that documents the cumulative inelastic response to displacement across the entire system (e.g., Wallace and Morris, 1986; Cowie and Scholz, 1992; Chester et al., 1993; Little, 1995; Vermilye and Scholz, 1998; Wilson et al., 2003; Dor et al., 2006; Mitchell and Faulkner, 2009; Bistacchi et al., 2010; Smith et al., 2013). The geometry of principal slip zones and the structures in their damage zones can affect earthquake nucleation, propagation, and arrest (e.g., King and Nabelek, 1985; Acharya, 1997; Duan and Day, 2008; Lozos et al., 2011). Geometric irregularities, such as bends and segmented faults (stepovers), can modify the far-field stress state locally, both on and off principal slip surfaces, and promote or inhibit rupture through these complexities. For instance, the normal stress on a fault surface in a restraining bend may increase (e.g., King and Nabelek, 1985; Acharya, 1997), enhancing off-fault fracture, which in turn can reduce the shear strength and increase the compliance of the damage zone (Lyakhovsky et al., 1997; Finzi and Langer, 2012). This damage can help dissipate energy from the principal zone slowing or stopping rupture propagation; but it also can provide the pathway for segment linkage in a large magnitude, multi-fault-segment rupture as recently demonstrated by the El-Mayor-Cucapah M_w 7.2 earthquake (Fletcher et al., 2014). Rupture propagation through a stepover can lead to a combination of processes, including decreased slip on the principal faults, formation of and movement

on new faults, uplift, folding, and distributed shear (e.g., Wakabayashi et al., 2004). Through these processes, slip can be transferred from one principal fault to the next through a series of newly-formed linking structures located between the bounding principal slip zones (McClay and Bonora, 2001; Mitra and Paul, 2011; Cooke et al., 2013; Hatem et al., 2015).

The southern San Andreas fault within the San Gorgonio Pass region of the San Bernardino Mountains is an example of a broad, multi-fault system with strike-slip, oblique-slip, and dip-slip kinematics, and notably is referred to as a structural or tectonic knot (Fig.1; Allen, 1957; Matti et al., 1992a; Matti and Morton, 1993; Spotila et al., 2001; Yule and Sieh, 2003; Langenheim et al., 2005; Yule, 2009). This area has long received attention because of the documented multi-strand character at the surface, poor definition of fault geometry and kinematics at depth (Rasmussen and Reeder, 1986; Jones, 1988; Seeber and Armbruster, 1995; Magistrale and Sanders, 1996; Yule and Sieh, 2003), significant slip-deficit (Spinler et al., 2010; Cooke and Dair, 2011; Zeng and Shen, 2014; McGill et al., 2015), and high hazard potential due to proximity to a large population center. The Mill Creek fault defines the northern boundary of this region.

The overall objective of this study is to characterize the near-surface, brittle deformation within the damage zone of the Mill Creek fault in order to better understand the role that this fault has played in accommodating the overall right-lateral shear along the San Andreas system within the San Bernardino Mountains. An additional important objective is to document the character of deformation in a geometrically complex

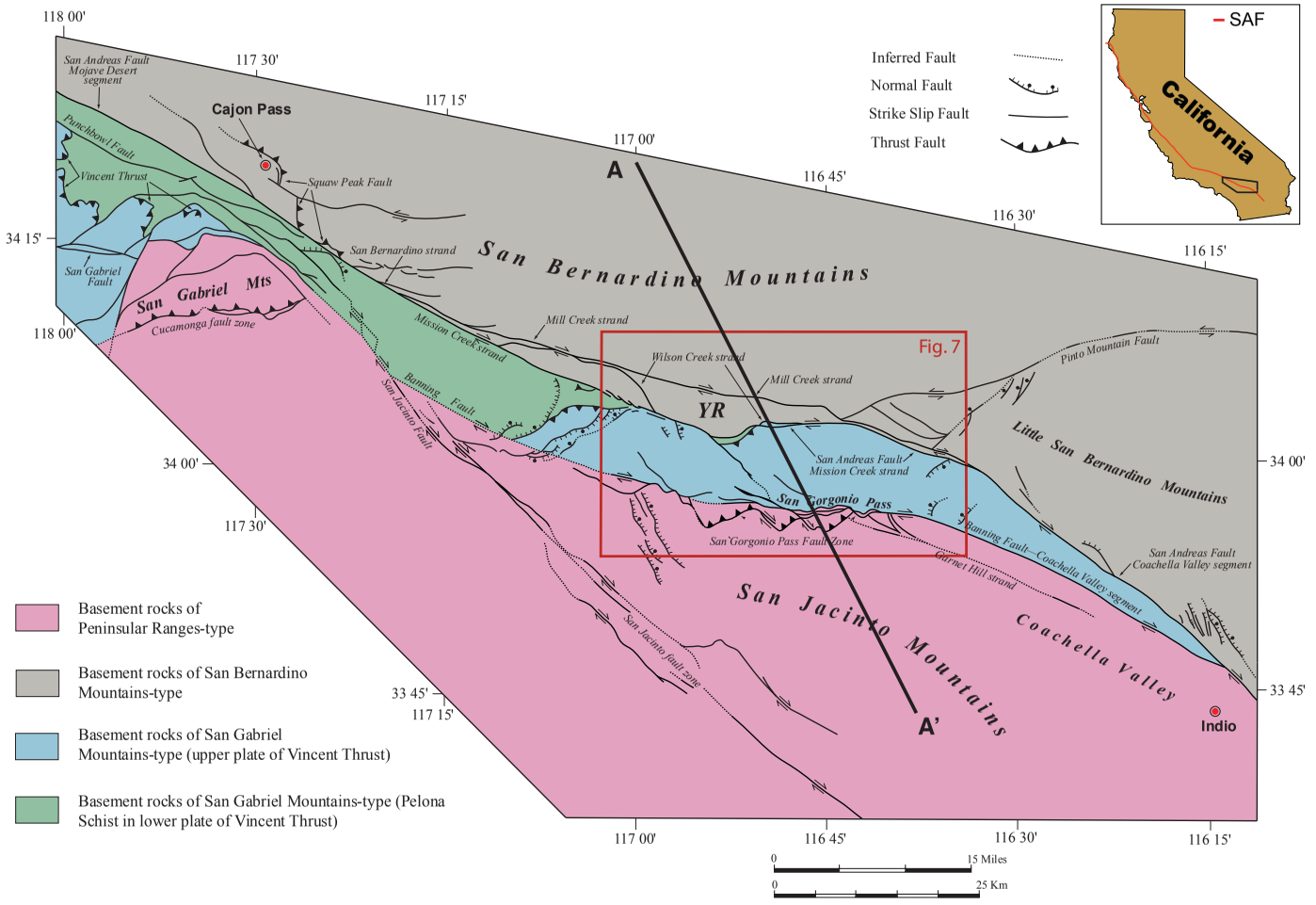

Fig. 1. Geologic map of San Gorgonio Pass that shows the major faults of the San Andreas system within this region, and distribution of four major crystalline basement terrains. The red box outlines the region enlarged in Figure 7, and line A-A' shows the trend of the cross section presented in Figure 5. Modified from Matti et al. (2003)

portion of a major strike-slip fault. This latter information is critical for modeling earthquake rupture propagation and strong ground motion, and necessary to advance seismic hazard assessment along geometrically complex fault systems.

The main tasks of this study are to define the mesoscale subsidiary fault fabric of the damage zone of the Mill Creek fault and surrounding areas, analyze the fault kinematics, and determine the kinematic relationships to bounding faults and patterns of uplift in order to unravel the deformation history and develop a synoptic model of structural overprinting as basement rocks were exhumed from seismogenic depths.

This study will contribute to a larger effort led by the Southern California Earthquake Center (SCEC) that targeted the San Gorgonio Pass region for concentrated, multidisciplinary earthquake research (http://files.scec.org/s3fs-public/SCEC4_01-Proposal_FINAL.pdf).

2. BACKGROUND

2.1. Fault Zones Structure

A mature fault zone is an irregular volume of rock that has a length, width, and shear displacement that typically are greater than the fault thickness. Faults in the mid- to upper-crust often display distinct structural domains including one or more principal slip surfaces or fault cores, where most of the shear displacement is concentrated; a damage zone bordering the core that is composed of a system of joins, faults, folds, and local distributed shear; and a relatively undeformed host rock bounding the damage zone (Fig. 2; Sibson, 1986; Chester and Logan, 1986; Wallace and Morris, 1986; Chester et al., 1993; Caine et al., 1996; Wilson et al., 2003). Observations of exhumed fault zones indicate that the intensity of deformation in damage zones increases towards fault cores (Anders and Wiltschko, 1994; Wilson et al., 2003; Chester et al., 2004, 2005; Mitchell and Faulkner, 2009; Smith et al., 2013; Choi et al., 2016).

Previous studies of the damage zones of exhumed faults (Wilson et al., 2003; Chester et al., 2004; Berg and Skar, 2005; Dor et al., 2006; Mitchell and Faulkner, 2009; Bistacchi et al., 2010; Smith et al., 2013), and active faults sampled in boreholes (e.g., Almeida, 2007) have documented that the deformation structures often display strong preferred orientations that develop and are maintained as a fault grows. This can even be the case for exhumed damage zones within more complex fault systems, such as compressional fault bends (e.g., Becker, 2012). Studies show that the structures in the damage zone surrounding a bend or fault-step evolve, increasing in number early in the displacement history (Cowie and Scholz, 1992; Chester and Chester, 1998; Vermilye

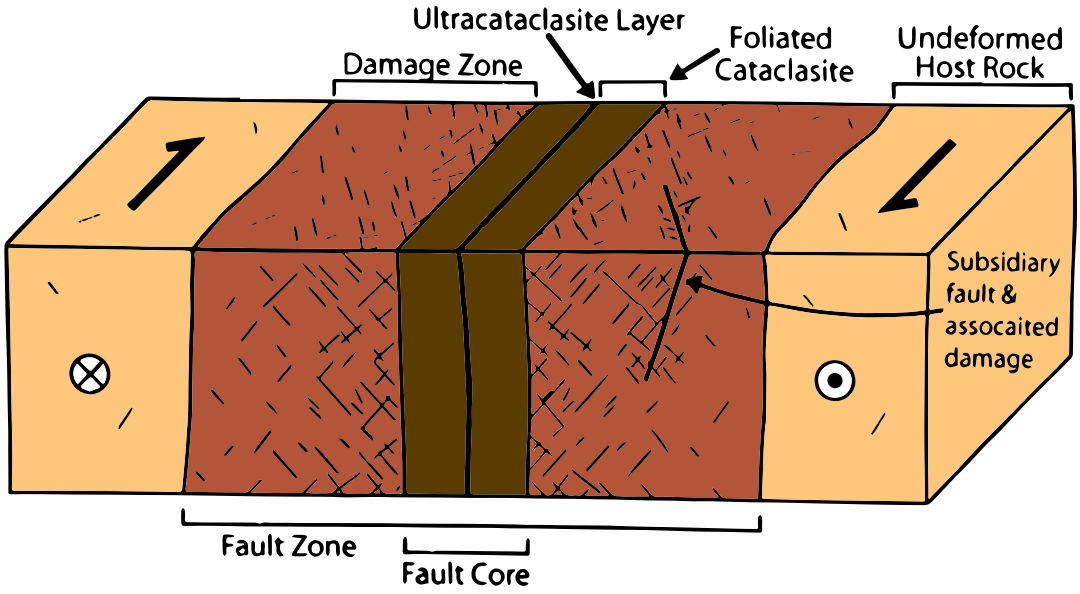

Fig. 2. Simplified block diagram illustrating the different structural domains often found in a mature strike-slip fault. The center black line represents the zone of highest shear strain, here called an ultracataclasite, representing an extremely fine-grained, cohesive fault rock, that is bounded by a zone of less sheared rock, referred to as foliated cataclasites. The foliated cataclasites and ultracataclasite together constitute the core of the fault zone. The core is bounded by a zone of damage formed in response to movement across the fault core. Modified from Becker (2012), Mitchell and Faulkner (2009), and Chester et al. (1993).

and Scholz, 1998; Savage and Brodsky, 2011), while being reactivated, extended, and cross-cut as fault maturity and slip efficiency increases (e.g., Becker, 2012; Cooke et al., 2013). This is particularly the case in mechanically homogeneous crystalline rocks and massively bedded sedimentary rocks where strong preferred fracture orientations have been shown to persist through large scale bends in the fault surface (e.g., Becker, 2012). More variable fracture patterns may develop in host rocks characterized by a strong mechanical anisotropy (e.g., Chester and Fletcher, 1997; Berg and Skar, 2005; Bistacchi et al., 2010; Becker, 2012; Smith et al., 2013)

Fault bends, identified by a change in fault strike, and stepovers identified by a discontinuous step in strike are common structures of strike-slip fault systems (Fig. 3; Crowell, 1974; Aydin and Nur, 1985; Christie-Blick and Biddle, 1985; Sylvester, 1988). Field observations of restraining fault bends and stepovers illustrate that shear along these systems can be accommodated by a combination of strike and dip-slip faulting, uplift, and folding (e.g., Barka and Kadinsky-Cade, 1988; Spotila et al., 2001; Cowgill et al., 2004; Mann et al., 2007; Mann, 2007; Bartholomew et al., 2014). Mechanical and analog models suggest that the ability for a block to move past a restraining bend improves with increasing displacement (Cooke et al., 2013; Hatem et al., 2015). This increase in efficiency occurs through the propagation and extension of new faults, reactivation of pre-existing faults, and abandonment of some fault segments (e.g., McClay and Bonora, 2001; Mitra and Paul, 2011; Becker, 2012; Cooke et al., 2013; Hatem et al., 2015). Examples of recent large magnitude earthquakes on the Southern San Andreas system that produced slip on multiple faults and significant off-fault strain

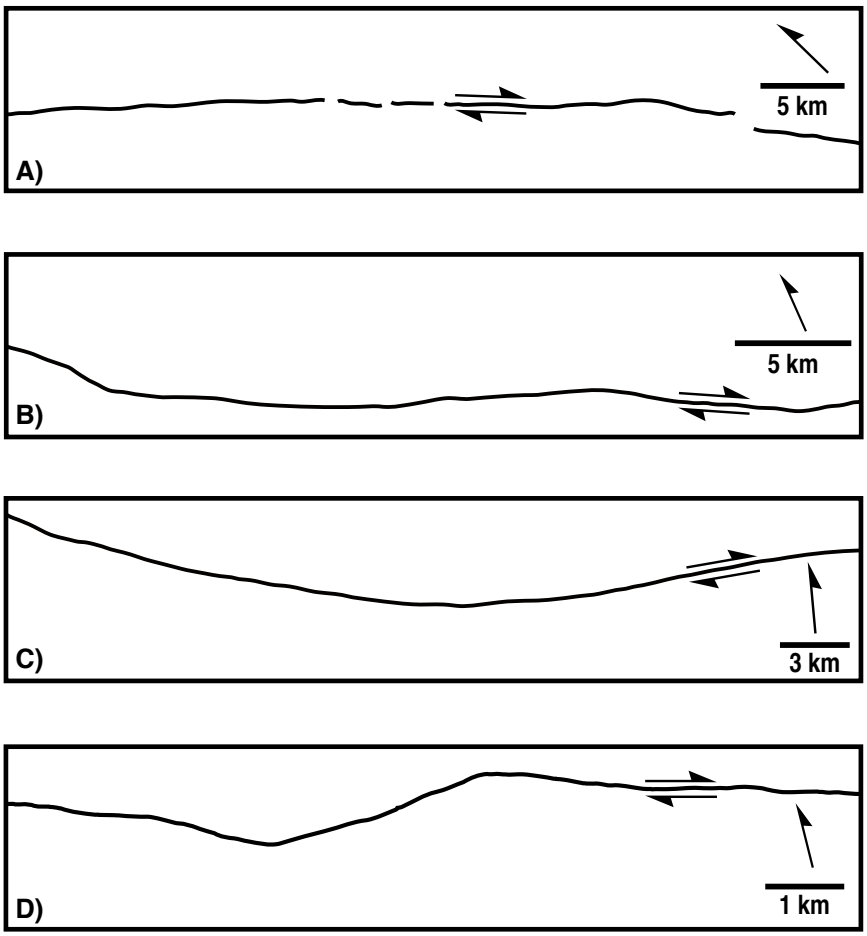

Fig. 3. Geometry of different faults within the San Andreas fault system. Faults with relatively straight segments include: (A) San Andreas fault near Parkfield and (B) Punchbowl fault. Faults with bends include: (C) North Branch San Gabriel fault, and (D) Mill Creek fault in this study. Fault traces modified from Segall and Pollard (1980), Wilson et al., (2003), and Becker (2012).

include the 1992 M_w 7.3 Landers (Wald and Heaton, 1994), 1999 M_w 7.1 Hector Mine (Peltzer et al., 2001), and 2010 M_w 7.2 El Mayor-Cucapah (Fletcher et al., 2014) events. The latter earthquake occurred on the Laguna Salada fault, which is interpreted as the southern extension of the Elsinore fault. These earthquakes ruptured through bends and steps in the principal fault surfaces and produced complex strain features in the damage zones of the major faults in their surface exposures.

2.2. Modeling of Earthquake Rupture through Geometrically Complex Fault Systems

The geometry of faults and fault systems can have a significant effect on rupture initiation, propagation, and arrest (King and Nabelek, 1985; Acharya, 1997; Kato et al., 1999; Duan and Oglesby, 2005, 2006; Duan and Day, 2008; Wesnousky, 2008; Lozos et al., 2011, 2012; Finzi and Langer, 2012; Huang et al., 2016). To better understand how fault geometry influences these processes, the scientific community has produced a wide variety of analytical and dynamic rupture models (e.g., Segall and Pollard, 1980; Kato et al., 1999; Andrews, 2005; Ben-Zion and Shi, 2005; Duan and Oglesby, 2005; Duan and Day, 2008; Templeton and Rice, 2008; Ma and Andrews, 2010; Finzi and Langer, 2012; Huang et al., 2014). Far-field stress orientations and magnitudes are modified near the terminations of faults and in the vicinity of geometric irregularities in fault surfaces. These changes in stress state can enhance or inhibit slip on the fault surface, and increase or decrease the production of strain off the fault surface (e.g., Segall and Pollard, 1980; Xing et al., 2004; Duan and Day, 2008). In restraining bends, the normal stress on the

fault plane can increase locally, leading to higher frictional resistance to slip (King and Nabelek, 1985; Acharya, 1997; Kato et al., 1999), and promote off-fault plastic deformation through fracture and other deformation mechanisms (e.g., Duan and Day, 2008). This process can dissipate radiated seismic energy, reduce material strength, and slow or stop a rupture (Andrews, 2005).

The properties of fault zones can affect seismic radiation and earthquake propagation (Andrews, 2005; Ben-Zion and Shi, 2005; Templeton and Rice, 2008; Dedontney et al., 2011; Dunham et al., 2011; Finzi and Langer, 2012; Huang et al., 2016). Significant efforts, therefore, have been made to incorporate the effects of damage zone properties in dynamic rupture models. Ben-Zion and Shi, (2005) and Dedontney et al. (2011) have explored the role of bi-material interfaces on rupture directivity and find disagreement on whether or not rupture direction can be determined based on the resulting damage asymmetry across the fault plane. Dedontney et al. (2011) test the dependency that the angle between maximum principal compressive stress direction and the fault plane, Ψ, has with plastic deformation occurring on either the compressive or extensional quadrants of a rupturing fault (Templeton and Rice, 2008) and conclude that presence of damage asymmetry, by itself, cannot be used to determine rupture directivity. Ma and Andrews (2010) and Roten et al. (2014) find that plastic strain is concentrated near the fault plane and widens near the surface of the Earth when the material surrounding the fault zone has a low cohesion. Plasticity near the fault reduces ground peak velocities because directivity pulses are not strong enough to produce waveguide amplification (Roten et al., 2014). Increased ground peak velocities, however, are enhanced by

supershear rupture. Dynamic rupture simulations on mature faults by Huang et al. (2014) suggest that supershear rupture velocities can be obtained if there is a well-developed damage zone, even without large fault stresses.

Most of the aforementioned studies include off-fault deformation in their models to approximate the permanent strain on rock after rupture. The addition of fault surface roughness (Duan and Day, 2008; Dunham et al., 2011; Lozos et al., 2011) and stepovers (Finzi and Langer, 2012) can change patterns of off-fault deformation. Specifically, the effects of fault bends localize off-fault plasticity on the extensional side of a compressive bend and reduce rupture speeds (Duan and Day, 2008; Dunham et al., 2011). These models show that off-fault deformation enhances energy dissipation and stress-relaxation. It is clear that the characteristics of off-fault damage can influence rupture propagation and that more detailed field characterizations of this damage are needed to constrain models and test model predictions.

2.3. Geology of the San Gorgonio Pass Region

The San Gorgonio Pass region is located in the San Bernardino Mountains in Southern California. In this region, the San Andreas fault system is composed of multiple segments that have variable strikes and near-vertical to low-angle dips, and display evidence of pure strike-slip to dip-slip kinematics (Fig. 1). This complexity was first referred to as a knot by Allen (1957) because of its multi-strand character and its location within a large left-stepping restraining bend defined by the San Bernardino strand of the San Andreas fault to the northwest and the Mission Creek-Coachella Valley strand to the southeast (Fig. 1).

This section of the San Andreas system has not hosted a large magnitude earthquake in over 200-300 years (Yule and Sieh, 2001; Weldon et al., 2005; Fialko, 2006). Fialko (2006) suggests that this relatively quiet period has led to an estimated 7-10 m of interseismic elastic strain accumulation. The estimated slip deficit and recent rupture scenarios (Fig. 4; Olsen et al., 2006; Graves et al., 2008, 2011; Jones et al., 2008; Cooke and Dair, 2011) indicate that this system poses a great threat to a densely populated region (e.g., Jones et al., 2008). Many factors contribute to the forecasting of seismic hazard, however, and a critical unknown here is the geometry and linkages between active faults in the subsurface to structures observed at the surface.

The seismogenic zone in the San Gorgonio Pass extends to 15 – 20 km depth (Jones, 1988; Petersen and Wesnousky, 1994; Magistrale and Sanders, 1996) and has seismicity patterns that are markedly different above and below 12 km (Nicholson et al., 1986). Earthquake activity above 12 km is distributed over a relatively large area and appears to define short and linear fault segments, consistent with the fault complexity displayed at the surface. In contrast, below 12 km seismicity is much more concentrated, defining a relatively small active area. Estimated stress drops across the Mill Creek-Mission Creek fault stepover are greatest between the Mill Creek Fault and San Gorgonio thrust fault (Fig. 1), implying an inverse relation between stress-drop and slip-rate (Goebel et al., 2015). Slip rates decrease from 25 mm/yr in Indio Hills, to the northwest and from 20 mm/yr at Cajon Pass to the southeast (e.g., Gold et al., 2015; McGill et al., 2015) to 8 – 5.7 mm/yr in the center of the Pass. Slip rates drop to a minimum at the center of the

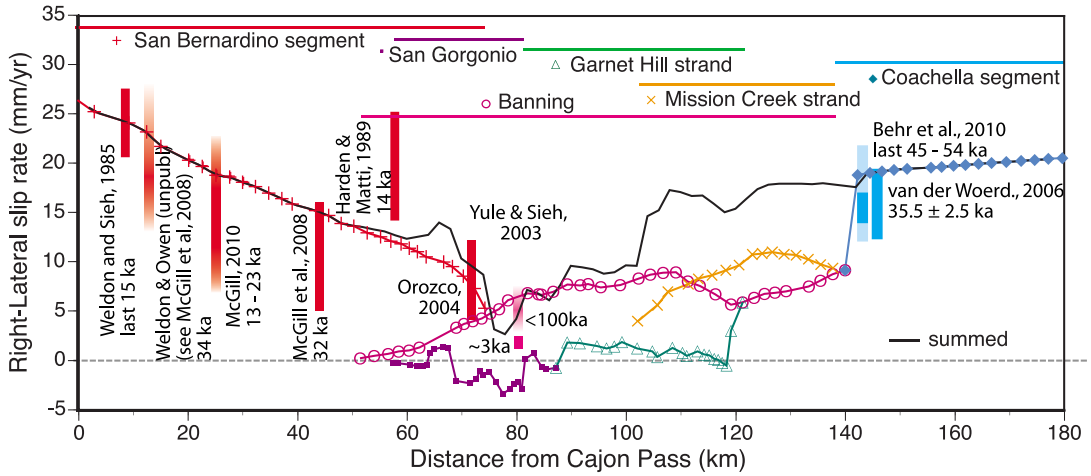

Fig. 4. Right-lateral slip rate along the surface trace of the San Andreas fault along a 180 km traverse south from Cajon Pass. Slip rates determined from paleoseismologic studies, indicated by the vertical bars, are shown relative to model estimates. The black line through the data represents the summed rate from all modeled fault strands. Figure taken from Cooke and Dair (2011).

Pass where a significant slip deficit within the knot has been proposed (Fig. 4; e.g., Cooke and Dair, 2011).

Sparse microseismicity in the upper 5 km of the crust makes it difficult to link the surface traces of mapped faults to seismicity at depth (Nicholson et al., 1986; Seeber and Armbruster, 1995; Magistrale and Sanders, 1996; Yule and Sieh, 2003; Goebel et al., 2015). Several structural interpretations have been proposed to describe the obscured fault geometries and linkages through the Pass. One of these interpretations suggests that the San Gorgonio thrust is part of a massive landslide that conceals an underlying vertical through-going San Andreas fault (Rasmussen and Reeder, 1986). A second interpretation equates the San Andreas fault to a linear trend in seismicity trend that is offset by the San Gorgonio fault; the two faults then converge westward and diverge southeastward (Seeber and Armbruster, 1995). Yule and Sieh (2003) consider geomorphic, seismicity, and field observations of others (Allen, 1957; Dibblee Jr., 1982; Matti et al., 1992a; Matti and Morton, 1993; Magistrale and Sanders, 1996) to arrive at a third interpretation (Fig. 5). They suggest a north-dipping flower-like thrust system exists that has multiple strands over the depth of known seismicity. They interpret this structure to reflect oblique-slip related to convergence in the vicinity of San Gorgonio Pass (Yule and Sieh, 2003). This third hypothesis implies a clear through-going fault at depth (Yule and Sieh, 2003; Carena et al., 2004; Dair and Cooke, 2009; Yule, 2009).

Focal mechanisms for earthquakes with magnitudes from 2.6 to 4.3 indicate substantial oblique-reverse and oblique-normal fault motion has occurred in the Pass region (Jones, 1988). Focal mechanisms change with depth from strike-slip dominated

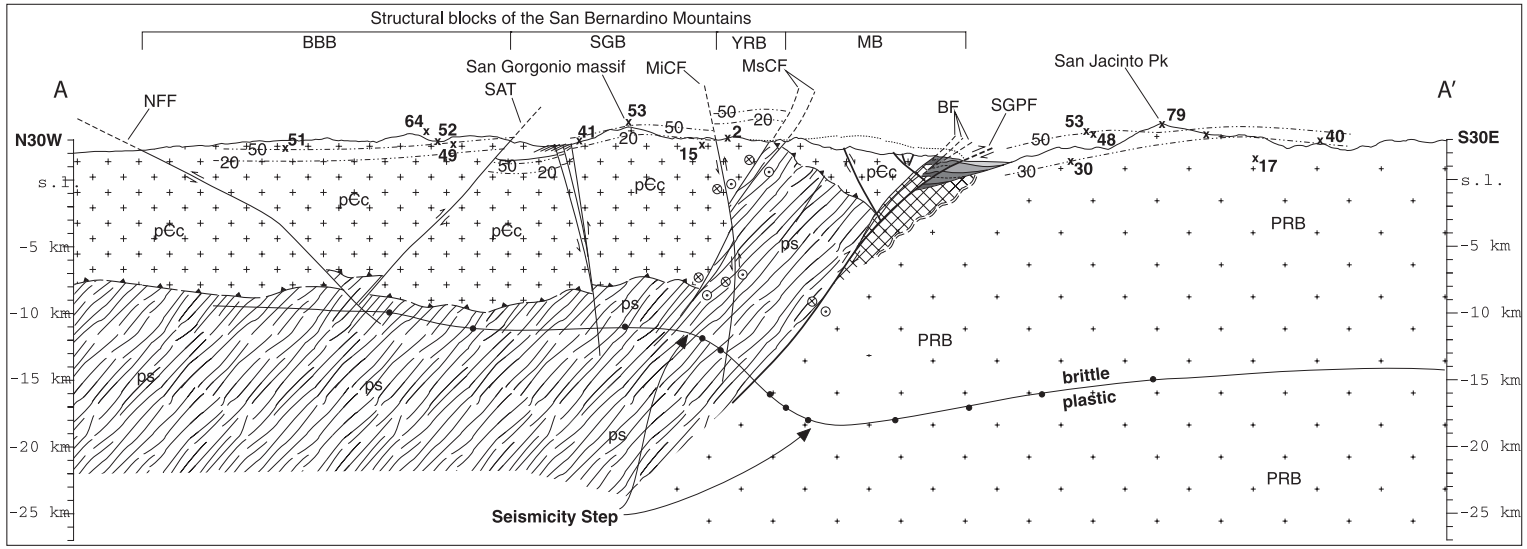

Fig. 5. Regional cross section through San Gorgonio Pass. Bold numbers represent Helium ages, and suggest rapid uplift in Yucaipa Ridge relative to the surrounding structural blocks. Trend of cross section line shown on Figure 1. Modified from Yule and Sieh (2003)

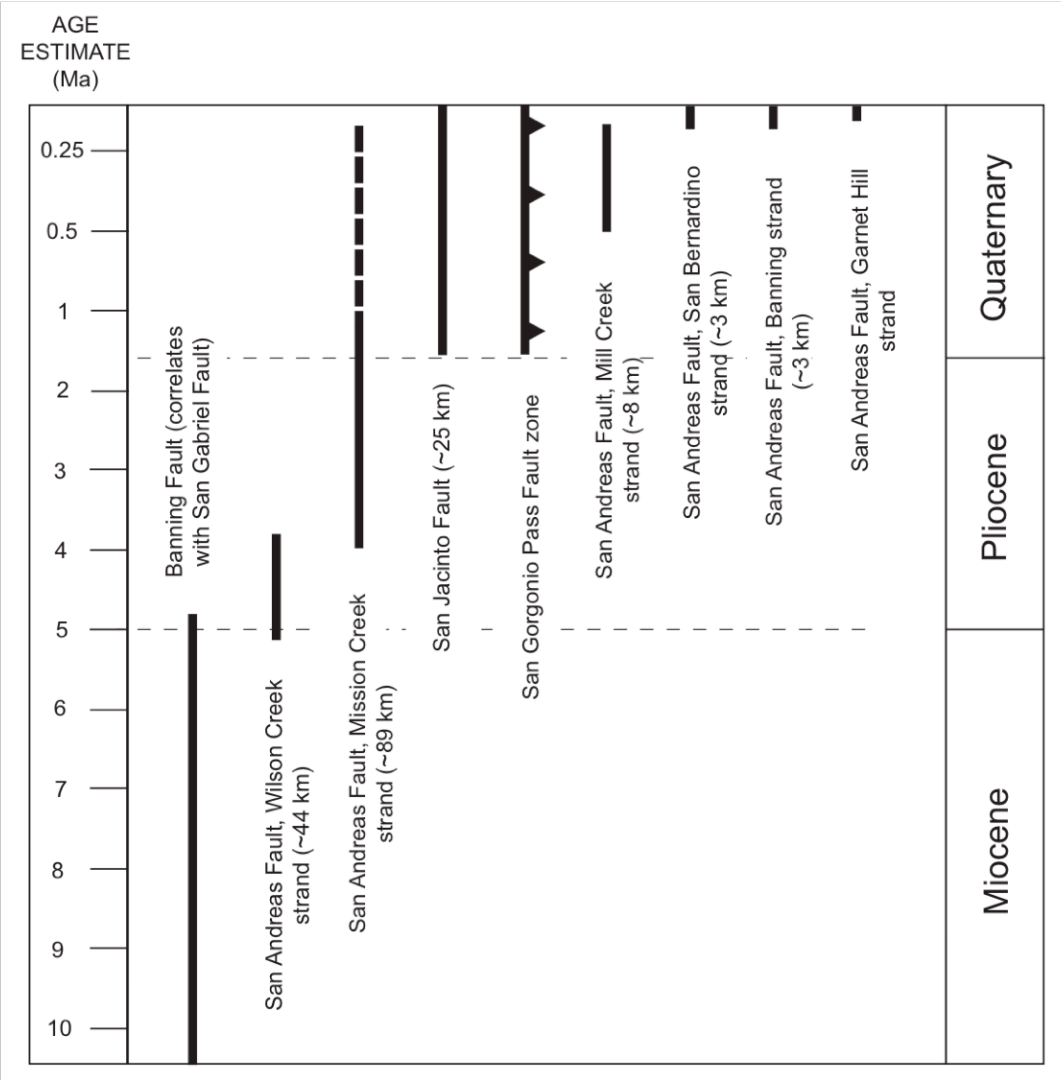

Fig. 6. Estimates of activity and displacement magnitudes on faults within the San Bernardino Mountains and surrounding areas. Timing estimates are based on stratigraphic reconstructions. Dashed lines represent inferred activity. Figure taken from Kendrick et al., (2015) that incorporates data provided by Matti et al. (1992b, 1993), and is modified from Langenheim et al. (2005).

motion within the top 10 km to an increasing number of reverse mechanism below 10 km, and normal mechanisms below 15 km. Overall, observations suggest that the maximum principal horizontal compressive stress is oriented at a high angle (68°-73°) to the average strike of the local faults, concordant with observations of Zoback et al. (1987) and Shamir et al. (1988) for other portions of the San Andreas fault. Spotila and Sieh (2000) and Spotila et al. (2001) use these stress direction observations to support the hypothesis that the structural style in the San Gorgonio Pass region reflects the obliquity between crustal block motion and movement through a large restraining bend. This configuration has led to rapid uplift of structural blocks at rates of 5-7 mm/yr (Spotila et al., 2001). This same study found that Yucaipa Ridge has been exhumed from 2-3 km depth, but it is uncertain whether or not uplift rates have changed since 1 Ma.

Based on palinspastic reconstructions, Matti and Morton (1993) estimate that after the San Gabriel fault was abandoned (Fig. 6), the main trace of the southern San Andreas fault accumulated no more than 160 km of displacement. They suggest that this displacement took place over the last 4-5 Myr, with most of the complexity in the fault structure developing during last 1.2 Myr (Fig. 1; Matti et al., 1992; Matti and Morton, 1993). During that time, the Mission Creek fault surface became progressively less planar as a result of left-lateral movement on the Pinto Mountain fault (Dibblee, 1968; Matti and Morton, 1993) until it was abandoned in the southern portion of the region when the San Gorgonio Pass fault formed (Fig. 6). At the same time, the decrease in strike-slip activity in San Gorgonio Pass gave rise to the San Jacinto fault that served to

help transfer some slip south of San Gorgonio Pass. The Mill Creek fault then developed as slip across the whole system continued (Figs. 1 and 6).

The Mill Creek fault was first named and described by Hill (1928) as one of the most prominent faults in Southern California. This fault diverges from the San Bernardino strand of the San Andreas fault at a low angle (Fig. 1) and bounds the San Gorgonio restraining bend on the north. The sheared core of the Mill Creek fault outcrops in two locations in Mill Creek Canyon, where otherwise is covered by alluvium (e.g., Allen, 1957; Matti et al., 2003). The fault core is surrounded by a green and red damage zone that is approximately a hundred meters in thickness (Allen, 1957). The fault extends to the east through Raywood Flat, a topographically high fluvial drainage where many generations of incised gravels and conglomerates have been deposited (Kendrick et al., 2015).

Matti et al. (1992, 2003) and Kendrick et al. (2015) suggest that the maximum magnitude of right-lateral slip on the Mill Creek fault in the Raywood Flat area is 8 km; an estimate that is based on offset Late Pleistocene gravels in the Hell For Sure Canyon and the North Fork of Whitewater Canyon. This estimate is much smaller than Gibson's (1971) estimate of 120 km that was based on stratigraphic correlation of the Mill Creek Formation to the Mecca and Palm Springs Formations. Kendrick et al. (2015) further suggest that the Mill Creek fault is offset 1.25 km by the Pinto Mountain fault and that slip is now accommodated by the San Bernardino, Banning, and Garnet Hill faults (Figs. 1 and 7), the most active faults of the southern San Andreas fault system. Pleistocene gravels at City Creek suggest that the western segment of the Mill Creek fault, west of

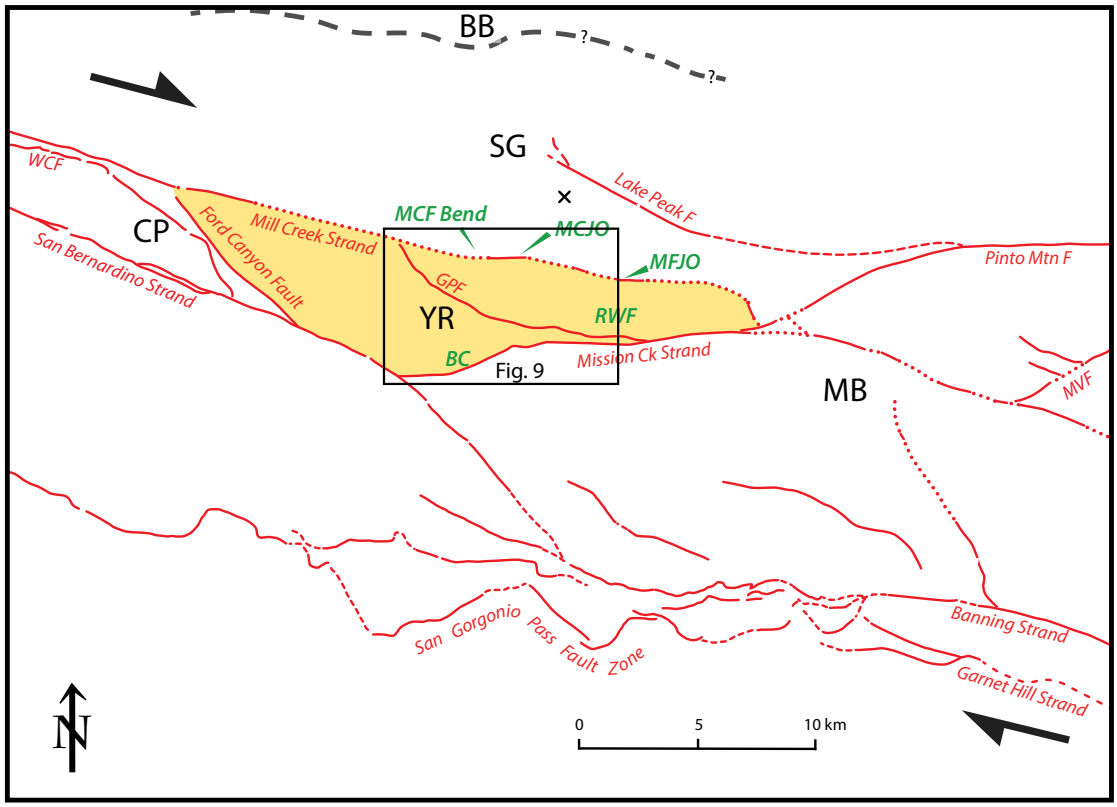

Fig. 7. Fault map within the San Gorgonio Pass "structural knot". Black box outlines the study area for this project. The study area is located in the central region of the Yucaipa Ridge structural block (YR, yellow). Other areas are the: Big Bear structural block (BB); Cram Peak structural block (CP); San Gorgonio structural block (SG); Lower Raywood flat (LRWF), Mill Creek Jump-off (MCJO), Middle Fork Jump-off (MFJO), Banning Canyon (BC). The bend of the Mill Creek fault (MCF) is also shown. Modified from Kendrick et al. (2015).

Forest Falls, CA, may still be active with a slip of about 2 mm/yr (McGill et al., 1999). The activity of the Mill Creek fault has been constrained indirectly using cross-cutting relations between sedimentary deposits on the Mission Creek and San Bernardino faults (Fig. 1; Matti et al., 1992; Matti and Morton, 1993; Matti et al., 2003; Langenheim et al., 2005; Kendrick et al., 2015). These relations estimate that most of the displacement on the Mill Creek fault took place from ~500 kyr to ~120 kyr (Fig. 7).

3. METHOD OF STUDY

3.1. Field Observations and Data Collection

Prior to going into the field, the main faults within the study area (Fig. 7) were located using published maps and reports (Dibblee Jr., 1964, 1967, 1970, Matti et al., 1983, 1992b, 1992c; Kendrick et al., 2015), and also located using Google Earth. Early stages of field work were dedicated to traversing the accessible regions of the study area (Fig. 7) to locate significant fault zone exposures and to define the boundaries of their damage zones, locate suitable outcrops of basement rocks, and search for offset-gravel deposits to help determine the most recent movement on faults in the region.

From this exploration, data collection stations were established and mapped on 1:24,000 USGS topographic base maps using iHikeGPS. Outcrop stations that displayed brittle and ductile deformation, offered the possibility of obtaining three-dimensional outcrop views, and provided laterally extensive outcrop faces were prioritized for study and designated as recording stations. Specific stations that were chosen as sites for multiple structural measurements were photographed and printed so that the locations and traces of measured items could be recorded directly on the images; data recorded included the orientation of the outcrop face.

All geologic data collected from each station were recorded in a field notebook. Features mapped and recorded include: (1) observed and inferred boundaries and types of major and minor faults, (2) rock type, (3) orientations of subsidiary faults, fault slip-vectors, apparent sense-of shear determined from offset features, and slip-surface mineralization, (4) cross-cutting fault relations, and (5) orientations of foliations, when

present. All measurements were assigned a quality factor (excellent, good, fair, poor) to allow for data sorting and detailed analysis later. Particular attention was focused on describing the full kinematics of deformation in the damage zone of the Mill Creek fault.

All structural data were plotted and analyzed using Stereonet3D, a free software package developed by Cardozo and Allmendinger (2013) and available for download from the Apple App Store.

The field reconnaissance defined four distinct, accessible regions to best explore the kinematic history of the Mill Creek fault system, within Mill Creek canyon, and its relation to the Galena Peak and Mission Creek faults (Figs. 7 and 8). These regions are referred to as Mill Creek Canyon, Yucaipa Ridge, and Raywood Flat (Figs. 7 and 8).

Representative oriented samples of the San Bernardino-type metamorphic and igneous complex were collected from several stations along the Mill Creek fault and surrounding regions. Additional oriented samples were collected from the fault cores and their damage zones. These samples were collected for future studies to allow a comparison of the mesoscale subsidiary fault data, collected and analyzed during this study, to future microstructural observations to better define the relative timing of deformation events in the area and identify the fluid-rock reactions during deformation.

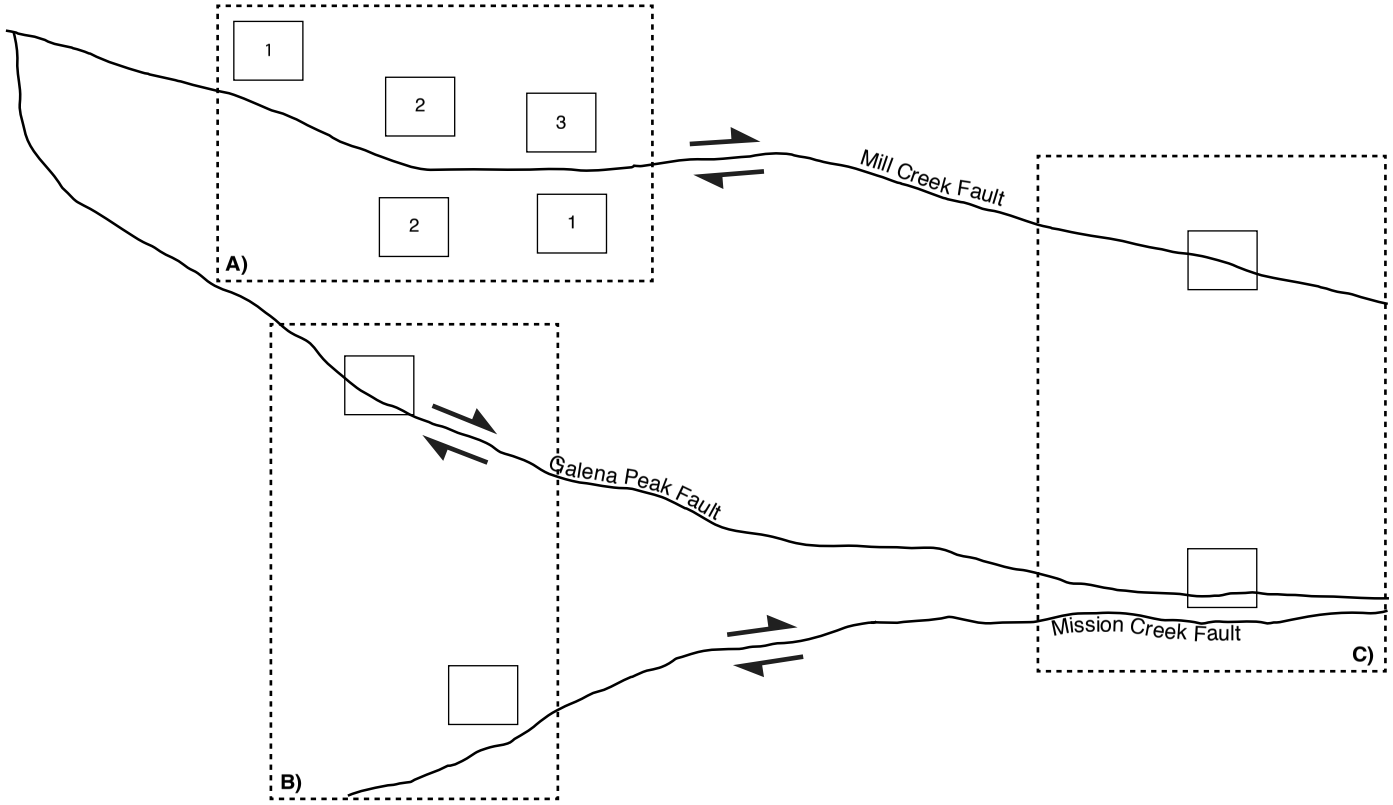

Fig. 8. Diagram of the different regions of the study area. Boxes with dashed outlines identify the distinct structural domains the study area: (A) Mill Creek canyon region; (B) Yucaipa Ridge region; (C) Raywood Flat region. Boxes with solid outlines represent the distinct structural domains. Inside each structural domain there are multiple measurement stations.

3.2. Data Analysis

3.2.1. Outcrop Image Analysis

Photographs of the stations were used to mark measurements and build geologic outcrop maps. These maps aid to point out patterns related to the orientation, geometry, and spacing of subsidiary faults and other features. Analysis of these groupings enabled for determination of kinematic relationships between the types of data and helped provide relative timing of faulting. These data were used to elaborate upon the poorly constrained timing of events related to the Mill Creek Fault activity.

3.2.2. Stereographic Analysis

Data analysis was done utilizing lower-hemisphere equal-area stereographic projections provided by Stereonet3D (Cardozo and Allmendinger, 2013). Subsidiary fault data plotted were grouped into specific categories for orientation analysis by station and by larger structural domain. The data categories analyzed are: faults, slip vectors, b-axes, longest faults, gouge zones, breccia zones, iron-stained grooved or slickenline surfaces, epidote-lined grooved and slickenline surfaces, and surfaces showing both iron-oxide and epidote-lined surfaces. Analysis of these groupings were used to relate kinematics to timing and relative importance of features. Data from the damage zones of the major faults were separated into structural domains defined on the basis of position north and south of the master fault, and location relative to geometric irregularities in the master fault orientation. Fabric variations relative to structural domains were analyzed to determine kinematics, including timing of formation, rotation, and overprinting, and to

interpret the orientation of the principal stress directions that may explain the fabric of distinct fabric categories within each structural domain.

Cross-cutting relationships or overprinting relationships were used to determine the relative timing of deformation events between different subsidiary features. These relationships were then used to interpret the development of the Mill Creek – Mission Creek stepover.

3.2.3. Kinematic Analysis

To confirm possible conjugate relationships of subsidiary fault sets the true slip direction was determined from apparent separation estimates seen in the field. Under certain circumstances, assuming that the slip vector of the offsetting fault reflects the most recent direction of slip, it was possible to estimate the true slip direction using stereographic projections. The analysis can be carried on if the orientation of the outcrop face, offset structural feature, offsetting fault, and the slip direction along the offsetting fault are known.

Groups of strike-, oblique-, and dip-slip were distinguished from the kinematic analysis. In order to avoid confusion between type of fault, those faults with steep dips whose slip vectors vary within 20-30 degrees from true dip are called dip-slip faults. Faults with steep dips whose slip vectors vary within 20 degrees from horizontal are called strike-slip faults. Any fault and slip vector orientation between those limits is called an oblique-slip fault. In addition, oblique-slip faults were further divided into four kinematic types: Left-Lateral Normal (LL-N), Left-Lateral Reverse (LL-R), Right-Lateral Normal (RL-N), and Right-Lateral Reverse (RL-R).

4. RESULTS

4.1. Major Faults and Lithology

The study area extends over the San Gorgonio, Yucaipa Ridge, and Morongo structural blocks where the Mill Creek fault and Mission Creek fault form a stepover (7). Within the stepover the Mill Creek fault is mostly concealed by alluvium and its trend follows two prominent canyons formed by head-ward erosion of Raywood Flat. It is in Mill Creek Canyon where a large-scale bend is inferred from the geometry of the canyon and fault core exposures. Along the southern boundary of the study area the Vincent Thrust crops out close to the Mission Creek fault but its trace is disregarded in mapping because it predates San Andreas fault-related deformation.

A total of 62 oriented samples were collected and cover every structural domain of the study area. A minority of samples were collected in structural domains outside of Mill Creek Canyon. Samples include gouge and rock samples from locally representative rock types. Although microscopy work could not be completed on the samples, the hand samples were used to provide rough estimates of lithology and to provide an understanding of lithological changes in the study area.

The rock units encountered in the study area are generally concordant to those described in group by previous studies (Allen, 1957; Matti et al., 1992a). In order to highlight some of the local characteristics that may exert some control over the damage fabric, like differences in intensity of foliation, rock type, and possibly age, a more detailed description of the lithology of the area is provided. Those descriptions are limited to the extent of Mill Creek Canyon.

Table 1
Outcrop size, lithology, and measurements by structural domain in the Mill Creek canyon region.

Domain	Station	Location	Exposure Size	Dominant Lithology	Foliation	Total # of Fracture Measurements	Total # of Slip Vectors	Faults with apparent Sense of Shear
Straight Segment - Before Bend N	1W	Mill Creek Canyon	< 400 m*	G, Q	Mild to Absent	21	21	-
	1N	Mill Creek Canyon	105 m	Q	Moderate to Absent	113	78	17
Straight Segment - After Bend S	-	-	-	-	-	-	-	-
Bend Region - North	SB9	Mill Creek Canyon	90 m	B, MQ, Q	Mild to Absent	98	30	14
Bend Region - South Transfer Zone	40	Yucaipa Ridge	100 m	G	Moderate to Heavily Contorted	95	66	7
	41	Yucaipa Ridge	32 m	G	Moderate to Heavily Contorted	61	50	7
	43	Yucaipa Ridge	133 m	G	Moderate to Heavily Contorted	84	57	29
	44	Yucaipa Ridge	45 m	G	Moderate to Heavily Contorted	49	28	4
Straight Segment - After Bend N	10	Mill Creek Canyon	113 m	Q	Moderate and planar	101	62	56
	14-15	Mill Creek Canyon	< 50 m**	Q	Moderate and planar	40	25	12
	17	Mill Creek Canyon	67 m	Q	Moderate and planar	111	72	62
Straight Segment - Before Bend S	18	Mill Creek Canyon	180 m	B, G	Heavily Contorted to Absent	116	93	16

*Includes multiple exposures. **In case of no direct measurement, the length of outcrop size is estimated.

The rock type north of the Mill Creek fault is generally coarse-grained quartz monzonite of Mesozoic age (Table 1). The monzonite is foliated to different degrees and intrudes older foliated metamorphic rock. A small patch of biotite orthogneiss that is heavily intruded by felsic dikes is present north of the bend region. The south side of the fault exhibits granitic orthogneisses that are heavily foliated (Table 1). In many instances the gneisses show a migmatitic texture rendering most foliation measurements unreliable for structural relationships. In some parts the orthogneiss is intruded by a more mafic composition rich in hornblende, plagioclase, and biotite.

The Mill Creek Fault is interpreted to have accumulated 8.7 km of right-lateral slip (Kendrick et al., 2015) and displays a prominent fault bend as observed in Mill Creek Canyon. The trace of the Mill Creek fault is concealed by alluvium over most of its length across the study area. West of the bend, the orientation of the fault is inferred from the straight orientation of the canyon, that trends 290˚, for greater than 10 km (Dibblee Jr., 1964) and the steep to vertical canyon walls (e.g., Fig. 7). The fault bend is not directly observed, but must occur in the vicinity of station SB4; the change in strike at the bend is approximately of 20˚ occurring over a distance of about 250 m (Fig. 9). The orientation of the fault east of the bend comes from direct measurement along the two fault core exposures near the headwaters of Mill Creek Canyon (Figs. 10, 11, and 12). The average strike of the fault from measurements at stations SB0 and SB8 is E-W and the dip ranges from 43˚ to 54˚ to the south. These observation indicate that the Mill Creek fault orientation changes from a nearly vertical, northwest-orientation west of the

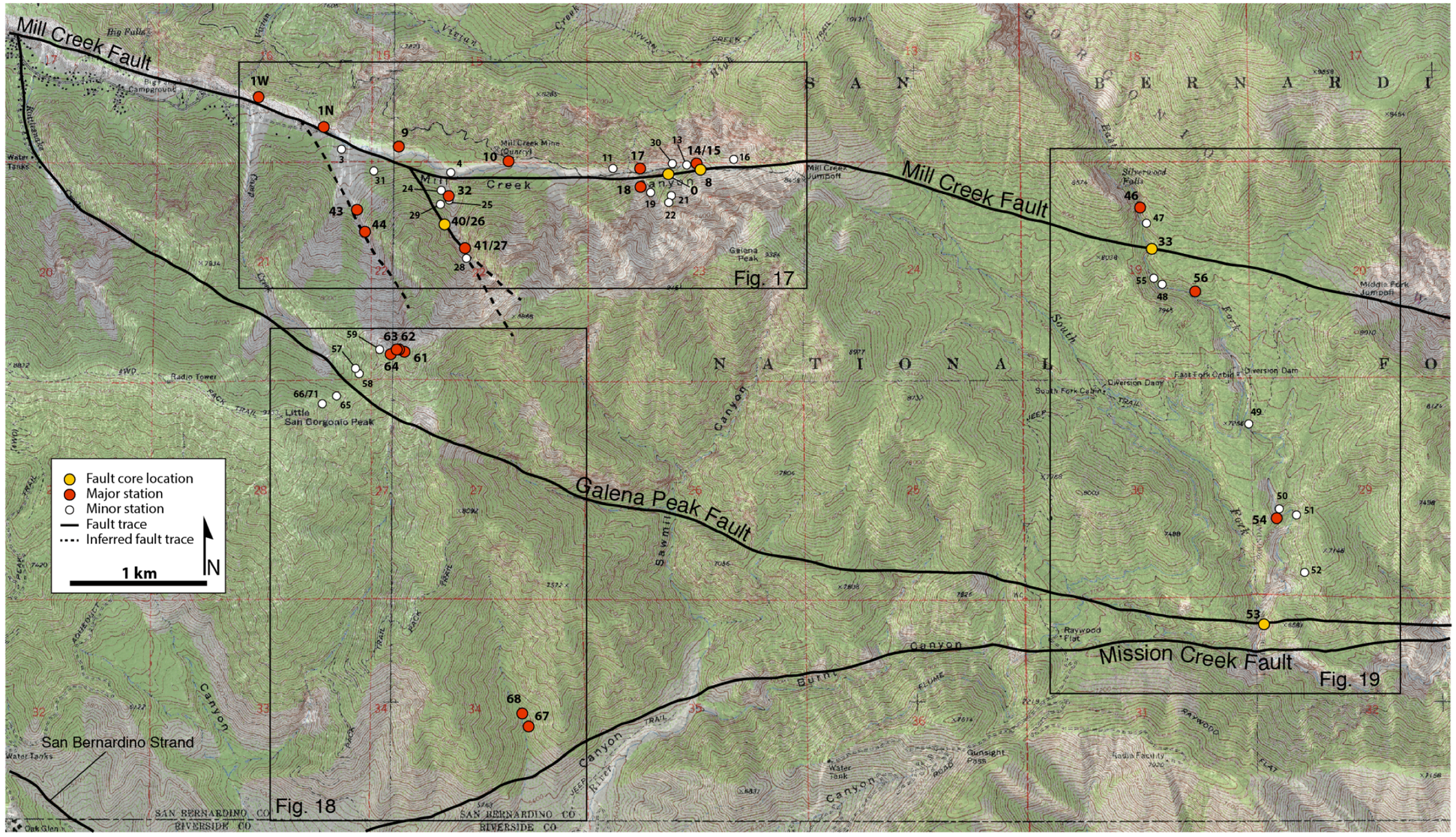

Fig. 9. Topographic map of the study area showing the major fault traces. Yellow dots represent exposures of faults cores. Red dots indicate stations with more than five structural measurements. White dots indicate stations with less than five structural measurements. The solid boxes indicate the regions illustrated and discussed later in the text.

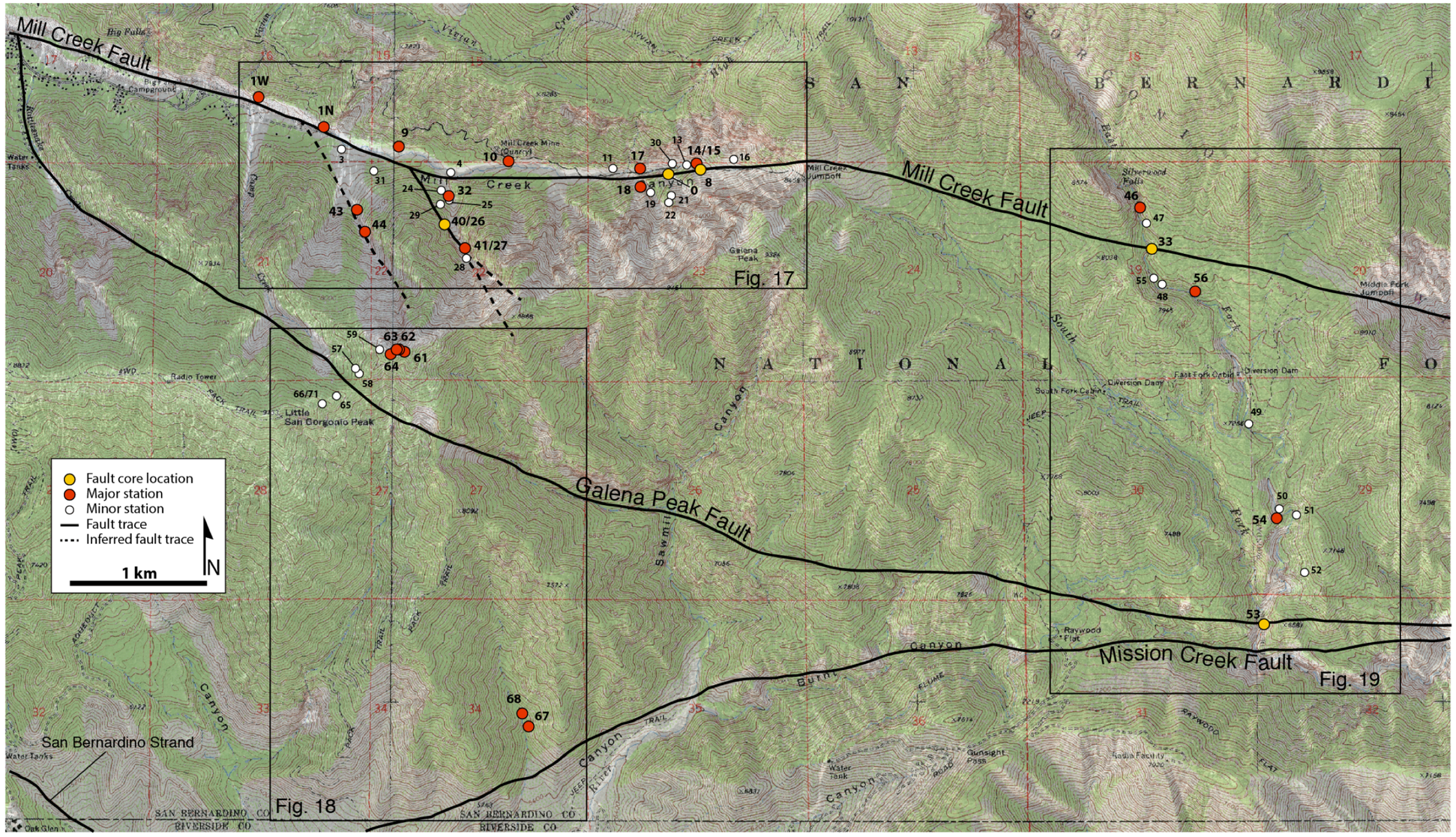

Fig. 9. Topographic map of the study area showing the major fault traces. Yellow dots represent exposures of faults cores. Red dots indicate stations with more than five structural measurements. White dots indicate stations with less than five structural measurements. The solid boxes indicate the regions illustrated and discussed later in the text.

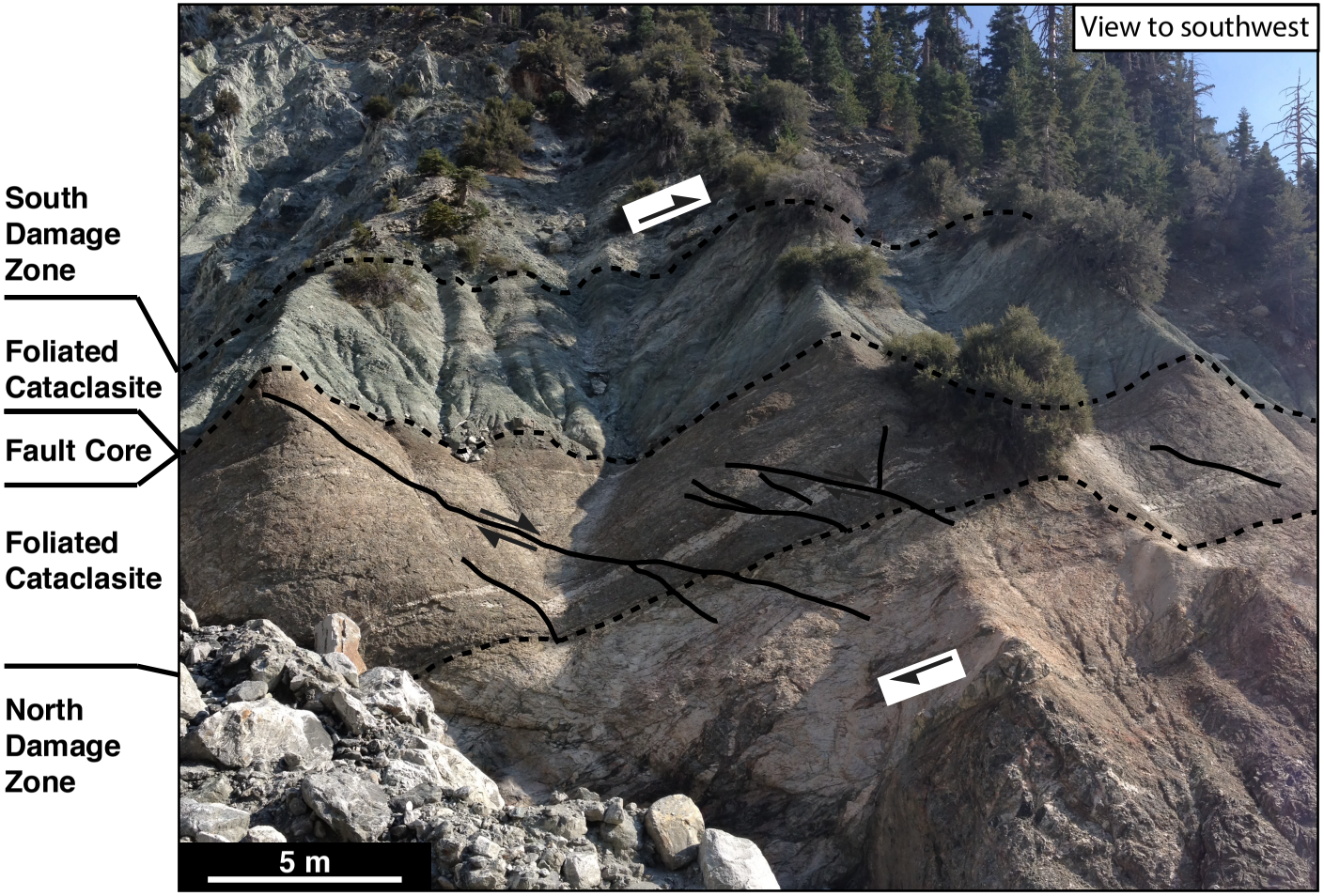

Fig. 10. View perpendicular to strike of the Mill Creek fault damage zone. This fault exposure is located at Station 0 (Fig. 9). Long subsidiary faults cut across the southern foliated cataclasite unit and display consistent apparent sense of shear. Arrows denote the sense of shear of the fault.

bend to a lower-angle oblique reverse fault in the headwaters region of Mill Creek canyon.

The trace of the Mill Creek fault is concealed by alluvium over most of its length across the study area. Estimates of the orientation of the fault come from direct measurement along the fault core exposures and it is inferred to exist in between those exposures. West of the SB0 exposure in Mill Creek Canyon (Fig. 9) the orientation of the Mill Creek fault is interpreted to follow the orientation of Mill Creek Canyon. Therefore, the existence of a fault bend is not directly observed from fault measurements but it is assumed to exist from indirect evidence such as the south transfer zone or the change in kinematics with respect to the straight segments of the Mill Creek fault.

4.2. Mesoscale Structure of Major Faults

The fault zone structure of the Mill Creek, Galena Peak and an unnamed fault crossing Yucaipa Ridge were identified in the field (Fig. 9). The Mill Creek fault was exposed twice in Mill Creek Canyon and once in Raywood Flat, the rest of the faults were only encountered once. The structure of these faults is highly variable through the study area even for exposures of the Mill Creek fault.

4.2.1. Mill Creek fault

The fault core of the Mill Creek fault is characterized by multiple dark brown gouge units ranging from ultracataclasite to cataclasite (Fig. 10). The brown cataclasite layer varies from a few to 36 cm to the east (Fig. 11 and 12). The thickness of this layer is variable depending on location (Figs. 11 and 12). The cataclasite layer is aphanitic but contains more clasts and slivers of host rock as it thickens (Fig. 12).

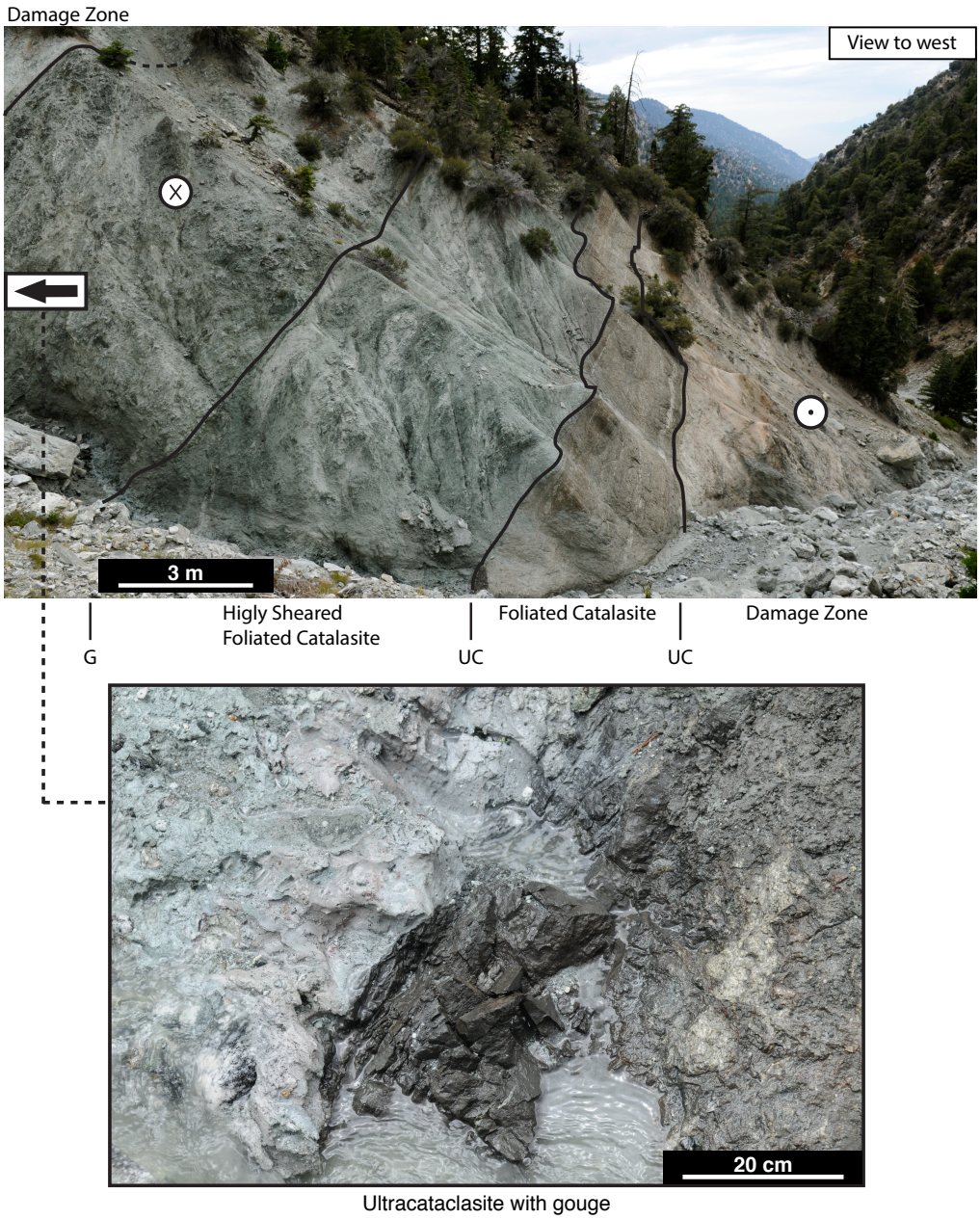

Fig. 11. View parallel to strike of the Mill Creek fault core and damage zone. This fault exposure is located at Station 0 (Fig.9). Multiple ultracataclasite (UC) and gouge (G) layers are found within and bounding the damage zone (top). An additional ultracataclasite core surrounded by gray gouge is found south in the direction pointed by the arrow. White circles with cross and dot indicate movement away and towards, respectively, and represent the sense of shear of the fault.

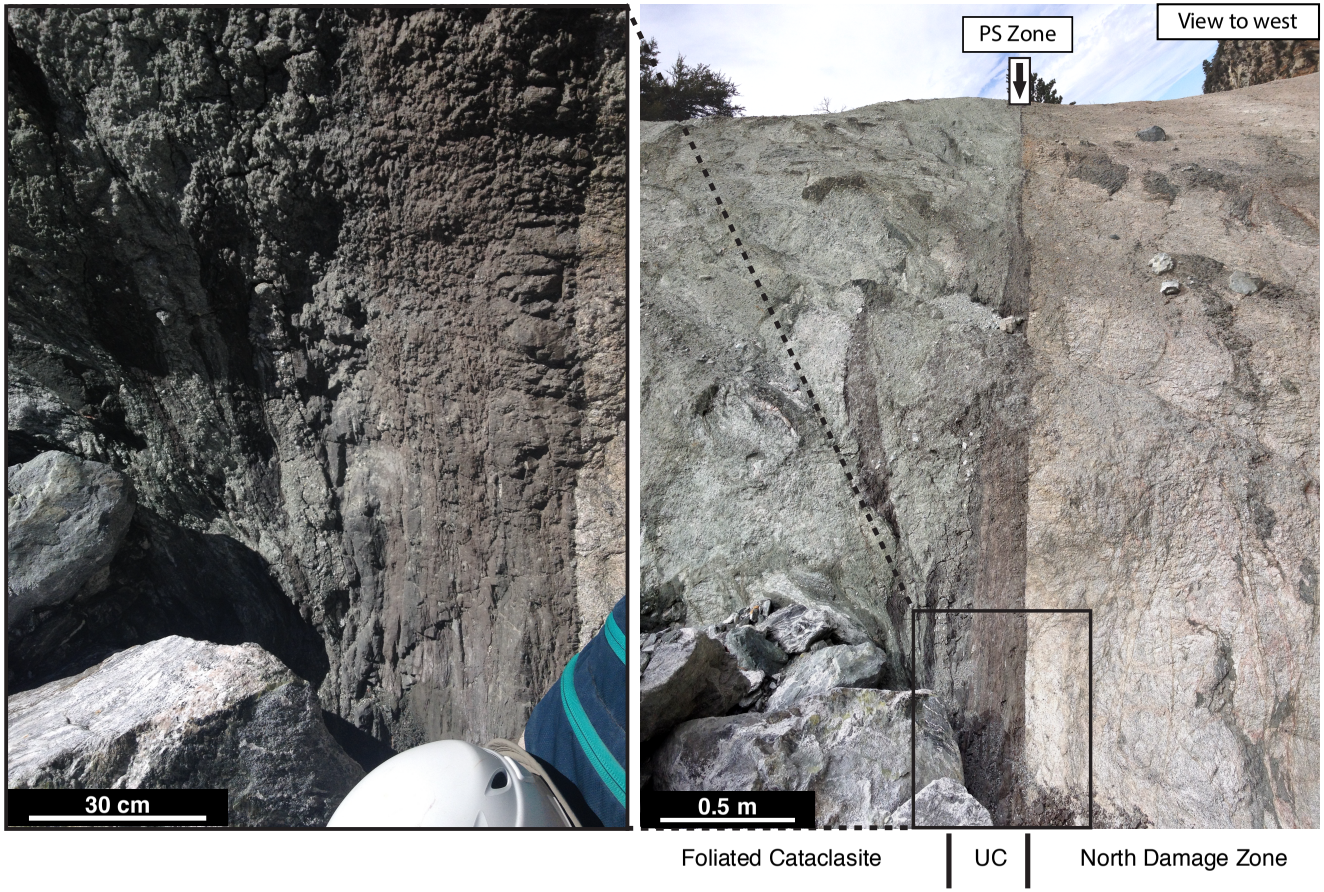

Fig. 12. Second view parallel to strike of the Mill Creek fault core and damage zone. This fault exposure is located at Station 8 (Fig. 9). The ultracataclasite (UC) layer shows multiple localized slip surfaces within the fault core (left). It is marked by a sharp contrast in grain size from the north damage zone and foliated cataclasite (right). The ultracataclasite layer thins to the west into a single principal slip surface (PS Zone).

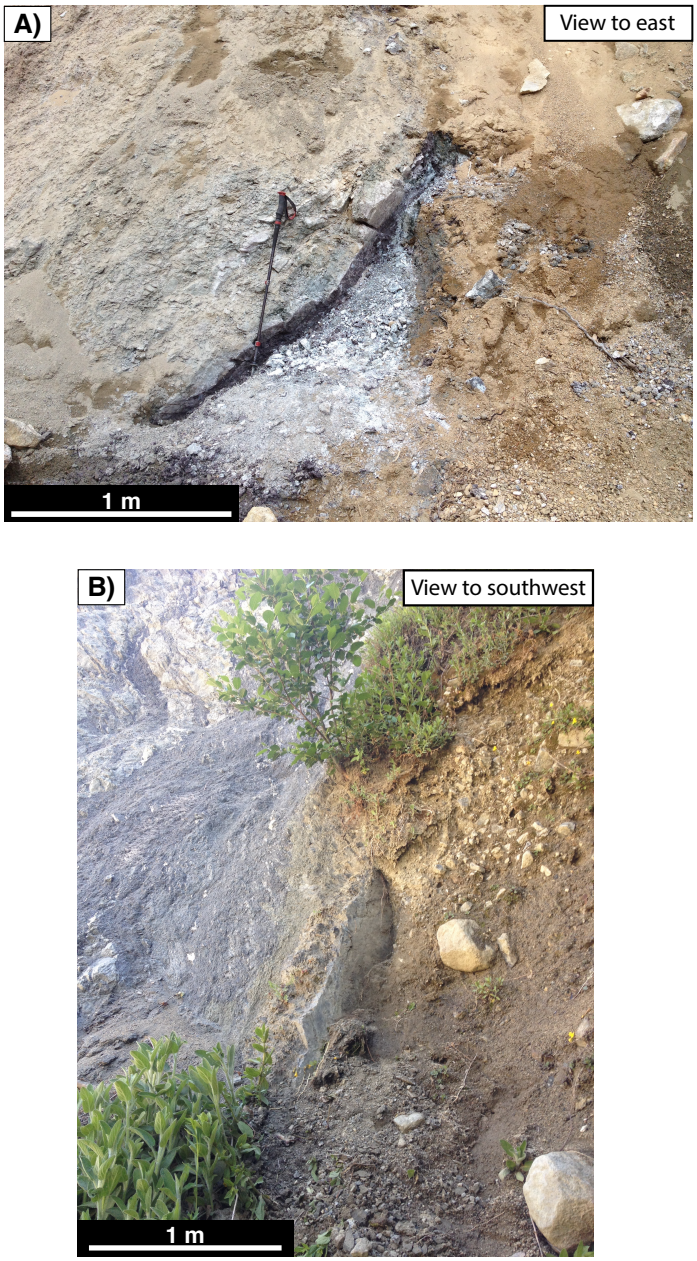

Fig. 13. Outcrop photographs of other fault exposures in the Raywood Flat region. A) Fault core exposure of the Mill Creek fault located at Station 33 (Fig. 9). This fault exhibits an incohesive layer of purple gouge that is covered by alluvium towards the top of the image. B) Fault core exposure of the Galena Peak fault located at Station 53 (Fig. 9). This fault exhibits a cohesive core of indistinguishable grain size that separates heavily foliated and sheared host rock from an alluvial deposit.

At its thickest point, the core appears as a localized shear within an altered damage zone laced with subsidiary faults several meters long (Fig. 10). The subsidiary faults cutting the core are in the same orientation and display the same sense of apparent separation on the outcrop. Based on Reidel shear geometries of offset aplitic fragments the motion across the fault is right reverse oblique.

The north side of the damage zone is tan to pink and the south side is light green to grey in color suggestive of chemical alteration adjacent to the fault core (Figs. 11 and 12) At its boundary there is a sudden change in color and grain size that marks the boundary of the fault core with the damage zone (Fig. 12). The damage zone contains an intensely fractured altered host rock that is laced with macroscale subsidiary faults. The altered host rock forms part of a damage zone 200-250 feet in thickness.

The third fault core exposure is located where the Mill Creek fault crosses the upper portion of Raywood Flat (Figs. 9 and 13). The outcrop is bisected by a creek and there is exposure on both sides. It is covered by fluvial gravels of very young age that have to be dug out to reach some of the faults. The gravels are separated by a fault from a green crush zone. At a lower structural level and across the stream, the same fault is seen separating two different types of altered host rock. Those altered rocks are thought to mark the damage zone of the Mill Creek fault also observed in Station 0 and Station 8.

The north side damage zone contains faults that have red clay zones bounded by deformed granodiorite with pink altered zones and it is laced with slicked iron-oxide stained surfaces. The red clay has striations, host rock inclusions, and is embedded with white clasts of unknown mineralogy. The south side damage zone has green gouge with

possible slicks. The most interesting faults at this location have 1-12 cm fault cores filled with gouge of different colors. The gouge is saturated with and has been probably altered by meteoric water. Faults with gouge are also among the longest features in the outcrop. They are also well foliated and sheared with much color variation.

4.2.2. South Transfer fault

Additionally, an unnamed fault was found on the north facing side of Mill Creek Canyon (Figs. 9 and 14). The trace of this fault projects southeast into Yucaipa Ridge but its exposure in the ridge was not observed. The fault zone is a gouge-clay mixture containing 5 cm long by 2 cm thick white clasts elongated parallel to the shear zone (Fig. 14). The gouge is friable and its fabric of slicked surfaces is highly variable.

4.2.3. Galena Peak fault

The fault zone structure of the Galena Peak fault was observed in the lower portion of Raywood Flat where it parallels the Mission Creek fault (Figs. 9). The fault core marked the boundary between an alluvial gravel deposit to the north from intensely fractured and foliated rock to the south (Fig. 13). The fault plane defined the boundary of a thin (10-15 cm) cataclasite layer of light gray color. The core was exposed such that a polished surface with grooves indicated the slip direction of the fault. Grain size was indistinguishable, unlike the host rock to the south or the gravel to the north. It is not clear whether the fault cuts through the gravel or the gravel was juxtaposed during deposition.

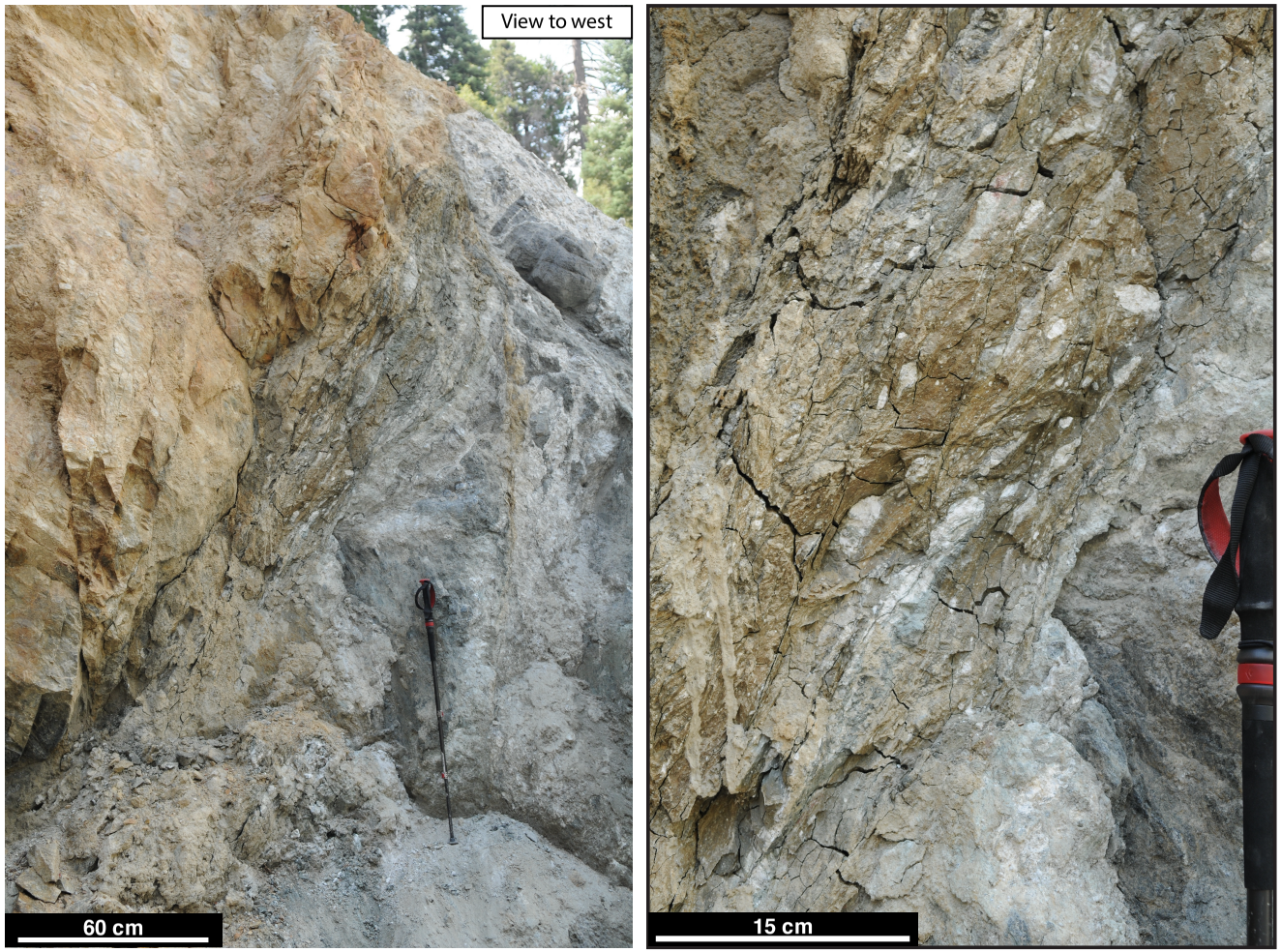

Fig. 14. View parallel to the strike of the Transfer fault core and damage zone. This fault exposure is located at Station 40 (Fig. 9). The fault core separates a relatively intact host rock from a heavily sheared host rock (left). Zoom in view shows matrix and entrained host rock clasts sheared in a direction parallel to strike (right).

Table 2
Description Rock type and thickness of fault core exposures by structural domain in the study area.

Domain	Station	Location	Rock type	Core thickness	Alteration Zone Thickness*,**	Total # of Fracture Measurements	Total # of Slip Vectors
Fault Cores	0	Mill Creek Canyon	C, UC	6 cm	200-300 m	25	19
	8	Mill Creek Canyon	C	30 cm	200 m	13	4
	33	Raywood Flat	G	12 cm	-	50	14
	53	Raywood Flat	UC?	20 cm	-	15	5

*Determined from satellite images. ** Alteration Zone refers to an area adjacent to the fault core whose texture and composition cannot be easily linked to the neighboring host rock.

Table 3
Outcrop size and measurements by structural domain in the Raywood Flat and Yucaipa Ridge regions.

Domain	Station	Location	Exposure Size	Dominant Lithology	Foliation	Total # of Fracture Measurements	Total # of Slip Vectors	Apparent Sense of shear
Straight Segment - GP,MiC	53	Raywood Flat	< 50 m*	-		15	5	2
	54	Raywood Flat	< 30 m*	-		18	15	-
Straight Segment - RWF	46	Raywood Flat	20 m	-		25	6	4
	33	Raywood Flat	< 20 m*	-		51	14	-
	56	Raywood Flat	< 10 m*	-		8	8	-
Straight Segment - GP	61-62-63-64	Yucaipa Ridge	< 150 m*	-		31	30	-
Straight Segment - MiC	67-68	Banning Canyon	< 20 m*	-		8	1	-

*In case of no direct measurement, the length of outcrop size is estimated.

4.3. Mesoscale Subsidiary Fault Fabrics

Subsidiary fault orientations are documented for different parts along the Mill Creek-Mission Creek stepover, particularly focusing on the large-scale bend and transfer faults of the Mill Creek fault in upper Mill Creek canyon. A total of 1128 subsidiary fault orientations were collected across 32 stations out of which only 993 subsidiary fault orientations were utilized from 24 stations to remove duplicative measurements and stations with insufficient representative measurements (Fig. 9, Table 1, Table 2, and Table 3). Slip vectors, and thus b-axes, were obtained for 637 of these subsidiary faults. Subsidiary fault fabrics are presented for each structural domain, within three regions: Mill Creek Canyon, Yucaipa Ridge, and Raywood Flat (Fig. 8).

The subsidiary fault orientations and kinematics have strong preferred orientations and kinematics. This is particularly well documented in outcrops where faults cut units with planar foliations. In some optimally oriented outcrop surfaces, particularly for those along the south-facing canyon wall of Mill Creek canyon in the domain north of the straight segment, east of the fault bend, conjugate fault geometries are evident (Figs. 15 and 16). Conjugate faulting is recognized in several other locations throughout the area.

The entire data set for each measurement station, used for the subsidiary fault fabric analysis, is recorded in Appendix A. Appendix A presents lower-hemisphere equal-area stereograms showing the fabric of the following groupings of data per station: poles to all faults, all slip vectors measured, all b-axes determined from the slip vectors, long faults, gouge and breccia zones, faults displaying iron-stained slip-surfaces, faults displaying epidote-lined slip surfaces, and faults displaying both epidote- and iron-

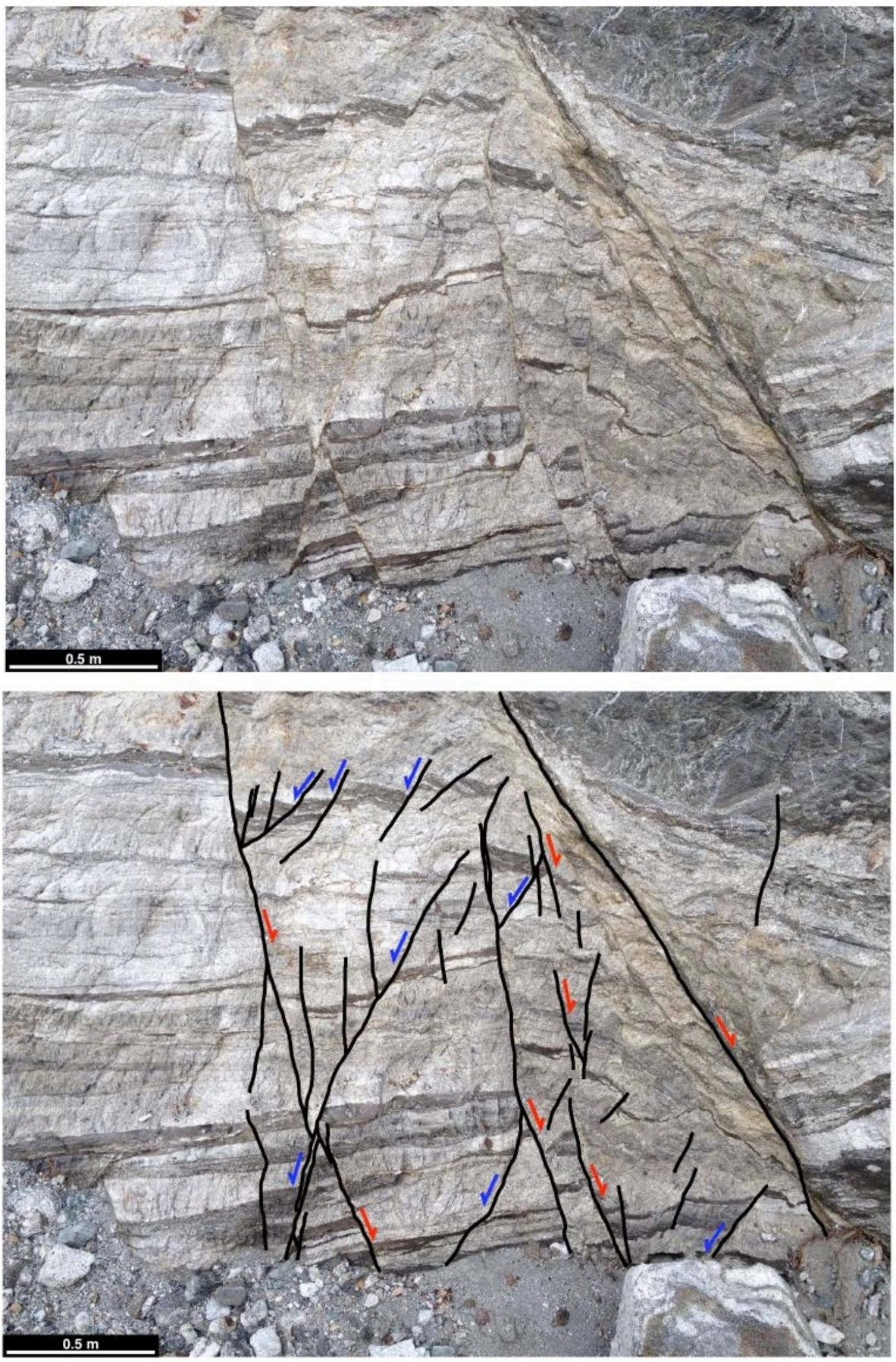

Fig. 15. Outcrop photograph of subsidiary faults. The photo shows a fractured outcrop at Station 10 (Fig. 9; top). An interpreted image shows distinct orientations and apparent sense of shear on subsidiary faults (bottom). The faults displace foliation layers in apparent right lateral offset (Red arrows) and apparent left lateral offset (Blue arrows).

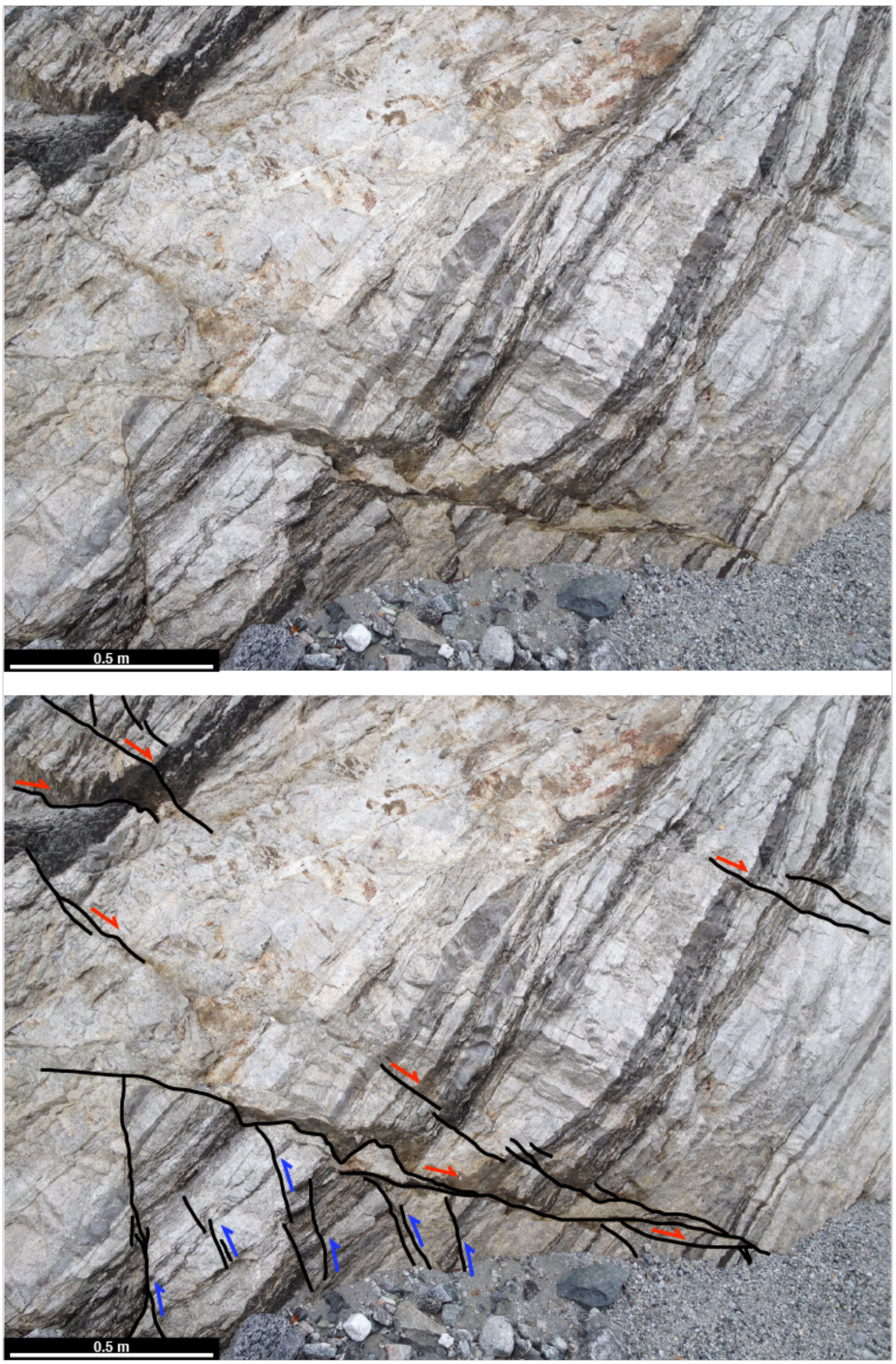

Fig. 16. Additional outcrop photograph of subsidiary faults. The photo shows a fractured outcrop at Station 10 (Fig. 9; top). An interpreted image shows distinct orientations and apparent sense of shear on subsidiary faults (bottom). The faults displace foliation layers in apparent right lateral offset (Red arrows) and apparent left lateral offset (Blue arrows)

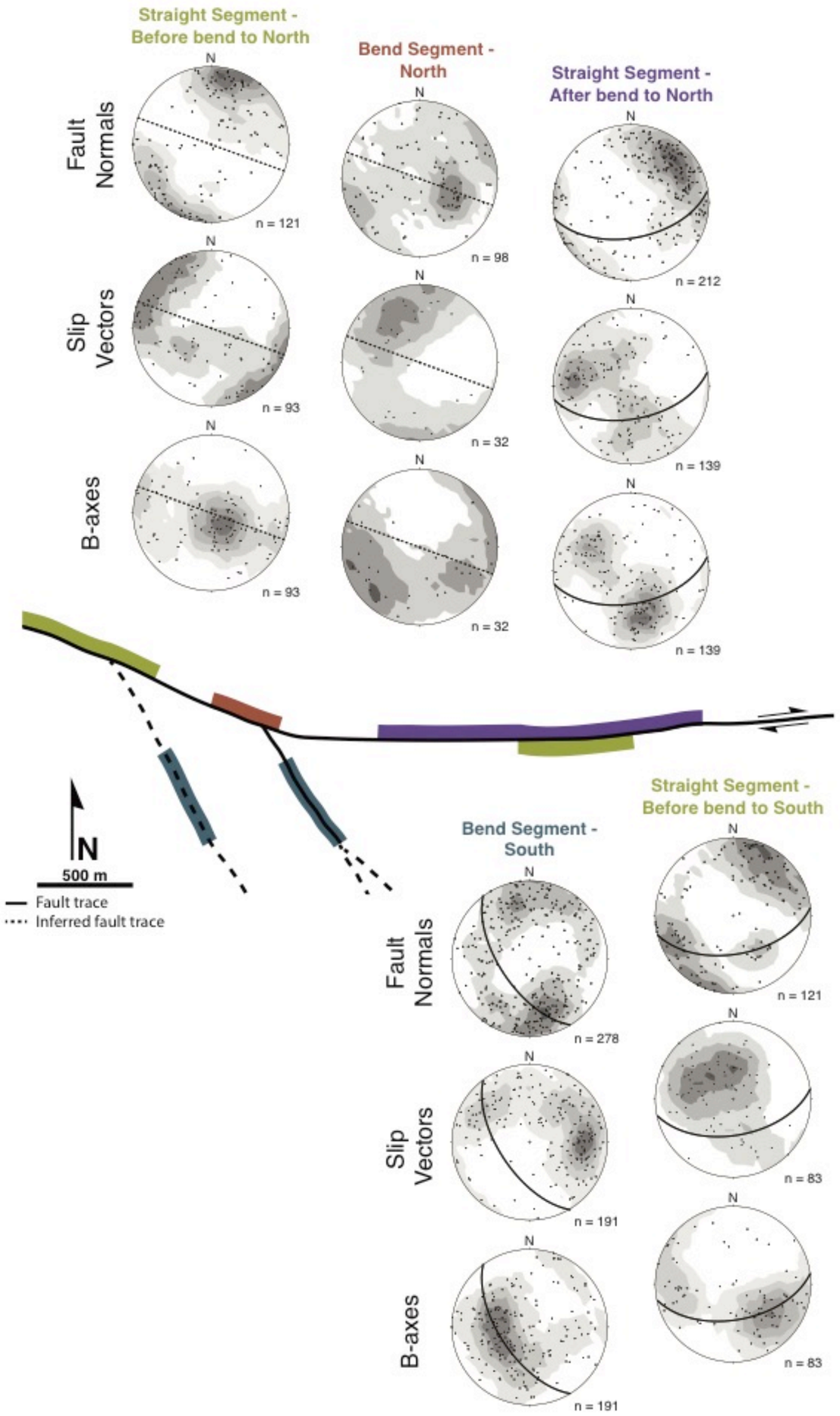

Fig. 17. Subsidiary fault orientations and kinematics in the Mill Creek canyon region. Equal-area, lower-hemisphere stereonet projections of poles, slip vectors, and b-axes to subsidiary faults along the Mill Creek fault damage zone. Stereonets show north at the top, average Mill Creek fault orientation (great circles), and number of data. A map of the trace of the Mill Creek fault in the middle of the image is colored by structural domains and shows the relative position of the data collected. The domains highlight areas before the bend (green), within the bend (red), after the bend (purple), and south of the bend (blue).

stained surfaces. The data from the individual stations are grouped into larger structural domains (Fig. 8). The combined data sets of subsidiary faults, and of fault kinematic indicators (i.e., the slip vectors and b-axes), per structural domains, are presented in the following sections (Fig. 17).

4.3.1. Mill Creek Canyon Region

4.3.1.1. North of the Straight Segment Before the Bend

The orientations and the kinematic indicators of subsidiary faults in this domain show strong preferred orientations (Fig. 17). Fault poles define a maximum concentration characterized by a low-magnitude inclination that trends in the north-northeast direction, with an additional weaker extension of the concentration to include west-southwesterly trends. The slip vectors are largely subhorizontal with northwest trends, ranging from due west to north. B-axes define a strong point maximum centered just southeast of vertical. Taken together, these fabrics indicate that the subsidiary faults in this domain are characterized as vertical to steeply dipping, striking northwesterly, and are dominated by strike-slip motion. These data indicate that most subsidiary faults in this damage zone domain are subparallel to the Mill Creek fault. Notably, there is a small cluster of faults with slip vectors that steeply dip to the southwest; most of these dip-sip faults were measured from the westernmost station (SB1W) within this domain (Appendix A).

4.3.1.2. North of Bend Segment

The orientations and the kinematic indicators of subsidiary faults in this domain show strong preferred orientations (Fig. 17). Fault poles define a diffuse concentration with

two different pole clusters. The first fault pole cluster is characterized by a moderately steep inclination that trends in the east-southeast direction. The slip vectors plunge slightly northwesterly, ranging from due west to north. B-axes define a broad range of orientations ranging from due west to south-southwest. The second fault pole cluster is largely subhorizontal and is defined as a weaker concentration that includes northeast and southwest trends. The slip vectors plunge slightly in to the north but are generally absent in this set. B-axes define a small cluster that is moderately dipping in a southeast trend. Taken together, these fabrics indicate that the subsidiary faults in this domain are characterized as vertical to shallowly dipping, striking northwesterly and north-northeasterly, and are dominated by oblique-slip motion. Additionally, there is an increased amount of scatter in subsidiary fault orientation that is not observed in any other structural domain.

Notably, the broad southwest b-axis cluster is exclusively formed from faults belonging to the shallowly dipping fault set. However, the orientations of faults belonging to the other b-axis cluster cannot be attributed to the northwest set alone (Appendix A).

4.3.1.3. North of the Straight Segment After the Bend

The orientations and the kinematic indicators of subsidiary faults in this domain show strong preferred orientations (Fig. 17). Fault poles define a concentration characterized by a strong maximum of low-magnitude inclination that trends in the northeast direction, with an additional weaker extension of the concentration to include northerly and south-southeasterly trends. The slip vectors define a concentration characterized by two

distinct clusters of moderate- to high-magnitude inclinations, one that trends in the northwest direction and one with south-southeasterly trends. B-axes define two strong point maxima with moderate-magnitude inclinations, one that trends northwest, and one that trends south-southeast. Taken together, these fabrics indicate that the subsidiary faults in this domain are characterized as vertical to moderately dipping, striking northwesterly, and are dominated by oblique-slip motion. These data indicate that most subsidiary faults in this damage zone domain are at a moderate angle to the Mill Creek fault. Notably, it is visible from close-up outcrop pictures of one of the stations in this structural domain (SB10; Appendix A) that faults exhibiting LL and RL apparent separation dip in opposing directions (Figs. 15 and 16). The pictures also show that one set, specifically the one displaying RL apparent separation, appears to be longer than the other one.

4.3.1.4. South of the Straight Segment Before the Bend

The orientations and the kinematic indicators of subsidiary faults in this domain show strong preferred orientations (Fig. 17). Fault poles define a maximum concentration that trends north-northwest. This concentration is characterized by a low- to moderate-magnitude inclinations trending in the northeast and southwest direction, ranging from north-south to east-west. An additional weaker concentration of fault poles plunges moderately with southwesterly trends. The slip vectors are largely plunging moderately with northwest trends, ranging from due north to west-northwest. B-axes define a strong point maximum plunging moderately with southeast trends, with an additional smaller concentration plunging slightly with westerly trends. Taken together, these fabrics

indicate that the subsidiary faults in this domain are characterized as vertical to steeply dipping, striking northwesterly, and are dominated by oblique-slip motion, but with an additional set striking northwest and dipping shallowly to the northwest. These data indicate that most subsidiary faults in this damage zone domain are at a moderate angle to the Mill Creek fault.

4.3.1.5. South of the Bend Segment

The orientations and the kinematic indicators of subsidiary faults in this domain show strong preferred orientations with significant scatter (Fig. 17). Fault poles define two concentrations characterized by a low-magnitude inclinations; one that trends in the north direction, ranging from north-northwest to northwest, and another one that trends in the south-southeast direction, ranging from southwest to southeast. Both concentrations have an additional weaker extension that includes westerly and easterly trends. The slip vectors define two concentrations mostly of subhorizontal to low-magnitude inclinations with north-northeast trends that extend to the northeast, and with northwest trends. B-axes define a broad strong point maximum centered south-southwest of vertical. Taken together, these fabrics indicate that the subsidiary faults in this domain are characterized as vertical to steeply dipping, largely striking north-northeasterly, and are dominated by strike- and oblique-slip motion.

4.3.1.6. Mill Creek Fault Core

The orientations and the kinematic indicators of subsidiary faults in the Mill Creek fault core and immediately adjacent damage zone show strong preferred orientations (Appendix A). Fault poles define a strong concentration characterized by a low-

magnitude inclination that trends in the north-northwest direction, with an additional weaker concentration that includes a range of trends from southwest to southeast. The slip vectors are mixed between moderate-magnitude inclinations with no particular preferred orientation and subhorizontal inclinations with north-northeast and easterly trends. B-axes not define a strong point maximum of preferred orientation. Taken together, these fabrics indicate that the subsidiary faults in this domain are characterized as moderately dipping, largely striking northwesterly, and represent strike- and oblique-slip motion. These data indicate that most subsidiary faults in this damage zone domain are subparallel to the Mill Creek fault. Notably, the gouge and cataclasite zones exhibit a very strong fabric parallel to the Mill Creek fault. The slip vectors and b-axes for those faults are mixed between strike- and oblique-slip kinematics similarly to the overall character of the fabric in this structural domain.

4.3.2. Yucaipa Ridge Region

4.3.2.1. North of the Straight Segment of the Galena Peak Fault

The orientations and the kinematic indicators of subsidiary faults in this domain show strong preferred orientations (Fig. 18). Fault poles define a maximum concentration characterized by a low-magnitude inclination that trends in the southwest direction, with an additional weaker extension of the concentration to include northeast trends. The slip vectors are largely subhorizontal with southeast trends, ranging from northeast to south-southeast. B-axes define a strong point maximum centered just northwest of vertical. Taken together, these fabrics indicate that the subsidiary faults in this domain are cha

racterized as vertical to steeply dipping, striking northwesterly, and are dominated by

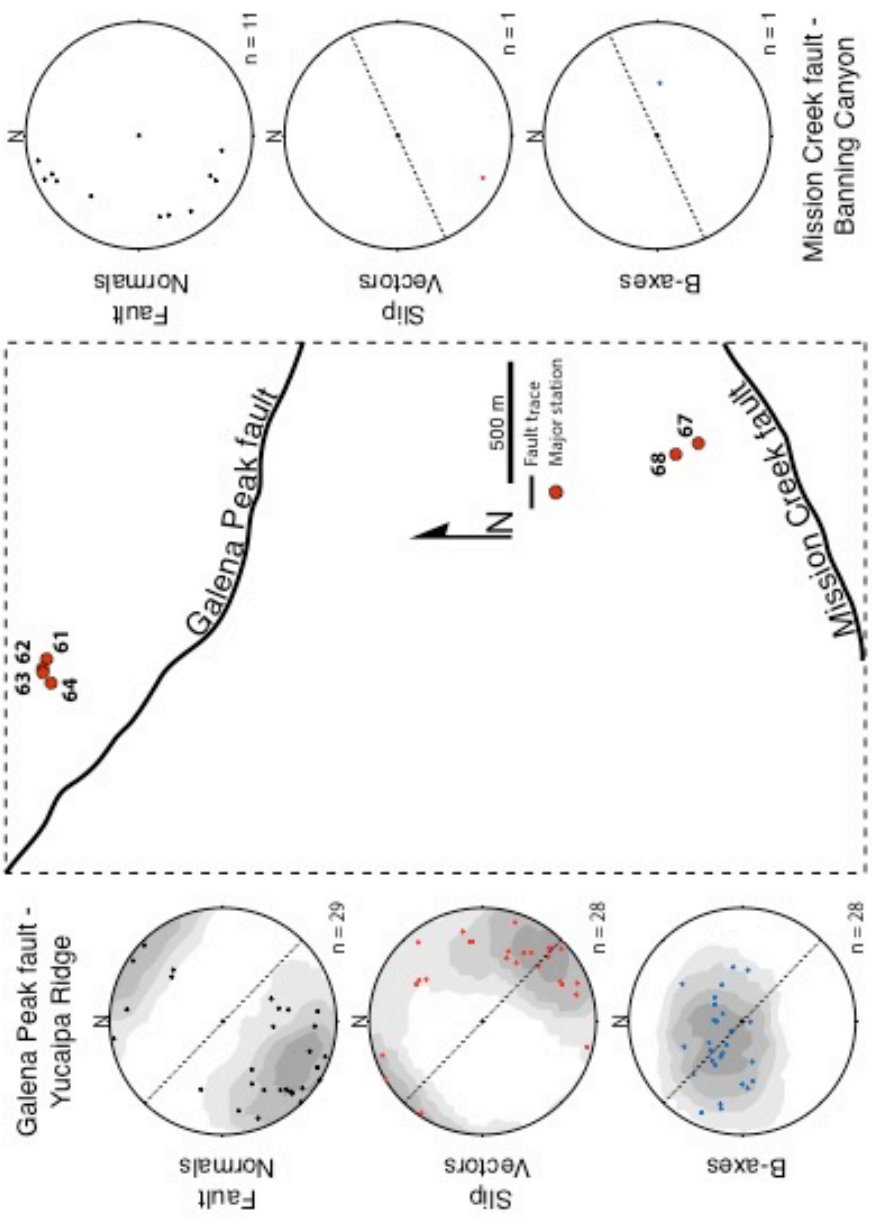

Fig. 18. Subsidiary fault orientations and kinematics in the Yucaipa Ridge region. Equal-area, lower-hemisphere stereonet projections showing poles, slip vectors, and b-axes to subsidiary faults along the Galena Peak fault and Mission Creek fault damage zones. Stereonets show north at the top, average fault orientation (great circles), and number of data. A map of the trace of the faults in the middle of the image.

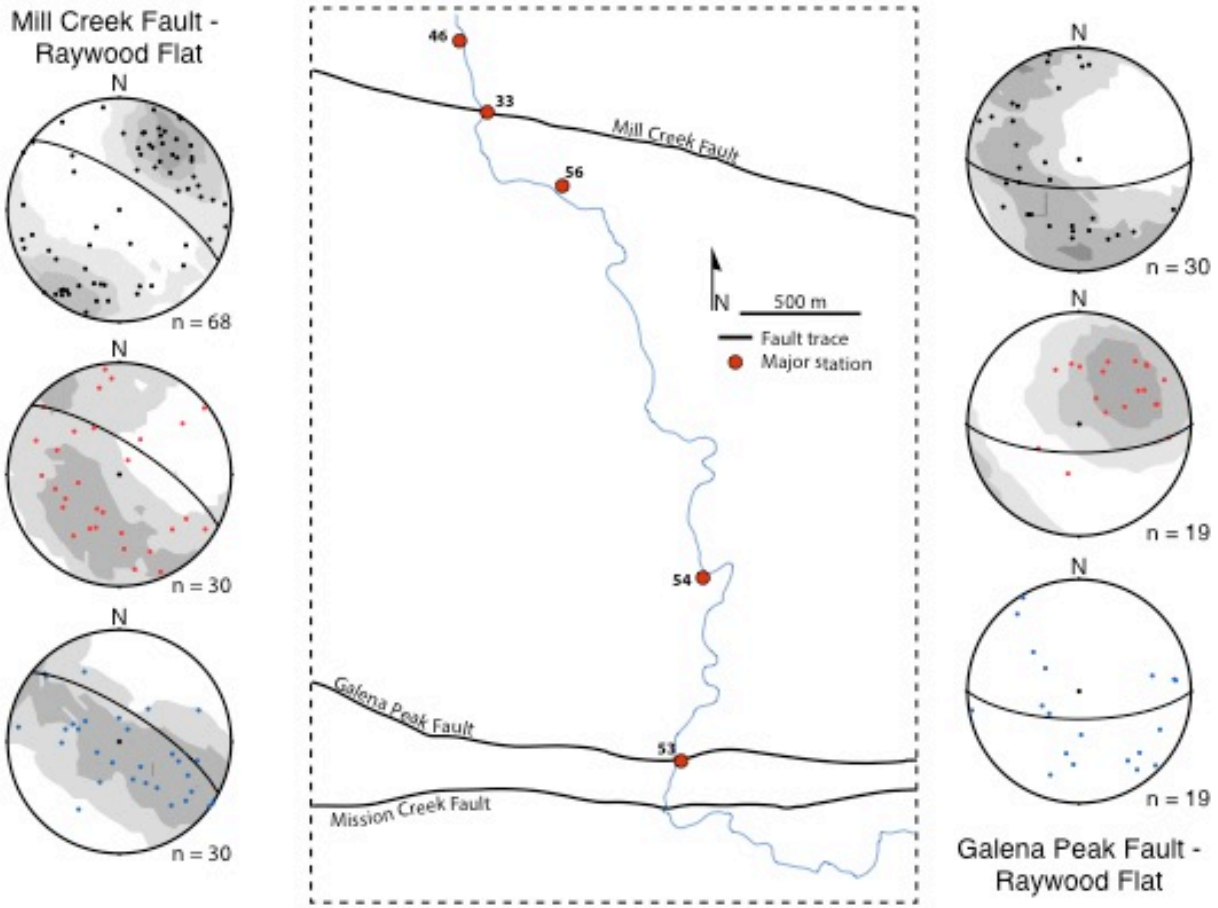

Fig. 19. Subsidiary fault orientations and kinematics in the Raywood Flat region. Equal-area, lower-hemisphere stereonet projections showing poles, slip vectors, and b-axes to subsidiary faults along the Mill Creek fault and Galena Peak fault damage zones. Stereonets show north at the top, average fault orientation (great circles), and number of data. A map of the trace of the faults in the middle of the image.

strike-slip motion. These data indicate that most subsidiary faults in this damage zone domain are subparallel to the estimated orientation of Galena Peak fault.

4.3.2.2. North of the Straight Segment of the Mission Creek Fault

The orientations of subsidiary faults in this domain show weakly preferred orientations (Fig. 18). Fault poles in this structural domain are characterized by two groups of low-magnitude inclination that trend north-northwest and southwest, but are not sufficient to define a statistical concentration. No significant kinematic indicators were recorded for this structural domain. The north-northwest trending poles are parallel to the estimated orientation of the Mission Creek Fault at this structural domain.

4.3.3. Raywood Flat Region

4.3.3.1. North of the Straight Segment of the Galena Peak and Mission Creek Faults

The orientations and the kinematic indicators of subsidiary faults in this domain show moderately preferred orientations (Fig. 19). Fault poles define a statistical concentration characterized by low-magnitude to steep inclinations with trends that define a great circle girdle whose pole plunges 45° towards the northeast direction. The slip vectors define a strong point maximum centered northeast of vertical. However, b-axes do not define a statistical concentration. Taken together, these fabrics indicate that the subsidiary faults in this domain are characterized as vertical to shallowly dipping, striking northwesterly, and are dominated by strike- and oblique-slip motion. These data indicate that a small number of subsidiary faults in this damage zone domain are

subparallel to the Galena Peak fault. Notably, faults that strike east-west, closest to the Galena Peak fault (SB53), show nearly horizontal slip vectors highly indicative of strike-slip motion (Appendix A). The other north-northwest and north-northeast striking faults (SB54) exhibit predominantly oblique-slip motion (Appendix A).

4.3.3.2. North and South of the Straight Segment of the Mill Creek Fault

The orientations and the kinematic indicators of subsidiary faults in this domain show strong preferred orientations (Fig. 19). Fault poles define a maximum concentration characterized by a low- to moderate-magnitude inclination that trends in the north-northeast direction, with an additional weaker extension of the concentration to include east-northeast trends. The slip vectors are defined by moderate-magnitude inclinations that trend along a great circle girdle whose pole plunges approximately 45° towards the northeast direction. B-axes are also defined by a great circle girdle whose pole plunges slightly towards the northeast direction. Taken together, these fabrics indicate that the subsidiary faults in this domain are characterized as vertical to moderately dipping, striking northwesterly, and exhibit a mix of strike-, oblique- and dip-slip motion. These data indicate that most subsidiary faults in this damage zone domain are subparallel to the Mill Creek fault.

4.4. Distribution of Mineral-filled Subsidiary Faults

There are two main types of mineral fill and stained surfaces for the subsidiary faults within the study area. The first major type of mineral fill is epidote and the second is faults stained with iron oxide. The majority of epidote-filled faults are grooved and the iron-stained faults display slickenlines (Fig. 20).

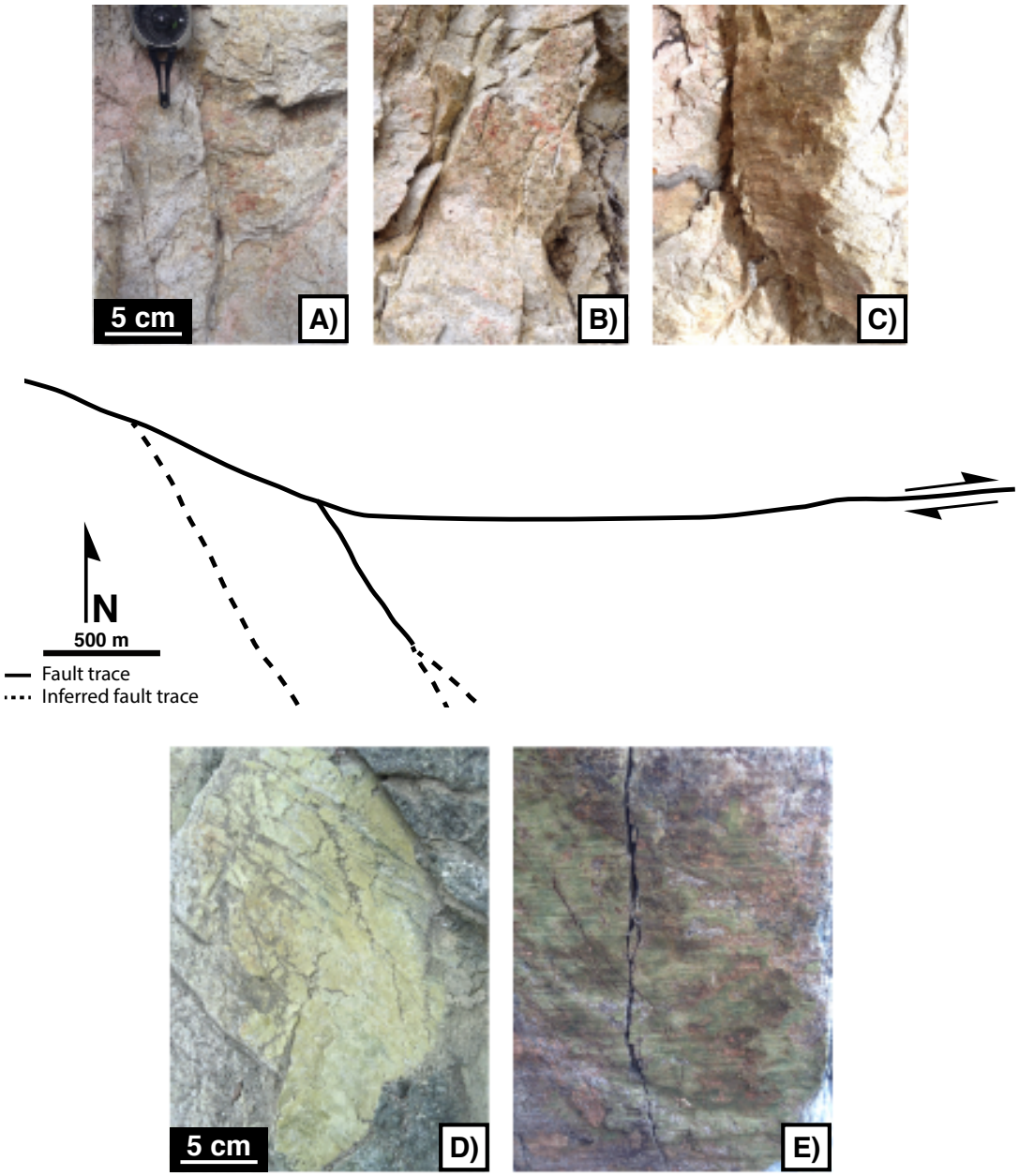

Fig. 20. Distribution of mineral-coated subsidiary faults in the Mill Creek canyon region. Iron-stained or -slickensided surfaces (a,b,c) are, in most cases, found north of the Mill Creek fault. Epidote-filled (d) or -grooved surfaces (e) are found south of the Mill Creek fault.

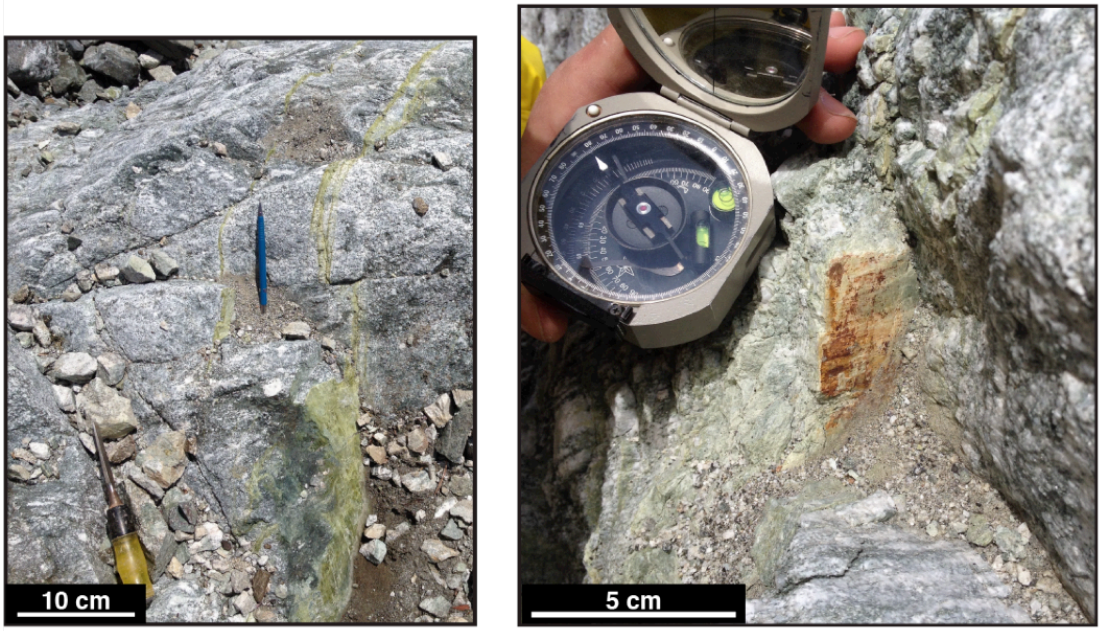

Fig. 21. Overprinting relationships in the Mill Creek canyon region. Photos document timing relationships between different kinds of subsidiary faults and within subsidiary faults. Subsidiary faults with no mineral fill cross-cutting epidote-filled faults (left). Epidote-filled fault overprinted by iron-staining (right).

The distribution of mineral-filled subsidiary faults is markedly different across the Mill Creek fault in Mill Creek canyon. The presence of epidote is essentially absent on the north side of the Mill Creek fault, but is ubiquitous on the south side, whereas the iron staining along the fault surfaces is typical on the north side of the Mill Creek fault, and less prevalent on the south side of the fault (Fig. 20). Because of this relationship, observations of both kinds of mineral fill at the same station are rare. In the cases where epidote-filled faults and iron-slickenlined faults are present at the same station, however, the epidote-lined faults are always overprinted by iron-staining or by iron-stained slickenlines (Fig. 21). Instances of overprinting show that the rake of slickenlines for both mineral-fill types is parallel for most of the recorded cases, but in some cases the rake may diverge up to ~20°. Overprinting also is indicated by non-mineral-filled faults cross-cutting epidote-filled faults (Fig. 21).

5. DISCUSSION

The identification of distinct subsidiary fault sets and associated kinematics in each structural domain are used to guide the interpretation of deformation and principal stress directions at the time of faulting. These interpretations can be used with observations of cross-cutting relations to test the hypothesis that the deformations and principal stress orientations in the damage zones of the major faults have changed in both space and time, largely as a function of the fault geometry of the master fault.

This deformation and stress analysis cannot be based entirely on the Andersonian model of faulting (Anderson, 1951), because many domains contain or are dominated by three dimensional strain manifested by oblique-slip faulting. Nonetheless, as was documented in some ideally oriented outcrops, conjugate sets are common in the field area. Conjugate faults consist of two distinct and generally related fault sets that have complimentary slip vectors, often not perfectly orthogonal, and which share a common b-axis orientation. To carry out this analysis it is useful to produce a synoptic diagram for each domain, which is a visual representation of the geometry of multiple structural elements. Figure 22 presents an example synoptic representation of a master fault and an associated array of subsidiary faults that form a conjugate fault set related to the master fault. These features are represented in a lower-hemisphere equal-area projection onto a horizontal plane.

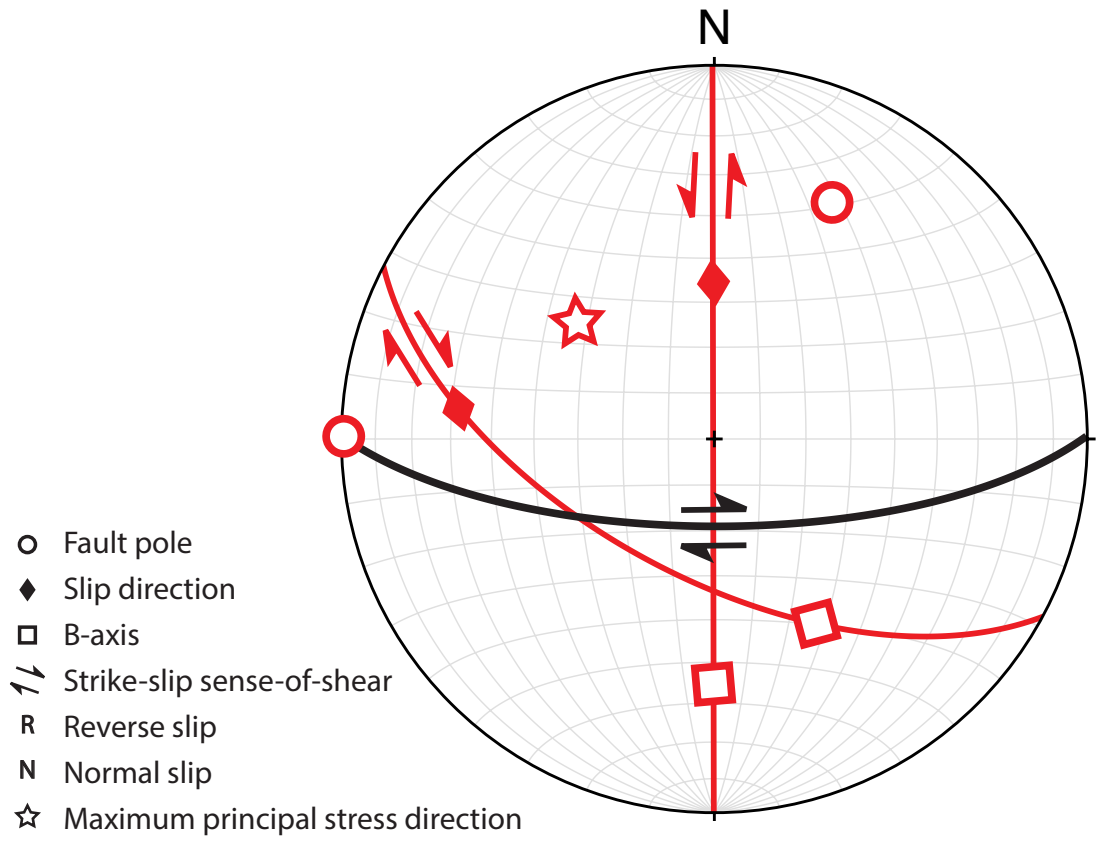

Fig. 22. Synoptic diagram example of a fabric distribution. Equal-area, lower-hemisphere stereonet projection showing average poles (hollow circles), slip vectors (diamonds), and b-axes (hollow boxes) subsidiary fault sets. Orientation of the main fault (black great circle) with sense of shear. The kinematics of subsidiary fault sets (red great circles) display a typical conjugate set relationship. The maximum principal stress direction and sense of shear is interpreted from such relationship.

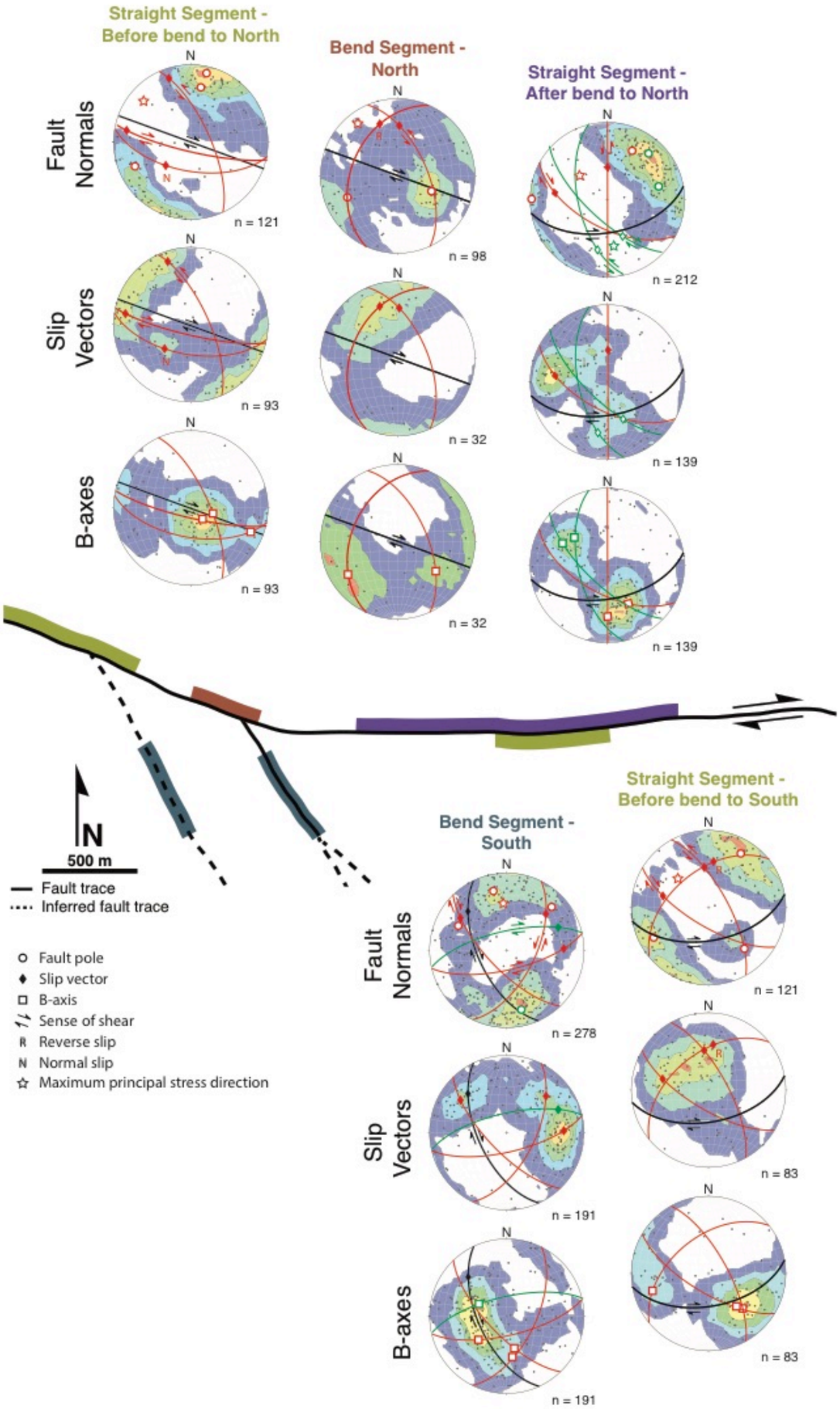

Fig. 23. Synoptic diagram of the subsidiary fault orientations and kinematics in the Mill Creek Canyon region. Equal-area, lower-hemisphere stereonet projections of poles, slip vectors, and b-axes to subsidiary faults along the Mill Creek fault damage zone superposed by synoptic diagram interpretations. Stereonets show north at the top, average Mill Creek fault orientation (great circles), and number of data. A map of the trace of the Mill Creek fault in the middle of the image is colored by structural domains and shows the relative position of the data collected. The domains highlight areas before the bend (green), within the bend (red), after the bend (purple), and south of the bend (blue).

5.1. Deformation and Stress Along the Mill Creek and Galena Peak Faults

5.1.1. North of the Straight Segment Before the Bend

The synoptic diagram for the domain of the Mill Creek fault shows two major subsidiary fault sets and one minor fault set (Fig. 23). Most of the faults in the three sets of faults display iron-stained slickenlines; these slickenlines define the orientation of slip that occurred on the subsidiary fault surfaces. The two major faults sets form a conjugate geometry of west-northwest and north-northwest striking faults with opposite directions of dip, as indicated by the two strong concentrations of fault poles. One of the conjugates is nearly parallel to the plane of the Mill Creek fault, and the other is antithetic to the Mill Creek fault. The two near-horizontal slip-vector concentrations, and one common b-axis concentration for these faults indicate that they represent a conjugate, strike-slip fault array. The bisector of the dihedral angle of the conjugate set is 51˚, and the inferred orientation of the maximum principal compressive stress at fault formation plunges approximately 20˚ in the N50W direction. (Fig. 23).

The minor subsidiary fault set is interpreted as a right-lateral normal-slip fault set. This interpretation is compatible with the orientation of the maximum principal compressive stress determined for the conjugate strike-slip array, if the sub-vertical principal compressive stress ($\sim\sigma_v$) is close in magnitude to the maximum principal compressive stress for this domain.

5.1.2. North of the Bend Segment

The synoptic diagram for this domain of the Mill Creek fault displays two significant subsidiary fault sets (Fig. 23). The most prominent fault set is sub-vertical with a north-

northwest strike. Slickenlines and sense-of shear information on the faults in this domain were sparse, but based on the angle between the prominent fault set and the master Mill Creek fault, it appears that the prominent fault set forms an antithetic conjugate to the Mill creek fault. The fault set then is very similar to the relationship seen in the damage zone along the straight-segment to the west-northwest. The second subsidiary fault set is composed of shallowly dipping faults with slip vectors and b-axes indicative of oblique-reverse kinematics. The shallowly dipping faults most-often display iron-stained slickenlines, which allow one to determine the slip direction.

The lack of kinematic data on the sub-vertical set may be explained by the biotite orthogneiss lithology at the particular station where faults of this orientation are displayed within this structural domain. It is clear that the surfaces within the orthogneiss are faults, but the strong mineral lineations and foliations in the rock, appear to inhibit the formation or preservation of slip lineations, in contrast to the monzonite rock type.

The two sets of faults in this domain form a dihedral angle of approximately 90˚, which is greater than typically expected for conjugate faulting, and the b-axes of these fault sets are not collinear, so the two sets can not be considered conjugates. The measurement station (SB9) that represents the fault data for the bend region is located on the western edge of the bend segment. Because of the position of SB9, it is assumed that the fabric noted in the bend domain could reflect that formed when these rocks were moving along the straight fault segment to the west. If so, one would expect to see subsidiary faults that parallel to the strike of the Mill Creek fault, but is not observed in

the bend domain. One possible reason that Mill-Creek-parallel subsidiary faults miht not be observed I because they would also be parallel to the outcrop surfaces in this domain. As in the previously discussed domain, I suggest that the Mill Creek fault represents one of the sets of a conjugate array in this domain, suggesting a dihedral angle of approximately 53˚, with a maximum principal compressive stress axis that plunges approximately 20˚ to the N40W direction (Fig. 23). The set of reverse-oblique slip faults that dip to the northwest are compatible with this inferred principal compressive stress direction, but in contrast to the straight-fault domain to the northwest, implies that the sub-vertical principal compressive stress ($\sim\sigma_v$) is the minimum principal compressive stress for this domain.

5.1.2.1. North of the Straight Segment After the Bend

The synoptic diagram for this domain of the Mill Creek fault shows two conjugate sets (Fig. 23). The first conjugate set is expressed all stations within the domain and consists of west-northwest and north-northwest striking faults that generally dip to the west. The b-axes for this set are inclined to the southeast, consistent with oblique-slip kinematics. This conjugate set has a dihedral angle 54° with a maximum compressive stress direction of approximately 50° towards 310° (Fig. 23). The second conjugate set only occurs at one station furthest east of the bend (SB17), and is composed of subvertical, north-northwest and northeast striking faults that dip to the southwest. The b-axes of these faults coincide, and plunge to the northwest, also indicating oblique-slip kinematics. The second conjugate set has a dihedral angle of 40° with a maximum compressive stress direction that plunges approximately 30°, towards 150° (Fig. 23).

Long subsidiary faults form part of the set of northwest-striking faults in both conjugate sets, which is demonstrable by the long faults displaying b-axes in both the northwest and southeast preferred orientations. The iron-stained faults dominate the set of faults having northwest-trending b-axes, suggesting that the long faults record the most recent faulting event, as movement along them would cut other faults in their path. The gouge- and breccia-bearing faults predominately belong to the faults with southeast trending b-axes, which suggests that this conjugate set represents the earlier, and longer-lived stage of fault development.

5.1.2.2. South of the Straight Segment Before the Bend

The synoptic diagram for this domain of the Mill Creek fault shows one dominant conjugate set and another minor set of faults (Fig. 23). The dominant conjugate set is formed by sub-vertical faults of north-northwest and west-northwest strikes and opposing dip directions and has a dihedral angle of 40°. The b-axes of this set define a single preferred orientation that trends southeast. The minor fault set in this domain is formed by faults having northeast strikes and that dip to the northwest. The b-axes of this set are slightly inclined to the west, indicating a significant dip-slip component. The conjugate set implies a maximum compressive stress direction of approximately 45° towards 315° (Fig. 23).

The faults containing epidote faults occur in all three of the fault sets, while long faults mostly occur in the northwest striking faults of the conjugate set. Gouge and breccia faults occur in both of the conjugate fault sets.

5.1.2.3. South of the Bend Including the Transfer Faults

The synoptic diagram for this domain of the Mill Creek fault bend shows four distinct sets of faults, two of which constitute a conjugate set (Fig. 23). The distribution contains two dominant subsidiary fault sets that strike east-northeast and dip to the north and to the south. The slip vectors and b-axes of these faults indicate that these sets are primarily composed of strike-slip faults. The second conjugate set is composed of oblique-slip, moderately dipping faults, that have a dihedral angle of approximately 90° and the maximum compressive stress oriented approximately 40° towards 355° (Fig. 23).

Mineral fill distinguishes the dominant fault sets, where most of the epidote filled faults dip north or in the conjugate set, and the iron-stained slickenline fault surfaces occur in the major fault set that dips south. Most long faults belong to the dominant sets, but the orientation of gouge and breccia faults predominantly occur in the conjugate set of faults. These relations suggest that the conjugate faults and the northward dipping probably experienced greater displacements early in the deformation history, during which time they developed gouge and breccia zones. They were probably longer than they currently appear, but were cross-cut by more recent faulting events that are recorded by the now major set of south-dipping iron-stained faults and by the larger transfer faults.

5.2. The Role of Fault Geometry on Stress and Strain in the Damage Zone

Field and laboratory description of fault roughness have demonstrated that faults have fractal roughness that extend over multiple scales of observation (Power et al., 1987; Power and Tullis, 1991; Sagy and Brodsky, 2009). The stress state associated with

variations in fault roughness has been studied through analytical and numerical modeling (e.g., Saucier et al., 1992; Chester and Fletcher, 1997; Chester and Chester, 2000; Dunham et al., 2011). The analytical models considering the elastic and viscous deformation of the damage zone associated with faults of different roughness characteristics show that stress orientations and magnitudes adjacent to the master fault surface are modified with respect to the far-field applied stress (Saucier et al., 1992; Chester and Fletcher, 1997; Chester and Chester, 2000). For instance, (Chester and Fletcher, 1997) show that if the damage zone is modeled as a mechanically anisotropic medium, the anisotropy possibly resulting from a pre-existing set of closely-spaced subsidiary faults, that as this medium moves into a bend region, the magnitude of the stress change increases with increasing anisotropy and angularity of the bend. The results of the analytical models are supported by numerical models, which not only show that bends produce localized plastic strain near fault bends, but also suggest a dependence of deformation intensity on the orientation of the far-field maximum principal compressive stress (e.g., Dunham et al., 2011). Therefore, an assumption of homogeneous stress state along a geometrically irregular fault surface is invalid.

Changes in the state of stress are supported by field observations at the mesoscale (e.g., Becker, 2012) and at the microscale (e.g., Griffith et al., 2010). Becker (2012) characterized the subsidiary fault fabric along an isolated bend of similar size in the North Branch San Gabriel fault. This fault is an ancient trace of the San Andreas system in southern California that accommodated between 16 and 21 km of right-lateral strike-slip motion when it was active, and now is exhumed to about 3 km depth. Becker (2012)

found that the subsidiary fault orientations along the long straight segments of the San Gabriel fault are similar on both sides of the fault, and on both sides of the bend, indicating simple strike-slip kinematics, regardless of whether the damage zones had traveled through the bend or not. The fabrics within the bend, however, display distinct differences relative to the straight segments. This finding is different than the damage zone of the Mill Creek fault in Mill Creek canyon, and is interpreted to indicate that the San Gabriel fault was subjected to a much simpler stress state when it was active. Griffith et al. (2010) characterized the microcrack distribution along the non-planar strike-slip Lobbia fault in the Lake Edison Granodiorite in the Sierra Nevada Mountains. Their work shows that the orientation distribution of microfractures also markedly changes in the bend region of the damage zone and the that intensity of microfractures suggest that significant inelastic strain energy was dissipated near the master fault surface in response to movement past the irregular fault geometry.

The change in fault orientation in Mill Creek canyon, referred to as the bend in the fault, is defined by a 20˚ change in strike that is interpreted to occur over less than 250 m (Fig. 9). Based on the mechanical models referenced above, this pronounced change in strike should produce a rotation of the principal stress axes, and is consistent with the subsidiary fault fabric reported herein. The Mill Creek fault is concealed by alluvium, with the exception of two outcrops in Mill Creek canyon (Figs. 11 and 12). These outcrop exposures of the faults show that the orientation of the fault, changes from a near vertical orientation, west of the bend, to a much shallower dip of 50-60˚ south, east of the bend (Figure 24). This change in dip is consistent with the subsidiary fault fabric

for this eastern domain, and is illustrated in a schematic cross section shown in Figure 24. The effect that such geometry posses on the subsidiary fault fabric is reflected by the stress interpretation of conjugate sets (Fig. 23). The orientation of the maximum compressive principal stress is nearly horizontal west of the bend where the fault is near vertical. The maximum compressive principal stress changes in orientation closer to and east of the fault bend from a nearly horizontal in the northwest direction to plunging 45° in the northwest direction (Fig. 23). This change in stress orientation may be related to the change in dip of the fault from vertical to 50° - 60° dip to the south near and east of the bend. Figure 24 shows a schematic cross-section of the stress orientation relative to the fault trace illustrating the interpretation.

5.3. Effects on the Subsidiary Fault Fabric

5.3.1. Effects of Fault Orientation

The Mill Creek Fault is interpreted to have accumulated 8.7 km of right-lateral slip (Kendrick et al., 2015) and displays a prominent fault bend as observed in Mill Creek Canyon. The effect that such geometry posses on the subsidiary fault fabric is reflected by the stress interpretation of conjugate sets (Fig. 23). The orientation of the maximum compressive principal stress is nearly horizontal west of the bend where the fault is near vertical. The maximum compressive principal stress changes in orientation closer to and east of the fault bend from a nearly horizontal in the northwest direction to plunging 45° in the northwest direction (Fig. 23). This change in stress orientation may be related to the change in dip of the fault from vertical to 50° - 60° dip to the south near and east of

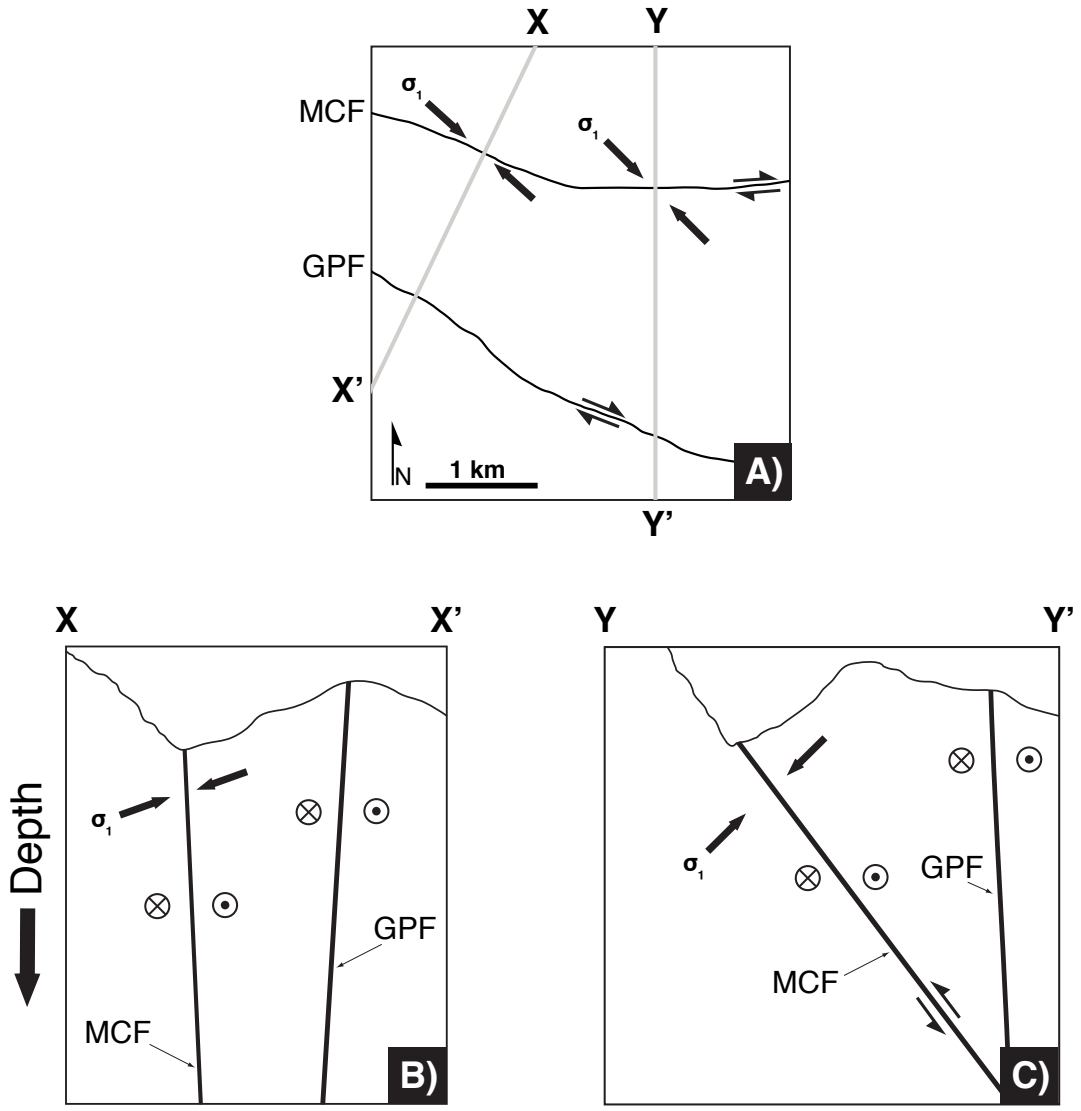

Fig. 24. Map view and schematic cross sections perpendicular to the Mill Creek fault in Mill Creek canyon. (A) Map view of the Mill Creek fault (MCF) and Galena Peak fault (GPF) showing the locations of the cross sections oriented perpendicular to the Mill Creek fault west of the bend (X-X'), and east of the bend (Y-Y'). This map view also shows the trend (~N45W) of the maximum compressive stress, σ_1, interpreted from the subsidiary fault data (Fig. 23). (B) Cross section X-X', showing the strike-slip component of motion on the Mill Creek fault by the x (away) and dot (towards) symbols, and the plunge (~20˚ NW) of σ_1 projected into the cross section plane. (C) Cross section Y-Y', showing the strike-slip component of motion on the Mill Creek fault by the x (away) and dot (towards) and the thrust component of motion (arrows on the MCF), and the plunge (~45˚NW) of σ_1 projected into the cross section plane.

the bend. Figure 24 shows a schematic cross-section of the stress orientation relative to the fault trace illustrating the interpretation.

5.3.2. Effects of the Fault Bend

The subsidiary fault fabric on the straight segment before the bend to the north of the fault reflects strike-slip kinematics associated with a steeply dipping Mill Creek fault (Fig. 23). The fabric changes in orientation and kinematics as it approaches the bend reflected by the presence of a shallowly dipping set within the bend segment. This set is exclusive to the bend segment north of the fault and shows highly left-lateral oblique-slip reverse faulting (Fig. 23) which are interpreted to reflect interaction with the geometry of the fault bend. The fact that most slickenlines of such set reflect oblique-slip, and rarely any strike-slip, kinematics is interpreted to reflect that the most recent activity is recorded in the iron-slicked fault surfaces.

As the rock leaves the bend region north of the fault, very shallow gouge and breccia faults present within the bend segment are still observed in the straight segment after the bend to the north (Station 10) but do not match the dominant fault set. At the same time, there is development of a conjugate set in Station 10 (Fig. 23; southeast-trending b-axes). During such process, the initial conjugate set of faults slipped enough to generate fault rock material and develop long subsidiary faults. With continued slip, a change of stress state is interpreted from a secondary conjugate set (Fig. 23; northeast-trending b-axes) showing an abundance of iron-slicked surfaces which may indicate the most recent faulting event. This second conjugate set is discussed in detail below.

The subsidiary fault fabric on the straight segment before the bend and south of the fault reflects a conjugate set of oblique-slip kinematics (Fig. 23). This set does not reflect strike-slip kinematics in comparison to the kinematics of the conjugate set observed on the straight segment before the bend on the north (Fig. 23). An additional fault set in the same structural domain shows shallowly-dipping faults that are epidote-filled. The kinematics of such set are interpreted as left-lateral oblique-slip reverse faulting, similar to the shallowly dipping set within the bend segment to the north (Fig. 23). As rock approaches the bend region, the conjugate set and the shallowly dipping set are rotated clock-wise (Fig. 23). Whether or not this rotation is affected by the bend or the development of the Transfer fault is not known.

The Mill Creek fault has a double bend geometry with one bend in Mill Creek canyon and a second one at the Mill Creek Jump-Off (Figs. 3D and 7). All data around the bend was concentrated on the bend located in the Mill Creek canyon. Considering the 8.7 km of right-lateral displacement (Kendrick et al., 2015), the fabric south of the fault has already slipped through one bend and could exhibit deformation associated with such bend. The two east-west-striking right-lateral fault sets within the bend segment south of the fault, and the shallowly dipping fault set on the straight segment before the bend south of the fault may reflect movement along the straight segment and bend segment of the bend in Mill Creek Jump-Off, respectively.

Overall, the data representing the structural domains east of the bend do not exhibit characteristic strike-slip kinematics as would be expected for slip along a straight segment of a fault. Instead, there is an increase in the number of subsidiary faults that

exhibit oblique- and dip-slip kinematics within and east of the bend segment (Fig. 23). The oblique-slip kinematics seen on the straight segment after the bend north of the fault could be reflecting deformation associated to oblique compression and rapid uplift of Yucaipa Ridge.

5.3.3. Effects of Topography

The straight segment after the bend to the north of the fault displays a bimodal distribution of b-axes and slip vectors that form two conjugate sets (Fig. 23). Such relationship of conjugate sets give rise to the interpretation of two different maximum compressive stress orientations. The first conjugate set defines a stress orientation plunging 50° in the N50W direction and the second conjugate set defines a stress orientation plunging 45° in the S10E direction (Fig. 23). The stress interpretation of the first set is consistent with that of other structural domains but the second stress interpretation requires additional explanation.

One possibility is that there is significant reactivation of faults as the rock mass moves out of the bend region. This would require fault sets in the orientation observed in the bend region to be reactivated and rotated with respect to the fault trace. However, a station (Station 10) closer to the bend and within the same structural domain does not show fault sets that would resemble the orientation of those sets observed at the bend region north of the fault or those in orientation similar to the sets from which the second stress interpretation originates from.

An alternate hypothesis is that the overburden associated with the high topography of the north wall of the canyon is affecting the observed fabric. Such overburden could

impose a stress state parallel to the free surface of the canyon wall such that it would modify the orientation of the maximum compressive stress observed. Thus, the formation of conjugate sets indicating a different maximum compressive stress orientation does not reflect a change of stress on the fault surface.

5.3.4. Effects of Foliation and Outcrop Orientation

The orientation of foliation planes was recorded in the study area and is plotted for every location where data was collected (Appendix B). The foliation orientation shows variation across the study area that may be related to lithologic factors. Foliation in rock is abundant and very well organized in the foliated quartz monzonite. The foliation is organized with a dominant northeast strike and northwest dip, especially in the structural domain past the bend and to the north (Appendix B). Organized foliation surfaces are harder to identify typically south of the fault mainly where the presence of a migmatitic fabric in the orthogneisses is more abundant. At other locations (Appendix B) , foliation measurements are not sufficient to define the foliation fabric either due to a lack of foliation or a presence of contorted foliation.

With the exception of the bend region to the north of Mill Creek fault, the foliation is not seen to plot in similar orientations as dominant subsidiary fault sets. Therefore, the orientation and abundance of foliation planes does not control the distribution of fabric in the study area. This observation provides evidence to support the hypothesis that the subsidiary fault fabric across the study area is controlled by the large scale bend in the Mill Creek fault. In addition, the abundance of foliation surfaces correlates to the amount of faults whose full kinematics can be known.

Recording outcrop orientations is important for any fabric characterization because any structural feature will not be recorded if it is oriented, or very close to, parallel to the outcrop orientation (Terzaghi, 1965). Therefore, each of the poles shown represents a blind spot on the outcrop (Appendix B). This means that faults whose poles plot at the blind spot will be not sampled on the outcrop. The presence of a concentration of poles to outcrop orientations suggests that the fabric surveyed may not represent a fair sample of the faults in the rock (Terzaghi, 1965). Terzaghi (1965) advises that corrections are useful to correct for overrepresented orientations, but that it is impossible to reliably know magnitude of importance of faults near the blind spot even after a correction is applied to the data.

The foliation distribution across Mill Creek Canyon indicates that the distribution of outcrop orientations is different on either side of the Mill Creek Fault (Appendix B). The outcrop orientations north of the fault strike E-W while those south of the fault strike north-northwest. On the north side of the fault, the orientation of the Mill Creek Fault is parallel to the average outcrop orientation. It is possible that sets oriented parallel to the Mill Creek Fault, particularly those seen in synoptic diagrams for other structural domains south of the Mill Creek fault and elsewhere may not be recorded for stations north of the fault. By looking at the subsidiary fault distribution it can be argued that faults whose poles would plot at or near the blind spot are not completely devoid from sampling. Similarly, fault sets parallel to the Transfer fault are observed for the bend region to the south regardless of average outcrop orientations in parallel orientation to the Transfer fault.

The discrepancy between the reduced number of faults expected at the blind spot orientation and the presence of faults in the orientations dictated by the blind spot suggest that a correction is not needed for this data set. However, outcrop orientation may play a significant role in the long fault data because only small surfaces that are parallel to the outcrop face, and whose surfaces are slickensided, are identified.

5.4. Comparison to Other Fault Zone Studies

Numerous studies of subsidiary fault fabric exist on other major strike-slip faults of the San Andreas system from which similarities and differences aid interpretation of data presented in this study (e.g., Chester et al., 1993; Wilson et al., 2003; Almeida, 2007; Becker, 2012). These studies look at subsidiary fault orientations and kinematics on the damage zones of abandoned, exhumed faults, and have interpreted paleostress directions from the subsidiary fault fabric.

Relationships between subsidiary fault fabric orientation and location for the North Branch San Gabriel Fault (NBSGF), which has a simple, monoclinal, isolated bend, are presented by Becker (2012). The subsidiary faults fabric in the damage zone of the NBSGF show orientations and kinematics that are consistent along the straight segments of the fault and are different to those within the bend. We find that, similarly to the observations of Becker (2012), the bend region is characterized by a dominant set of sub-horizontal faults that is not seen in straight segments of the fault. This observation is limited to the north side of the fault, however, because the bend region to the south may be experiencing a significantly different state of stress due to the development of a right-

lateral, oblique-slip normal transfer zone as evidenced by the Transfer fault (Station 40/26; Fig.9).

In addition, the straight segments before and after the bend of the NBSGF exhibit a dominant fabric of sub-vertical, northwest-striking faults displaying strike-slip kinematics. A similar northwest-striking dominant fabric with strike-slip kinematics is also observed for the Mill Creek Fault in this study. The agreement between both studies reinforce the hypothesis that reactivation of faults will occur and display a preferred orientation on the rock mass once it moves through different structural domains characterized by relatively uniform stress states.

The difference is that the Mill Creek fault does not display strike-slip kinematics on sub-vertical faults on straight segments east of the bend (Fig. 23). This observation is dominant at places east of the Mill Creek Fault bend and south of the bend where the tectonic regime may have a stronger influence in the kinematics as compared to a simple, isolated bend in a strike-slip fault. This difference may indicate a component of 3D strain not observed for the NBSGF that may reflect depth of faulting where oblique tectonics is enhanced by faulting at shallower depth, and associated with tectonic complexities related to mesoscale transpression of the San Gorgonio Pass and uplift of Yucaipa Ridge.

Previous studies infer from subsidiary fault fabric the paleostress orientation of active and abandoned faults and show that the maximum compressive stress orientation was at high angles (~60° - 80°) to the main fault surface at the time of faulting (e.g., Chester et al., 1993; Wilson et al., 2003; Almeida, 2007; Becker, 2012). This interpretation holds

for the San Andreas fault at SAFOD with 315 km of displacement (e.g., Almeida, 2007), for the Punchbowl fault with 44 km of displacement (e.g., Chester et al., 1993; Wilson et al., 2003), and for the NBSGF with 16 km of displacement (e.g., Becker, 2012). In contrast, this study finds that the maximum compressive stress orientation is at a relatively low angle to the Mill Creek fault (Fig. 23). It is hypothesized that such stress orientation may reflect a higher apparent coefficient of friction on the fault surface compared to the other faults and may reflect the relatively smaller displacement magnitude of the Mill Creek fault (8.7 km) relative to the other faults.

5.5. Displacement transfer on the Mill Creek – Mission Creek stepover

The principle of mechanical efficiency is used to describe the work required by fault systems to accommodate strain (e.g., Cooke and Dair, 2011; Cooke et al., 2013; Hatem et al., 2015). Systems that are mechanically efficient have higher ratios of fault slip to off-fault deformation. Mechanically inefficient systems such as restraining bends are able to increase their efficiency through abandonment and development of fault strands (Cooke et al., 2013; Hatem et al., 2015). In analog models, this process involves the creation of new faults that transfer strike-slip and oblique-slip motion to and from principal slip surfaces.

Numerical models by Cooke and Dair (2011) of the evolution of the fault development in the San Gorgonio Pass region, indicate that the mechanical efficiency of the system increased with inception of the Mill Creek Fault at nearly 500 Kya (Fig. 4). Their model further predicts that the efficiency of the San Gorgonio Pass decreased with the abandonment of the Mill Creek Fault and introduction of the present day

configuration dominated by the Banning and Garnet Hill faults (Fig. 4). These results contradict the hypothesis provided by analog models that states mechanical efficiency should increase with progressive slip of the system and may reflect a lack of understanding of the real conditions at San Gorgonio Pass.

We observe the development of one, possibly two, major fault zones cutting across Yucaipa Ridge (Figs. 9 and 14). The kinematics associated with this structure show a complex interaction of strike- and oblique-slip motion and is interpreted as a right-lateral oblique-slip normal fault. The location of this fault zone is also coincident with the fault bend of the Mill Creek fault and may be related to the modified state of stress imposed by the geometric asperity. Accordingly, this fault zone could aid the transfer of displacement across Yucaipa Ridge to increase the mechanical efficiency of the Mill Creek-Mission Creek stepover, and eventually the San Gorgonio Pass restraining bend.

The observation of right-lateral strike-slip kinematics along the Mill Creek fault, the right-lateral oblique-slip normal kinematics of the Transfer fault in Yucaipa Ridge, and the strike-slip kinematics of the Galena Peak fault may suggest the formation of a releasing bend within Yucaipa Ridge. One hypothesis of displacement transfer is that the fault configuration is interpreted as a right-stepping segment that accommodates east-west extension in Yucaipa Ridge. The development of such structure implies that displacement from the west on the Mill Creek fault transfers through Galena Peak and the Transfer fault into the Mission Creek fault to the southeast. An example of such configuration is shown in Segall and Pollard (1980) for the Brawley and Imperial faults in Imperial Valley, also in the San Andreas system (Fig. 25).

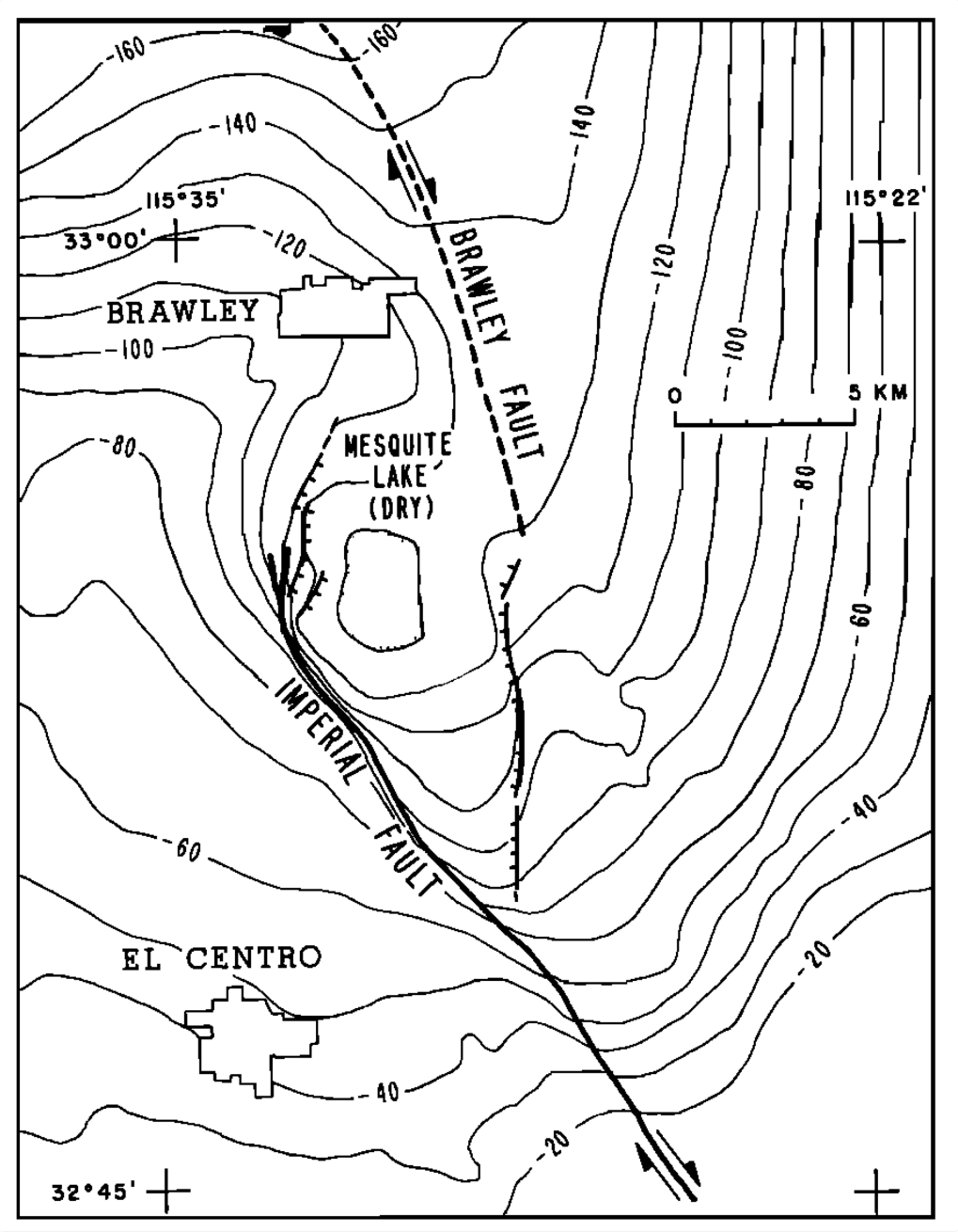

Fig. 25. Map of the Brawley and Imperial faults in Imperial Valley, southern California. The right-step between the two right-lateral faults produces a releasing bend. The northern branches of the Imperial fault and the southern extension of the Brawley fault are normal faults defining a zone of extension. Taken from Segall and Pollard (1980).

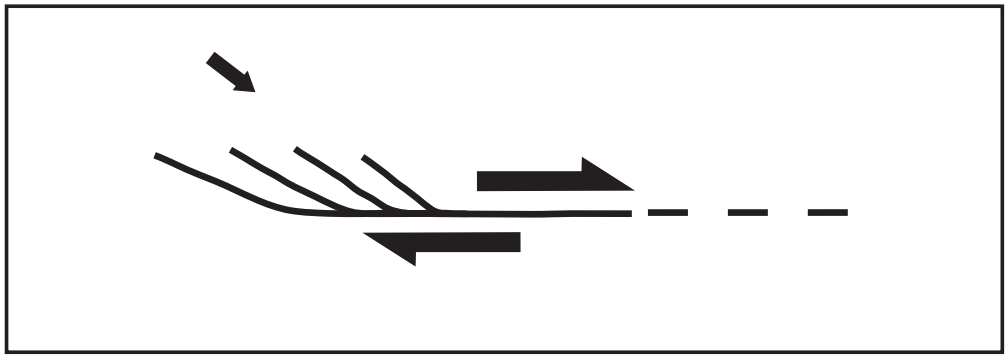

Fig. 26. Schematic diagram of a horsetail splay on a right-lateral fault. The small arrow describes the orientation of the principal maximum compressive stress. Modified from Kim and Sanderson (2006).

An alternate hypothesis of displacement transfer involves a horse-tail fault configuration between the Galena Peak and the array of Transfer faults across Yucaipa Ridge. The development of such structure implies dying of slip on the Galena Peak into the Mill Creek effectively limiting and/or preventing slip transfer from the Mission Creek to the Mill Creek fault. An example of such configuration is shown in Kim and Sanderson (2006) for a schematic depiction of a typical horse-tail geometry (Fig. 26).

5.6. Implications to Future Earthquake Rupture Modeling and Seismic Hazard

Earthquake rupture models have to account for realistic details found from direct observation in the field in order to better assess seismic hazard. One aspect of incorporating field observations into models revolves around the understanding of the slip kinematics of a fault or fault system and the relation between the surface mapping of structures to the structure at depth. The results in this study provide insight into the conditions which may be controlling active faulting in this region and which subsequently will dictate rupture propagation, or prevention, through the Mill Creek-Mission Creek stepover.

The observation and interpretations of the subsidiary fault fabric in the straight and bend segments of the Mill Creek fault provides guidance for understanding slip kinematics of the Mill Creek-Mission Creek stepover. Incorporation of 1) the slip kinematics observed through the fault bend in Mill Creek canyon, 2) the geometry of the Mill Creek fault, 3) the stress orientations along the fault trace, 4) the slip transfer occurring in Yucaipa Ridge, and 5) the damage intensity observed within the fault zone structure, could greatly improve the predicting capabilities of such models. Further, the

interpretation of higher apparent friction on the Mill Creek fault and the possible link to fault displacement magnitude would suggest that a rupture propagating north from Salton Trough would possibly bypass the Mill Creek fault in favor of a fault with higher displacement magnitude like the Mission Creek fault.

Additionally, numerical-mechanical models of faults with bends predict that an increased amount of plastic strain is localized on the extensional quadrant of a fault with a bend (e.g., Duan and Day, 2008). This is compatible with our observation of a mesoscale transfer fault south of the bend in Mill Creek Canyon. This fault, and those in similar orientations like the Galena Peak fault, could play a critical role in the system by transferring slip onto active strands of the stepover.

6. SUMMARY AND CONCLUSIONS

The subsidiary fault fabric of the damage zone of the Mill Creek fault indicates that the trend of the maximum principal compressive stress is oriented at a relatively low angle (~45˚) to the fault trace, which contrasts with the large angles (60-80˚) documented for other faults of the San Andreas system (e.g., San Gabriel fault, Punchbowl fault, and the San Andreas fault at SAFOD). The different principal stress orientation may indicate that the Mill Creek fault operated at a higher apparent friction than the other faults, and may reflect the relatively smaller displacement magnitude of the Mill Creek fault (>8 km) relative to the other faults.

The complexity in subsidiary fault fabric and prevalence of oblique-slip faulting increases from the northwest straight segment of the Mill Creek fault into the bend region, and the plunge of the inferred direction of the maximum principal compressive stress axis steepens from nearly horizontal to approximately plunging 45˚ towards the northwest. These observations imply a more significant component of three-dimensional deformation in the Mill Creek canyon region compared to that in a similar-shaped fault-bend along the North Branch San Gabriel fault. The difference may reflect depth of faulting where oblique tectonics is enhanced by faulting at shallower depth, and more interaction with neighboring faults in the Mill Creek region as compared to the San Gabriel fault area.

Three deformation events are identified in the study on the basis of subsidiary fault fabrics, location within the study area, and cross-cutting relationships. The earlier, dominant deformation event is fault-damage development associated with movement

along the Mill Creek fault from the straight segments into the bend region. A younger event in the region south of the Mill Creek fault bend is the development of the right-lateral oblique-normal transfer faults, which is recorded by the overprinting of epidote-mineralized subsidiary faults by younger iron-oxide stained faults associated with the formation of transfer faults and movement along these faults. The youngest deformation event consists of fracturing and reactivation of subsidiary faults on the north canyon walls, east of the bend in the Mill Creek fault, that likely records shortening associated with the steep topography and mass wasting processes during rapid uplift and exhumation.

The displacements on the right-lateral oblique-normal transfer faults, south of the fault bend, achieve east-west extension and right-lateral shear between the Mill Creek fault to the north and the Galena Peak fault to the south. These younger faults likely contributed to the overall right-lateral shear along the Mill Creek-Mission Creek-Galena Peak fault system through the San Gorgonio Pass region by transferring displacement from the northwest segment of the Mill Creek fault to the southeast segment of the Mission Creek fault, effectively bypassing the bend and Raywood Flat regions of the Mill Creek fault. The transfer faults also could constitute a pull-apart horsetail fault system (e.g., Kim and Sanderson, 2006) that diffuses slip on the Galena Peak fault without transfer of right-lateral displacement onto the Mill Creek fault, particularly for slip events propagating to the northwest on the Mission Creek fault and into the San Gorgonio Pass region. The mechanics of formation of the transfer faults may be understood in the context of a releasing step-over (e.g., Segall and Pollard, 1980).

The geometry of the transfer faults relative to the Mill Creek and Galena Peak faults is similar to other extensional step-over and bends of the southern San Andreas System (e.g., Segall and Pollard, 1980), and maybe be analogous to faulting at a larger scale associated with transfer from the Mission Creek fault to the San Bernardino strand of the San Andreas fault southwest of the study area.

REFERENCES

Acharya, H.K., 1997. Influence of fault bends on ruptures. Bull. Seismol. Soc. Am. 87, 1691–1696.

Allen, C.R., 1957. San Andreas Fault Zone in San Gorgonio Pass, Southern Califronia. America (NY). 68, 315–350. doi:10.1130/0016-7606(1957)68

Almeida, R., 2007. Mesoscale Fracture Fabric and Paleostress Along the San Andreas Fault at SAFOD. Texas A&M University.

Anders, M.H., Wiltschko, D. V., 1994. Microfracturing, paleostress and the growth of faults. J. Struct. Geol. 16, 795–815. doi:10.1016/0191-8141(94)90146-5

Anderson, E.M., 1951. The dynamics of faulting and dyke formation with applications to Britain, 2nd ed. Oliver and Boyd, Edinburgh.

Andrews, D.J., 2005. Rupture dynamics with energy loss outside the slip zone. J. Geophys. Res. 110, B01307. doi:10.1029/2004JB003191

Aydin, A., Nur, A., 1985. Types and role of stepovers in strike-slip tectonics. Soc. Econ. Paleontol. Mineral. Spec. Publ. 37, 35–44.

Barka, A., Kadinsky-Cade, K., 1988. Strike-slip fault geometry in Turkey. Tectonics. doi:10.1029/TC007i003p00663

Bartholomew, T.D., Little, T. a, Clark, K.J., Van Dissen, R., Barnes, P.M., 2014. Kinematics and paleoseismology of the Vernon Fault, Marlborough Fault System, New Zealand: Implications for contractional fault bend deformation, earthquake triggering, and the record of Hikurangi subduction earthquakes. Tectonics 33,

1201–1218. doi:10.1002/2014TC003543

Becker, A.W., 2012. Off-fault damage associated with a localized bend in the north branch san gabriel fault, California. Texas A&M University.

Ben-Zion, Y., Shi, Z., 2005. Dynamic rupture on a material interface with spontaneous generation of plastic strain in the bulk. Earth Planet. Sci. Lett. 236, 486–496. doi:10.1016/j.epsl.2005.03.025

Berg, S.S., Skar, T., 2005. Controls on damage zone asymmetry of a normal fault zone: Outcrop analyses of a segment of the Moab fault, SE Utah. J. Struct. Geol. 27, 1803–1822. doi:10.1016/j.jsg.2005.04.012

Bistacchi, A., Massironi, M., Menegon, L., 2010. Three-dimensional characterization of a crustal-scale fault zone: The Pusteria and Sprechenstein fault system (Eastern Alps). J. Struct. Geol. 32, 2022–2041. doi:10.1016/j.jsg.2010.06.003

Caine, J.S., Evans, J.P., Forster, C.B., 1996. Fault zone architechture and permeability structure. Geology 24, 1025–1028. doi:10.1130/0091-7613(1996)024<1025

Cardozo, N., Allmendinger, R.W., 2013. Spherical projections with OSXStereonet. Comput. Geosci. 51, 193–205. doi:10.1016/j.cageo.2012.07.021

Carena, S., Suppe, J., Kao, H., 2004. Lack of continuity of the San Andreas Fault in southern California: Three-dimensional fault models and earthquake scenarios. J. Geophys. Res. B Solid Earth 109. doi:10.1029/2003JB002643

Chester, F.M., Chester, J.S., 1998. Ultracataclasite structure and friction processes of the Punchbowl fault, San Andreas system, California. Tectonophysics 295, 199–221.

Chester, F.M., Chester, J.S., 2000. Stress and deformation along wavy frictional faults. J. Geophys. Res. 105, 23,421-23,430. doi:10.1029/2000JB900241

Chester, F.M., Chester, J.S., Kirschner, D.L., Schulz, S.E., Evans, J.P., 2004. Structure of large-displacement, strike-slip fault zones in the brittle continental crust, in: Karner, G.D., Taylor, B., Driscoll, N.W., Kohlstedt, D.. (Eds.), Rheology and Deformation of the Lithosphere at Continental Margins. Columbia Univerisity Press, New York, pp. 223–260.

Chester, F.M., Evans, J.P., Biegel, R.L., 1993. Internal Structure and Weakening Mechanisms of the San Andreas Fault. J. Geophys. Res. 98, 771–786.

Chester, F.M., Logan, J.M., 1986. Implications for Mechanical Properties of Brittle Faults from Observations of the Punchbowl Fault Zone, California. Pure Appl. Geophys. 124, 79–106.

Chester, J.S., Chester, F.M., Kronenberg, A.K., 2005. Fracture surface energy of the Punchbowl fault, San Andreas system. Nature 437, 133–136. doi:10.1038/nature03942

Chester, J.S., Fletcher, R.C., 1997. Stress distribution and failure in anisotropic rock near a bend on a weak fault. J. Geophys. Res. 102, 693–708. doi:10.1029/96JB02791

Choi, J.H., Edwards, P., Ko, K., Kim, Y.S., 2016. Definition and classification of fault damage zones: A review and a new methodological approach. Earth-Science Rev. 152, 70–87. doi:10.1016/j.earscirev.2015.11.006

Christie-Blick, N., Biddle, K.T., 1985. Deformation and basin formation algon strike-

slip faults. Soc. Econ. Paleontol. Mineral. Spec. Publicait. 37, 1–34.

Cooke, M.L., Dair, L.C., 2011. Simulating the recent evolution of the southern big bend of the San Andreas fault, Southern California. J. Geophys. Res. 116, B04405. doi:10.1029/2010JB007835

Cooke, M.L., Schottenfeld, M.T., Buchanan, S.W., 2013. Evolution of fault efficiency at restraining bends within wet kaolin analog experiments. J. Struct. Geol. 51, 180–192. doi:10.1016/j.jsg.2013.01.010

Cowgill, E., Arrowsmith, J.R., Yin, A., Wang, X., Chen, Z., 2004. The Akato Tagh bend along the Altyn Tagh fault, northwest Tibet 2: Active deformation and the importance of transpression and strain hardening within the Altyn Tagh system. Bull. Geol. Soc. Am. 116, 1443–1464. doi:10.1130/B25360.1

Cowie, P. a., Scholz, C.H., 1992. Growth of faults by accumulation of seismic slip. J. Geophys. Res. 97, 11085. doi:10.1029/92JB00586

Crowell, J.C., 1974. Origin of Late Cenozoic Basins in southern California. Soc. Econ. Paleontol. Mineral. Spec. Publ. 22, 190–204.

Crowell, J.C., 1979. The San Andreas fault system through time. J. Geol. Soc. London 136, 293–302.

Dair, L., Cooke, M.L., 2009. San Andreas fault geometry through the San Gorgonio Pass, California. Geology 37, 119–122. doi:10.1130/G25101A.1

Dedontney, N., Templeton-Barrett, E.L., Rice, J.R., Dmowska, R., 2011. Influence of plastic deformation on bimaterial fault rupture directivity. J. Geophys. Res. Solid

Earth 116, 1–12. doi:10.1029/2011JB008417

Dibblee Jr., T.W., 1964. Geologic map of the San Gorgonio Mountain quadrangle, San Bernardino and Riverside Counties, California. U. S. Geol. Surv. Misc. Geol. Investig. I-431, 1:62,500.

Dibblee Jr., T.W., 1967. Geologic Map of the Morongo Valley Quadrangle, San Bernardino and Riverside Counties, California. U.S. Geol. Surv. Misc. Geol. Investig. I-517, 1:62,500.

Dibblee Jr., T.W., 1968. Evidence of major lateral displacement on the Pinto Mountain fault, southern California. Geol. Soc. Am. Spec. Pap. 115, 322.

Dibblee Jr., T.W., 1970. Regional Geologic Map of San Andreas and Related Faults in Eastern San Gabriel Mountains, San Bernardino Mountains, Western San Jacinto Mountains and Vicinity, U.S. Geological Survey Open-File Report 71-88, 1:125,000. U.S. Geological Survey Open-File Report 71-88, 1:125,000.

Dibblee Jr., T.W., 1982. Geology of the San Bernardino Mountains, southern California, in: Geology and Mineral Wealth of the California Transverse Ranges: South Coast Geological Society Guidebook No. 10. pp. 148–169.

Dor, O., Rockwell, T.K., Ben-Zion, Y., 2006. Geological observations of damage asymmetry in the structure of the San Jacinto, San Andreas and Punchbowl faults in Southern California: A possible indicator for preferred rupture propagation direction. Pure Appl. Geophys. 163, 301–349. doi:10.1007/s00024-005-0023-9

Duan, B., Day, S.M., 2008. Inelastic strain distribution and seismic radiation from

rupture of a fault kink. J. Geophys. Res. Solid Earth 113, 1–19. doi:10.1029/2008JB005847

Duan, B., Oglesby, D.D., 2005. Multicycle dynamics of nonplanar strike-slip faults. J. Geophys. Res. B Solid Earth 110, 1–16. doi:10.1029/2004JB003298

Duan, B., Oglesby, D.D., 2006. Heterogeneous fault stresses from previous earthquakes and the effect on dynamics of Parallel strike-slip faults. J. Geophys. Res. Solid Earth 111, 15. doi:10.1029/2005JB004138

Dunham, E.M., Belanger, D., Cong, L., Kozdon, J.E., 2011. Earthquake ruptures with strongly rate-weakening friction and off-fault plasticity, part 2: Nonplanar faults. Bull. Seismol. Soc. Am. 101, 2308–2322. doi:10.1785/0120100076

Fialko, Y., 2006. Interseismic strain accumulation and the earthquake potential on the southern San Andreas fault system. Nature 441, 968–971. doi:10.1038/nature04797

Finzi, Y., Langer, S., 2012. Damage in step-overs may enable large cascading earthquakes. Geophys. Res. Lett. 39, L16303. doi:10.1029/2012GL052436

Fletcher, J.M., Teran, O.J., Rockwell, T.K., Oskin, M.E., Hudnut, K.W., Mueller, K.J., Spelz, R.M., Akciz, S.O., Masana, E., Faneros, G., Fielding, E.J., Leprince, S., Morelan, A.E., Stock, J., Lynch, D.K., Elliott, A.J., Gold, P., Liu-Zeng, J., González-Ortega, A., Hinojosa-Corona, A., González-García, J., 2014. Assembly of a large earthquake from a complex fault system: Surface rupture kinematics of the 4 April 2010 El Mayor-Cucapah (Mexico) Mw 7.2 earthquake. Geosphere 10, 797–827. doi:10.1130/GES00933.1

Gibson, R.C., 1971. Nonmarine turbidites and the San Andreas Fault, San Bernardino Mountains, in: Elders, W.A. (Ed.), Geological Excursions in Southern California. University of California Campus Museum Contributions, Riverside, pp. 167–181.

Goebel, T.H.W., Hauksson, E., Shearer, P.M., Ampuero, J.P., 2015. Stress-drop heterogeneity within tectonically complex regions: a case study of San Gorgonio Pass, southern California. Geophys. J. Int. 202, 514–528. doi:10.1093/gji/ggv160

Gold, P.O., Behr, W.M., Rood, D., Sharp, W.D., Rockwell, T.K., Kendrick, K., Salin, A., 2015. Holocene geologic slip rate for the Banning strand of the southern San Andreas Fault, southern California. J. Geophys. Res. Solid Earth 120, 5639–5663. doi:10.1002/2015JB012004

Graves, R., Jordan, T.H., Callaghan, S., Deelman, E., Field, E., Juve, G., Kesselman, C., Maechling, P., Mehta, G., Milner, K., Okaya, D., Small, P., Vahi, K., 2011. CyberShake: A Physics-Based Seismic Hazard Model for Southern California. Pure Appl. Geophys. 168, 367–381. doi:10.1007/s00024-010-0161-6

Graves, R.W., Aagaard, B.T., Hudnut, K.W., Star, L.M., Stewart, J.P., Jordan, T.H., 2008. Broadband simulations for Mw 7.8 southern san andreas earthquakes: Ground motion sensitivity to rupture speed. Geophys. Res. Lett. 35, 1–5. doi:10.1029/2008GL035750

Griffith, W.A., Nielsen, S., Di Toro, G., Smith, S. a F., 2010. Rough faults, distributed weakening, and off-fault deformation. J. Geophys. Res. Solid Earth 115, 22. doi:10.1029/2009JB006925

Hatem, A.E., Cooke, M.L., Madden, E.H., 2015. Evolving efficiency of restraining bends within wet kaolin analog experiments. J. Geophys. Res. Solid Earth 120, 1975–1992. doi:10.1002/2014JB011735

Hill, R.T., 1928. Southern California geology and Los Angeles earthquakes. The Southern California Academy of Sciences, Los Angeles, California.

Huang, Y., Ampuero, J.-P., Helmberger, D. V., 2014. Earthquake ruptures modulated by waves in damaged fault zones. J. Geophys. Res. Solid Earth 119, 3133–3154. doi:10.1002/2013JB010724

Huang, Y., Ampuero, J.P., Helmberger, D. V., 2016. The potential for supershear earthquakes in damaged fault zones - theory and observations. Earth Planet. Sci. Lett. 433, 109–115. doi:10.1016/j.epsl.2015.10.046

Jones, B.L.M., Bernknopf, R., Cox, D., Goltz, J., Hudnut, K., Perry, S., Ponti, D., Porter, K., Reichle, M., Seligson, H., Shoaf, K., Treiman, J., Wein, A., 2008. The ShakeOut Scenario, USGS Open File Report 2008-1150.

Jones, L.M., 1988. Focal Mechanisms and the State of Stress on the San Andreas Fault in Southern California. J. Geophys. Res. 93, 8869–8891.

Kato, N., Satoh, T., Lei, X., Yamamoto, K., Hirasawa, T., 1999. Effect of fault bend on the rupture propagation process of stick-slip. Tectonophysics 310, 81–99. doi:10.1016/S0040-1951(99)00149-3

Kendrick, K.J., Matti, J.C., Mahan, S.A., 2015. Late Quaternary slip history of the Mill Creek strand of the San Andreas fault in San Gorgonio Pass, southern California:

The role of a subsidiary left-lateral fault in strand switching. Geol. Soc. Am. Bull. B31101.1, 1–25. doi:10.1130/B31101.1

Kim, Y.-S., Sanderson, D.J., 2006. Structural similarity and variety at the tips in a wide range of strike-slip faults: A review. Terra Nov. 18, 330–344. doi:10.1111/j.1365-3121.2006.00697.x

King, G., Nabelek, J., 1985. Role of fault bends in the initiation and termination of earthquake rupture. Science 228, 984–987. doi:10.1126/science.228.4702.984

Langenheim, V.E., Jachens, R.C., Matti, J.C., Hauksson, E., Morton, D.M., Christensen, A., 2005. Geophysical evidence for wedging in the San Gorgonio Pass structural knot, southern San Andreas fault zone, southern California. Geol. Soc. Am. Bull. 117, 1554–1572. doi:10.1130/B25760.1

Little, T.A., 1995. Brittle deformation adjacent to the Awatere strike-slip fault in New Zealand: Faulting patterns, scaling relationships, and displacement partitioning. Geol. Soc. Am. Bull. 107, 1255–1271. doi:10.1130/0016-7606(1995)107<1255

Lozos, J.C., Oglesby, D.D., Brune, J.N., Olsen, K.B., 2012. Small intermediate fault segments can either aid or hinder rupture propagation at stepovers. Geophys. Res. Lett. 39, 4. doi:10.1029/2012GL053005

Lozos, J.C., Oglesby, D.D., Duan, B., Wesnousky, S.G., 2011. The effects of double fault bends on rupture propagation: A geometrical parameter study. Bull. Seismol. Soc. Am. 101, 385–398. doi:10.1785/0120100029

Lyakhovsky, V., Ben-Zion, Y., Agnon, A., 1997. Distributed damage, faulting, and

friction. J. Geophys. Res. 102, 27635. doi:10.1029/97JB01896

Ma, S., Andrews, D.J., 2010. Inelastic off-fault response and three-dimensional dynamics of earthquake rupture on a strike-slip fault. J. Geophys. Res. 115, 1–16. doi:10.1029/2009JB006382

Magistrale, H., Sanders, C., 1996. Evidence from precise earthquake hypocenters for segmentation of the San Andreas Fault in San Gorgonio Pass. J. Geophys. Res. 101, 3031–3044. doi:10.1029/95JB03447

Mann, P., 2007. Global catalogue, classification and tectonic origins of restraining- and releasing bends on active and ancient strike-slip fault systems. Geol. Soc. London, Spec. Publ. 290, 13–142. doi:10.1144/SP290.2

Mann, P., Demets, C., Wiggins-Grandison, M., 2007. Toward a better understanding of the Late Neogene strike-slip restraining bend in Jamaica: geodetic, geological, and seismic constraints. Geol. Soc. London, Spec. Publ. 290, 239–253. doi:10.1144/SP290.8

Matti, J.C., Cox, B.F., Iverson, S.R., 1983. Mineral resource potential map of the Raywood Flat roadless areas, Riverside and San Bernardino counties, California, U.S. Geological Survey Miscellaneous Field Studies Map 1563-A.

Matti, J.C., Morton, D.M., 1993. Paleogeographic evolution of the San Andreas fault in southern California: A reconstruction based on a new cross-fault correlation, in: Powell, R.E., Weldon, R.J., I., Matti, J.C. (Eds.), The San Andreas Fault System: Displacement, Palinspastic Reconstruction, and Geologic Evolution. Geological

Society of America Memoir 178, Boulder, Colorado, pp. 107–159.

Matti, J.C., Morton, D.M., Cox, B.F., 1992a. The San Andreas Fault System in the Vicinity of the Central Transverse Ranges Provice, southern California, U.S. Geological Survey Open-File Report 92-354.

Matti, J.C., Morton, D.M., Cox, B.F., 1992b. Distribution and Geologic Relations of Fault Systems in the Vicinity of the Central Transverse Ranges, Southern California, U.S. Geological Survey Open-File Report 92-354, 1:250,000. USGS Open-File Report 92-354.

Matti, J.C., Morton, D.M., Cox, B.F., Carson, S.E., Yetter, T.J., 1992c. Geologic Setting of The Yucaipa Quadrangle, San Bernardino and Riverside Counties, California, U.S. Geological Survey Open-File Report 92-446.

Matti, J.C., Morton, D.M., Cox, B.F., Carson, S.E., Yetter, T.J., 2003. Geologic Map and digital database of the Yucaipa 7.5' Quadrangle, San Bernardino and Riverside Counties, California, U.S. Geological Survey Open-File Report 03-301.

McClay, K., Bonora, M., 2001. Analog models of restrining stepovers in strike-slip fault systems. Am. Assoc. Pet. Geol. Bull. 85, 233–260. doi:10.1306/8626C7AD-173B-11D7-8645000102C1865D

McGill, S.F., Birnbaum, B.B., Burke, D., Reeder, T., 1999. Late Quaternary Activity on the North Branch of the San Andreas fault near San Bernardino, California, in: Water for Southern California. San Diego Association of Geologists, pp. 31–36.

McGill, S.F., Spinler, J.C., McGill, J.D., Bennett, R.A., Floyd, M.A., Fryxell, J.E.,

Funning, G.J., 2015. Kinematic modeling of fault slip rates using new geodetic velocities from a transect across the Pacific-North America plate boundary through the San Bernardino Mountains, California. J. Geophys. Res. Solid Earth 120, 2772–2793. doi:10.1002/2014JB011459.Received

Mitchell, T.M., Faulkner, D.R., 2009. The nature and origin of off-fault damage surrounding strike-slip fault zones with a wide range of displacements: A field study from the Atacama fault system, northern Chile. J. Struct. Geol. 31, 802–816. doi:10.1016/j.jsg.2009.05.002

Mitra, S., Paul, D., 2011. Structural geometry and evolution of releasing and restraining bends: Insights from laser-scanned experimental models. Am. Assoc. Pet. Geol. Bull. 95, 1147–1180. doi:10.1306/09271010060

Nicholson, C., Seeber, L., Williams, P., Sykes, L.R., 1986. Seismicity and fault kinematics through the Eastern Transverse Ranges, California: Block rotation, strike-slip faulting and low-angle thrusts. J. Geophys. Res. 91, 4891. doi:10.1029/JB091iB05p04891

Norris, R.J., Cooper, A.F., 2001. Late Quaternary slip rates and slip partitioning on the Alpine Fault, New Zealand. J. Struct. Geol. 23, 507–520. doi:10.1016/S0191-8141(00)00122-X

Olsen, K.B., Day, S.M., Minster, J.B., Cui, Y., Chourasia, A., Faerman, M., Moore, R., Maechling, P., Jordan, T., 2006. Strong shaking in Los Angeles expected from southern San Andreas earthquake. Geophys. Res. Lett. 33, L07305.

doi:10.1029/2005GL025472

Peltzer, G., Crampé, F., Rosen, P., 2001. The Mw 7.1, Hector Mine, California earthquake: surface rupture, surface displacement field, and fault slip solution from ERS SAR data. Earth Planet. Sci. 333, 545–555. doi:10.1016/S1251-8050(01)01658-5

Petersen, M.D., Wesnousky, S.G., 1994. Fault Slip Rates and Earthquake Histories for Active Faults in Southern California. October 84, 1608–1649.

Power, W.L., Tullis, T.E., 1991. Euclidean and fractal models for the description of rock surface roughness. J. Geophys. Res. 96, 415. doi:10.1029/90JB02107

Power, W.L., Tullis, T.E., Brown, S.R., Boitnott, G.N., Scholz, C.H., 1987. Roughness of natural fault surfaces. Geophys. Res. Lett. 14, 29. doi:10.1029/GL014i001p00029

Rasmussen, G., Reeder, W., 1986. What happens to the real San Andreas fault at Cottonwood canyon, Sangorgonio pass, California?, in: Kooser, M.A., Reynolds, R.E. (Eds.), Geology Arround the Margins of the Eastern San Bernardino Mountains. Inland Geological Society, Redlands, California, pp. 157–162.

Roten, D., Olsen, K.B., Day, S.M., Cui, Y., Fäh, D., 2014. Expected seismic shaking in Los Angeles reduced by San Andreas fault zone plasticity. Geophys. Res. Lett. 41, 2769–2777. doi:10.1002/2014GL059411

Sagy, A., Brodsky, E.E., 2009. Geometric and rheological asperities in an exposed fault zone. J. Geophys. Res. 114, 1–15. doi:10.1029/2008JB005701

Saucier, F., Humphreys, E., Weldon II, R., 1992. Stress Near Geometrically Complex Strike-Slip Faults : Application to the San Andreas Fault at Cajon Pass, Southern California. J. Geophys. Res. 97, 5081–5094.

Savage, H.M., Brodsky, E.E., 2011. Collateral damage: Evolution with displacement of fracture distribution and secondary fault strands in fault damage zones. J. Geophys. Res. 116, B03405. doi:10.1029/2010JB007665

Seeber, L., Armbruster, J.G., 1995. The San Andreas Fault system through the Transverse Ranges as illuminated by earthquakes. J. Geophys. Res. 100, 8285–8310. doi:10.1029/94JB02939

Segall, P., Pollard, D.D., 1980. Mechanics of Discontinuous Faults. J. Geophys. Res. 85, 4337–4350.

Shamir, G., Zoback, M.D., Barton, C.A., 1988. In situ Stress Orientation near the San Andreas fault: Preliminary results to 2.1 km Depth from the Cajon Pass scientific drillhole. Geophys. Res. Lett. 15, 989–992.

Sibson, R.H., 1986. Brecciation processes in fault zones: Inferences from earthquake rupturing. Pure Appl. Geophys. PAGEOPH 124, 159–175. doi:10.1007/BF00875724

Smith, S.A.F., Bistacchi, A., Mitchell, T.M., Mittempergher, S., Di Toro, G., 2013. The structure of an exhumed intraplate seismogenic fault in crystalline basement. Tectonophysics 599, 29–44. doi:10.1016/j.tecto.2013.03.031

Spinler, J.C., Bennett, R. a., Anderson, M.L., McGill, S.F., Hreinsdóttir, S., McCallister,

A., 2010. Present-day strain accumulation and slip rates associated with southern San Andreas and eastern California shear zone faults. J. Geophys. Res. 115, 29. doi:10.1029/2010JB007424

Spotila, J.A., Farley, K.A., Yule, J.D., Reiners, P.W., 2001. Near-field transpressive deformation along the San Andreas faul zone in southern California, based on exhumation constrained by (U-Th)/He dating. J. Geophys. Res. 106, 30909–30922.

Spotila, J.A., Sieh, K., 2000. Architecture of transpressional thrust faulting in the San Bernadino mountains, Southern California, from deformation of a deeply weathered surface. Tectonics 19, 589–615. doi:10.1029/1999TC001150

Sylvester, A.G., 1988. Strike-slip faults. Geol. Soc. Am. Bull. 1–38. doi:10.1130/0016-7606(1988)100<1666

Templeton, E.L., Rice, J.R., 2008. Off-fault plasticity and earthquake rupture dynamics: 1. Dry materials or neglect of fluid pressure changes. J. Geophys. Res. Solid Earth 113, 1–19. doi:10.1029/2007JB005529

Terzaghi, R.D., 1965. Sources of error in Joint Surveys. Geotechnique 15, 287–304.

Vermilye, J.M., Scholz, C.H., 1998. The process zone: A microstructural view of fault growth. J. Geophys. Res. 103, 12,223-12,237.

Wakabayashi, J., Hengesh, J. V., Sawyer, T.L., 2004. Four-dimensional transform fault processes: Progressive evolution of step-overs and bends. Tectonophysics 392, 279–301. doi:10.1016/j.tecto.2004.04.013

Wald, D.J., Heaton, T.H., 1994. Spatial and Temporal Distribution of Slip for the 1992

Landers , California , Earthquake. Bull. Seismol. Soc. Am. 84, 668–691.

Wallace, R.E., Morris, H.T., 1986. Characteristics of faults and shear zones in deep mines. Pure Appl. Geophys. PAGEOPH 124, 107–125. doi:10.1007/BF00875721

Weldon, R.J., Fumal, T.E., Biasi, G.P., Scharer, K.M., 2005. Past and future earthquakes on the San Andreas Fault. Science 308, 966–7. doi:10.1126/science.1111707

Wesnousky, S.G., 2008. Displacement and geometrical characteristics of earthquake surface ruptures: Issues and implications for seismic-hazard analysis and the process of earthquake rupture. Bull. Seismol. Soc. Am. 98, 1609–1632. doi:10.1785/0120070111

Wilson, J.E., Chester, J.S., Chester, F.M., 2003. Microfracture analysis of fault growth and wear processes, Punchbowl Fault, San Andreas system, California. J. Struct. Geol. 25, 1855–1873. doi:10.1016/S0191-8141(03)00036-1

Xing, H.L., Mora, P., Makinouchi, a., 2004. Finite element analysis of fault bend influence on stick-slip instability along an intra-plate fault. Pure Appl. Geophys. 161, 2091–2102. doi:10.1007/s00024-004-2550-1

Yule, D., 2009. The enigmatic San Gorgonio Pass. Geology 37, 191–192. doi:10.1130/focus022009.1

Yule, D., Sieh, K., 2003. Complexities of the San Andreas fault near San Gorgonio Pass: Implications for large earthquakes. J. Geophys. Res. 108, 2548. doi:10.1029/2001JB000451

Yule, J.D., Sieh, K.E., 2001. The paleoseismic record at Burro Flats: evidence for a 300-

year average recurrence for large earthquakes on the San Andreas Fault in San Gorgonio Pass, southern California. Geol. Soc. Am. Abstr. with Programs 33, pg. 31.

Zeng, Y., Shen, Z.K., 2014. Fault network modeling of crustal deformation in California constrained using GPS and geologic observations. Tectonophysics 612–613, 1–17. doi:10.1016/j.tecto.2013.11.030

Zoback, M.D., Zoback, M. Lou, Mount, V.S., Suppe, J., Eaton, J.P., Healy, J.H., Oppenheimer, D., Reasenberg, P., Jones, L., Raleigh, C.B., Ivan, G., Scotti, O., Wentworth, C., 1987. New Evidence on the San Andreas State Fault of Stress System of the. Science 238, 1105–1111.

APPENDIX A

FIGURES

SB0-8 All Faults

a. Fault Normals
n = 32

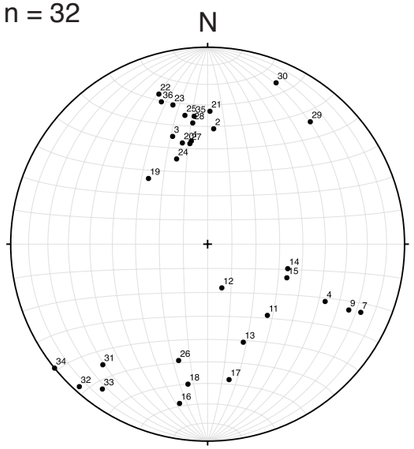

b. Fault Slip Vectors
n = 21

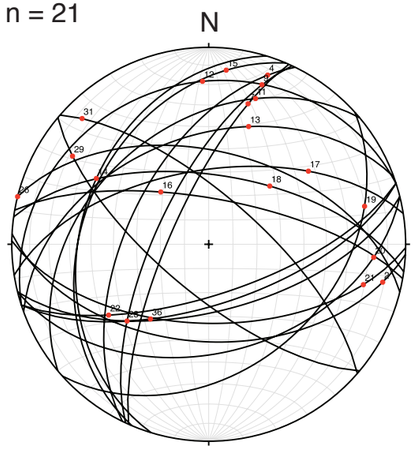

e. Gouge and Breccia Fault Normals
n = 11

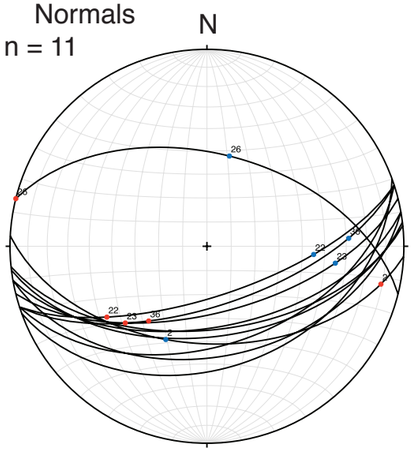

f. Fe Faults and Slickenlines
n = 1

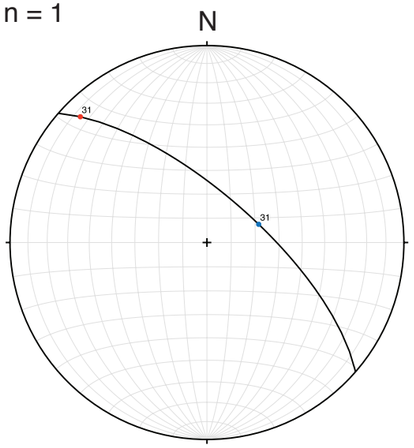

c. Fault B-Axes
n = 23

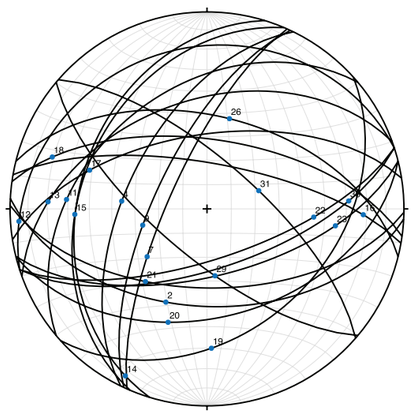

d. Faults, Large
n = 9

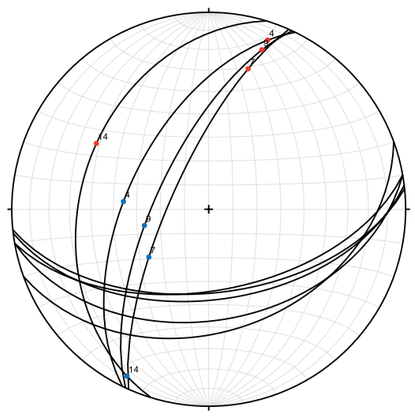

g. Epidote and Fe Faults and Slickenlines
n = xx

N

N/A

h. Epidote Faults and Slickenlines
n = xx

N

N/A

Kamb Contours, C.I. = 2 Sigma Symbols: • Slickenlines • B-axes

A-1. SB0-8 subsidiary fault data diagrams. The diagrams include: a) Fault poles; b) Slip vectors; c) B-axes; d) Long faults; e) Gouge and breccia zones; f) Iron-stained and/or iron-slickensided faults; g) Epidote-filled faults overprinted by iron-staining; h) Epidote-filled and/or Epidote-slickensided faults.

SB1N - All Faults

a. Fault Normals
n = 100

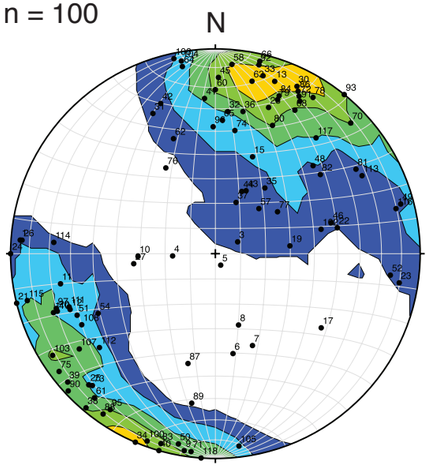

b. Fault Slip Vectors
n = 72

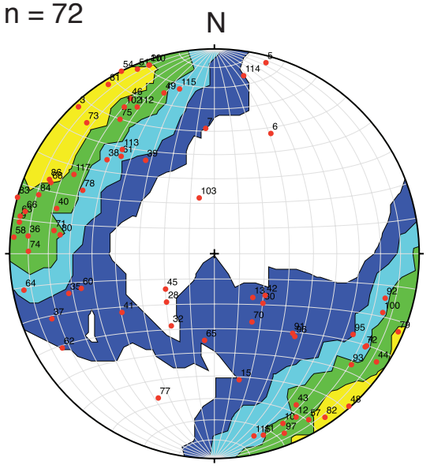

e. Gouge and Breccia Fault Normals
n = 8

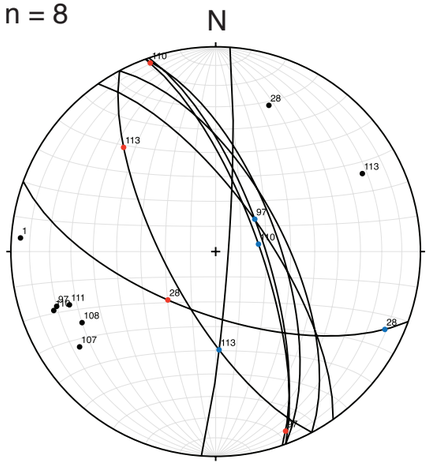

f. Fe Faults and Slickenlines
n = 26

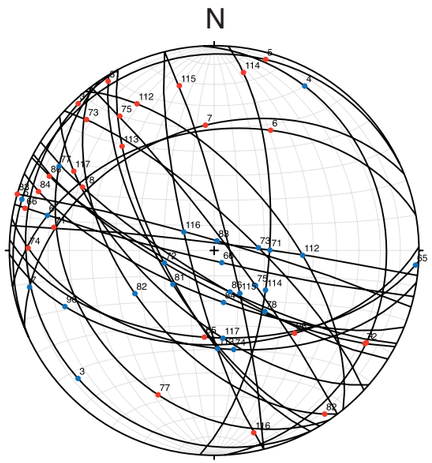

c. Fault B-Axes
n = 72

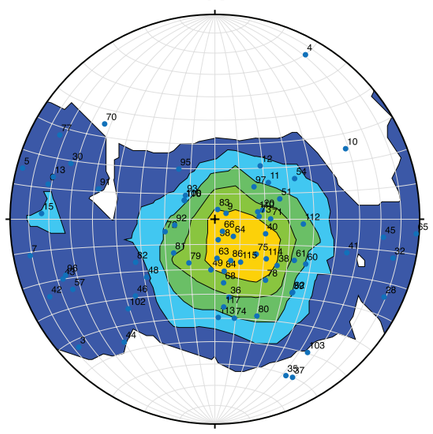

d. Faults, Large
n = 16

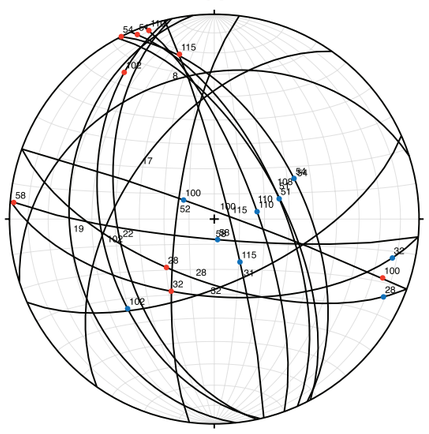

g. Epidote and Fe Faults and Slickenlines
n = xx

N

N/A

h. Epidote Faults and Slickenlines
n = xx

N

N/A

Kamb Contours, C.I. = 2 Sigma Symbols: • Slickenlines • B-axes

A-2. SB1N subsidiary fault data diagrams. The diagrams include: a) Fault poles; b) Slip vectors; c) B-axes; d) Long faults; e) Gouge and breccia zones; f) Iron-stained and/or iron-slickensided faults; g) Epidote-filled faults overprinted by iron-staining; h) Epidote-filled and/or Epidote-slickensided faults.

SB1W - All Faults

a. Fault Normals
n = 21

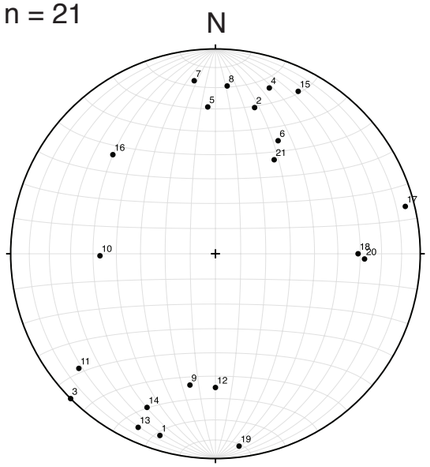

b. Fault Slip Vectors
n = 21

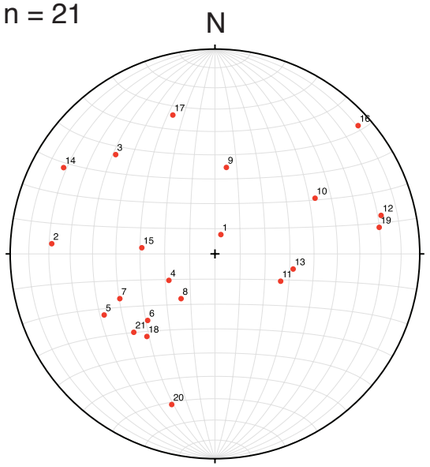

e. Gouge and Breccia Fault Normals
n = xx

N

N/A

f. Fe Faults and Slickenlines
n = 2

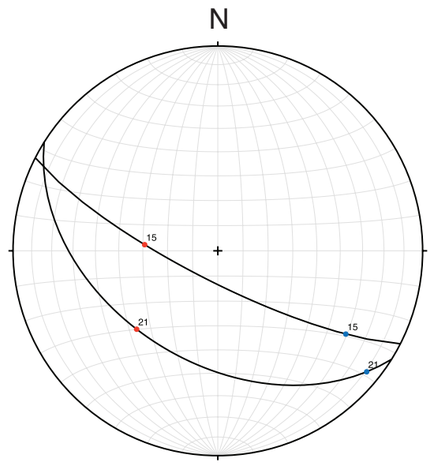

c. Fault B-Axes
n = 21

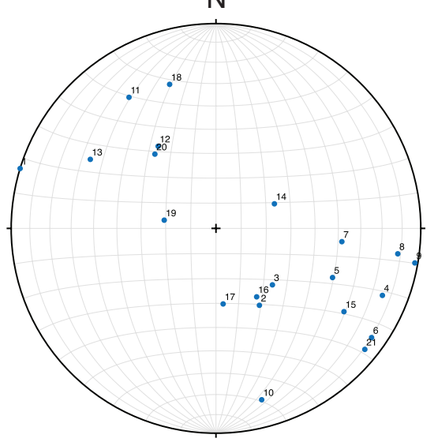

d. Faults, Large
n = xx

N

N/A

g. Other mineral filled Faults and Slickenlines
n = 8

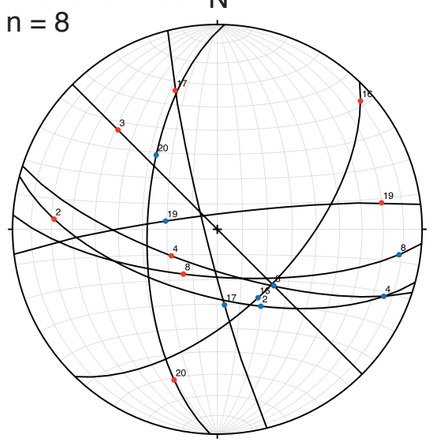

h. Epidote Faults and Slickenlines
n = 1

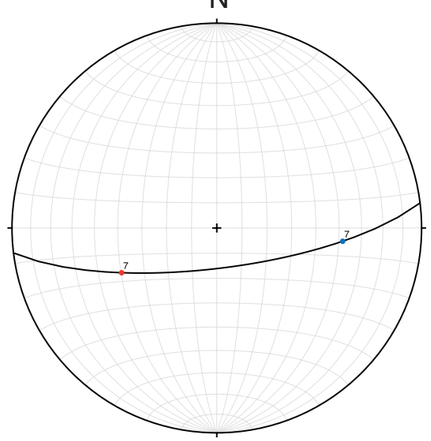

Kamb Contours, C.I. = 2 Sigma Symbols: • Slickenlines • B-axes

A-3. SB1W subsidiary fault data diagrams. The diagrams include: a) Fault poles; b) Slip vectors; c) B-axes; d) Long faults; e) Gouge and breccia zones; f) Iron-stained and/or iron-slickensided faults; g) Epidote-filled faults overprinted by iron-staining; h) Epidote-filled and/or Epidote-slickensided faults.

SB9 - All Faults

a. Fault Normals
n = 98

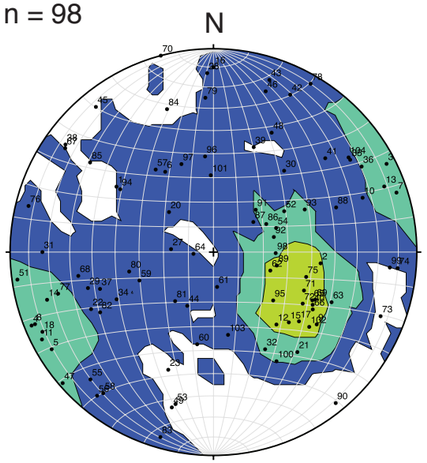

b. Fault Slip Vectors
n = 32

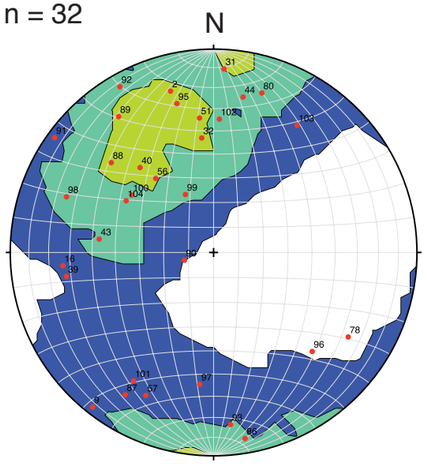

e. Gouge and Breccia Fault Normals
n = 1

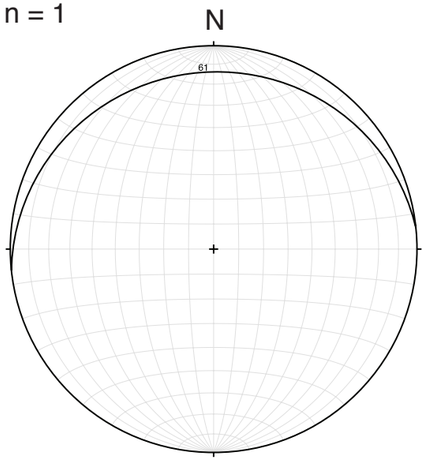

f. Fe Faults and Slickenlines
n = 12

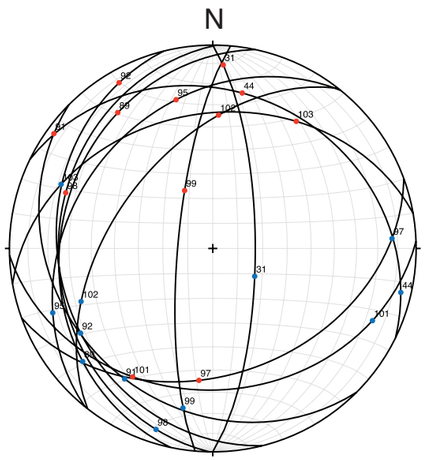

c. Fault B-Axes
n = 32

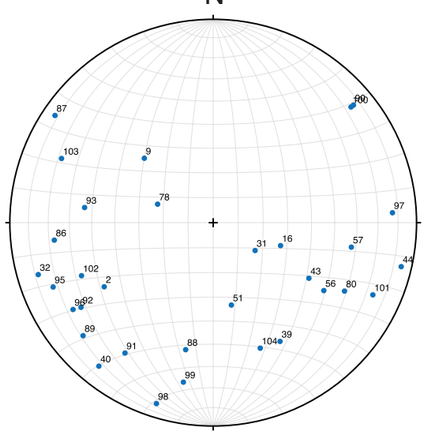

d. Faults, Large
n = 28

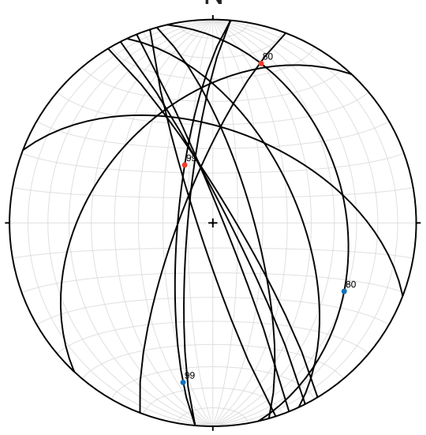

g. Epidote and Fe Faults and Slickenlines
n = xx

N

N/A

h. Epidote Faults and Slickenlines
n = xx

N

N/A

Kamb Contours, C.I. = 2 Sigma Symbols: • Slickenlines • B-axes

A-4. SB9 subsidiary fault data diagrams. The diagrams include: a) Fault poles; b) Slip vectors; c) B-axes; d) Long faults; e) Gouge and breccia zones; f) Iron-stained and/or iron-slickensided faults; g) Epidote-filled faults overprinted by iron-staining; h) Epidote-filled and/or Epidote-slickensided faults.

SB10 - All Faults

a. Fault Normals
n = 85

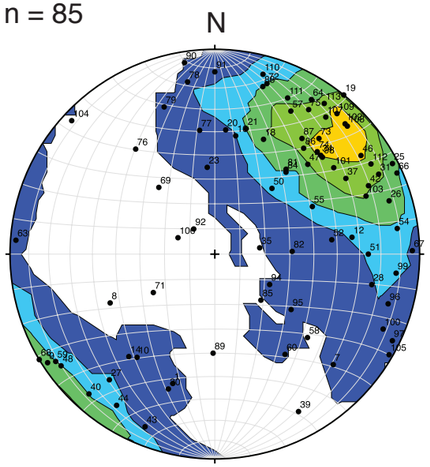

b. Fault Slip Vectors
n = 56

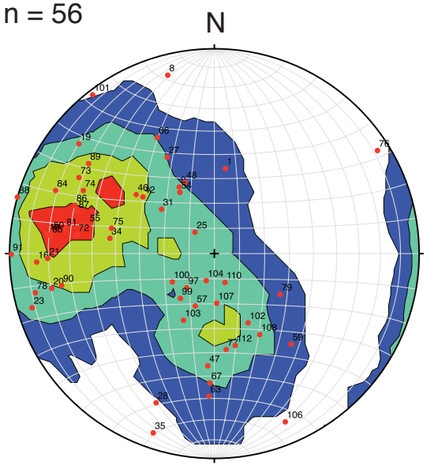

e. Gouge and Breccia Fault Normals
n = 6

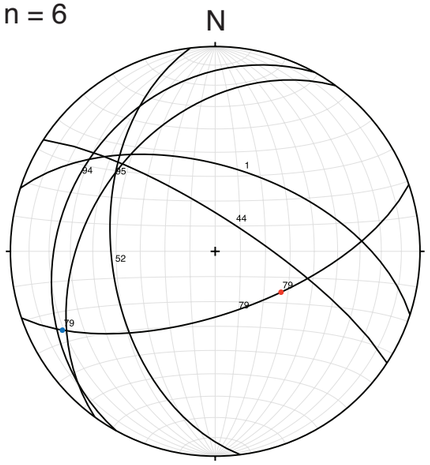

f. Fe Faults and Slickenlines
n = 10

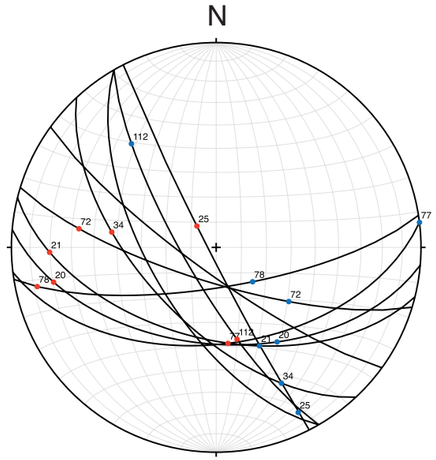

c. Fault B-Axes
n = 56

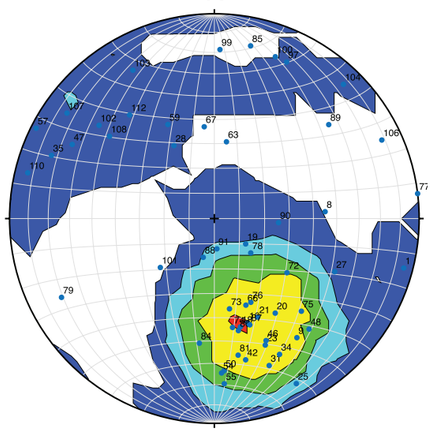

d. Faults, Large
n = 20

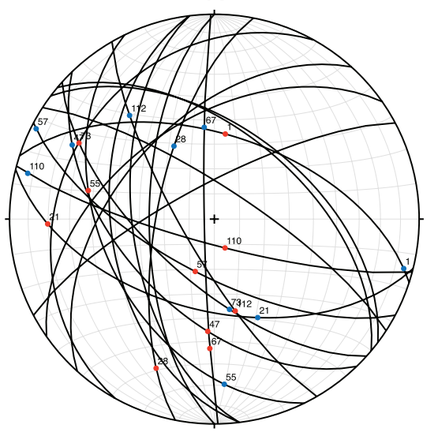

g. Epidote and Fe Faults and Slickenlines
n = 1

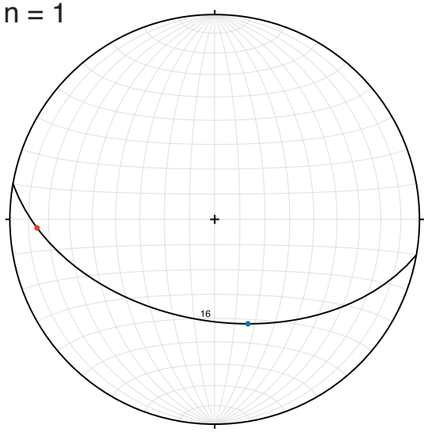

h. Epidote Faults and Slickenlines
n = xx

N/A

Kamb Contours, C.I. = 2 Sigma Symbols: • Slickenlines • B-axes

A-5. SB10 subsidiary fault data diagrams. The diagrams include: a) Fault poles; b) Slip vectors; c) B-axes; d) Long faults; e) Gouge and breccia zones; f) Iron-stained and/or iron-slickensided faults; g) Epidote-filled faults overprinted by iron-staining; h) Epidote-filled and/or Epidote-slickensided faults.

SB14-15 - All Faults

a. Fault Normals
n = 39

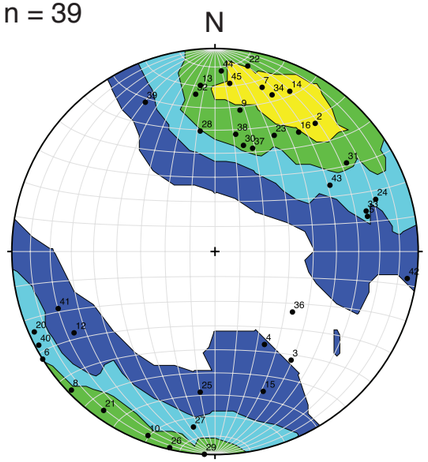

b. Fault Slip Vectors
n = 23

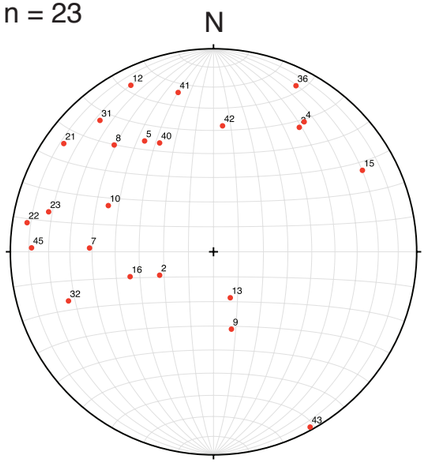

e. Gouge and Breccia Fault Normals
n = xx

N/A

f. Fe Faults and Slickenlines
n = xx

N/A

c. Fault B-Axes
n = 23

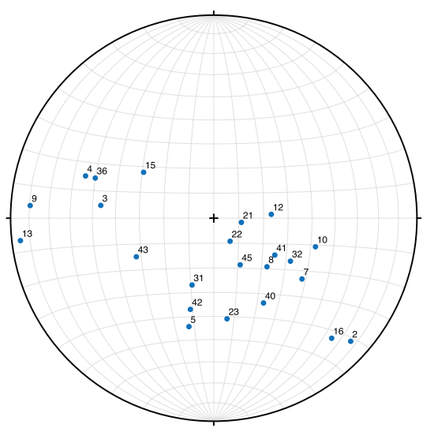

d. Faults, Large
n = 7

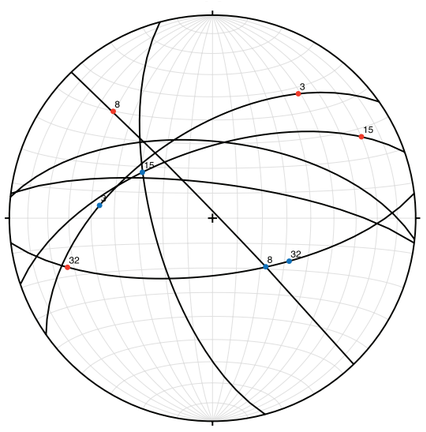

g. Epidote and Fe Faults and Slickenlines
n = xx

N/A

h. Epidote Faults and Slickenlines
n = xx

N/A

Kamb Contours, C.I. = 2 Sigma Symbols: • Slickenlines • B-axes

A-6. SB14-15 subsidiary fault data diagrams. The diagrams include: a) Fault poles; b) Slip vectors; c) B-axes; d) Long faults; e) Gouge and breccia zones; f) Iron-stained and/or iron-slickensided faults; g) Epidote-filled faults overprinted by iron-staining; h) Epidote-filled and/or Epidote-slickensided faults.

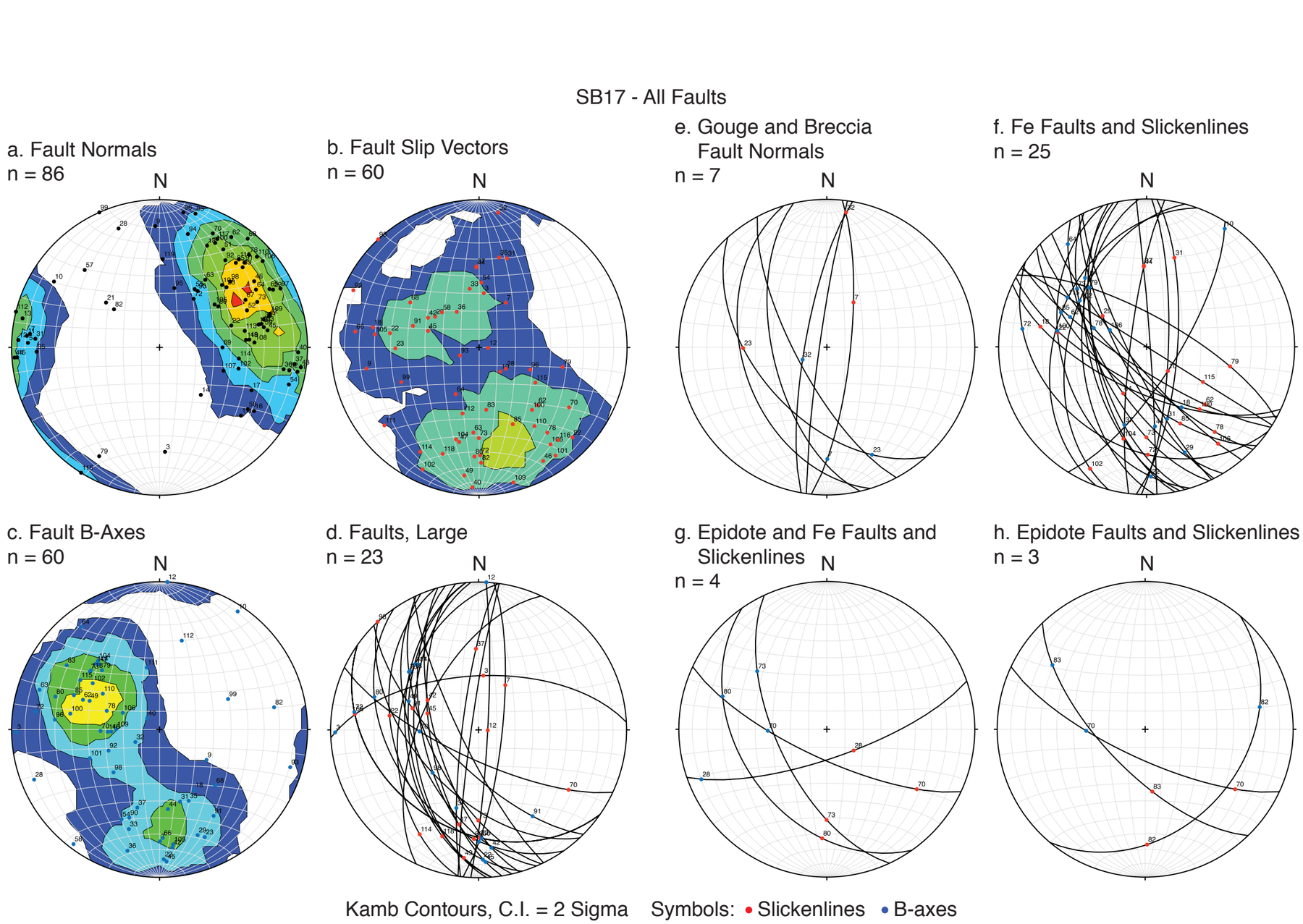

A-7. SB17 subsidiary fault data diagrams. The diagrams include: a) Fault poles; b) Slip vectors; c) B-axes; d) Long faults; e) Gouge and breccia zones; f) Iron-stained and/or iron-slickensided faults; g) Epidote-filled faults overprinted by iron-staining; h) Epidote-filled and/or Epidote-slickensided faults.

SB18 - All Faults

a. Fault Normals
n = 121

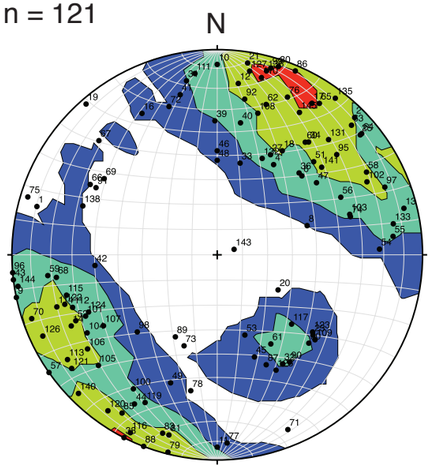

b. Fault Slip Vectors
n = 83

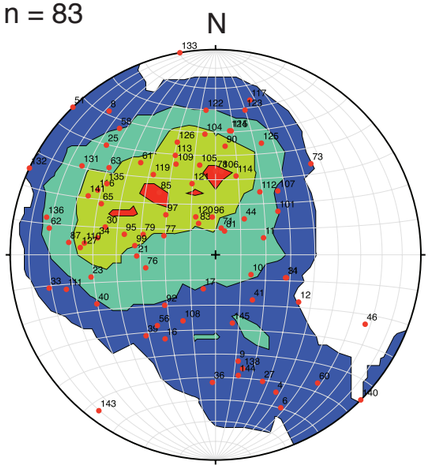

e. Gouge and Breccia Fault Normals
n = 7

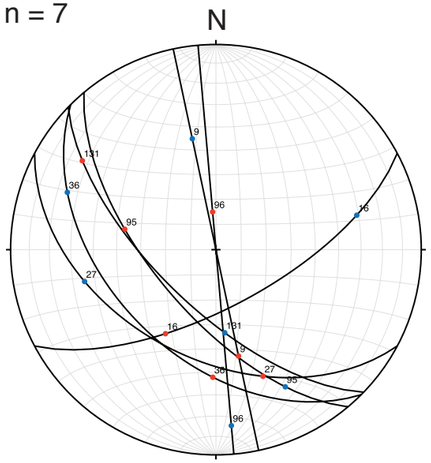

f. Fe Faults and Slickenlines
n = xx

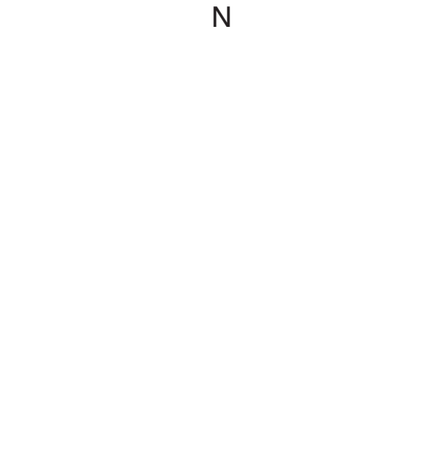

c. Fault B-Axes
n = 83

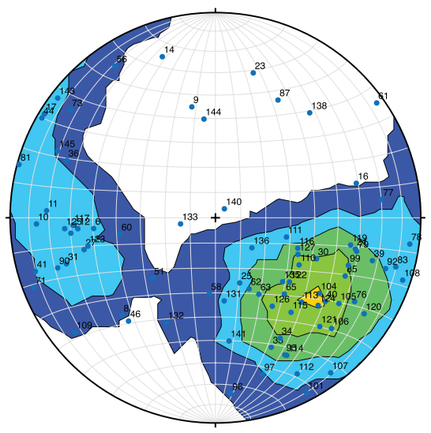

d. Faults, Large
n = 34

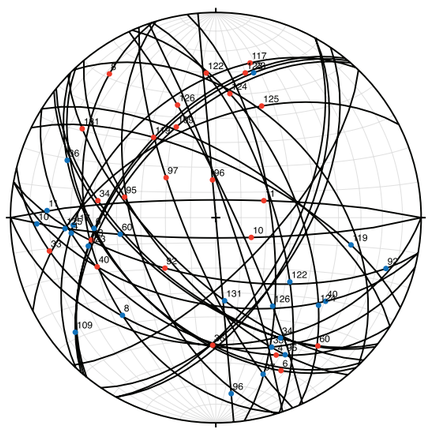

g. Epidote and Fe Faults and Slickenlines
n = 1

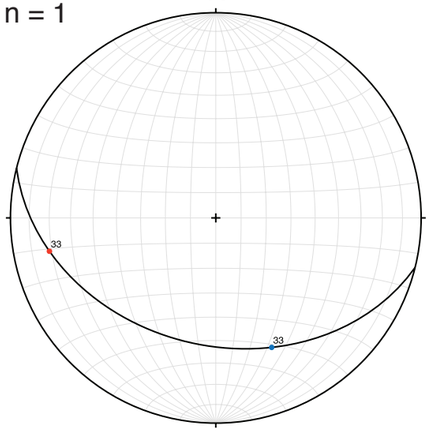

h. Epidote Faults and Slickenlines
n = 33

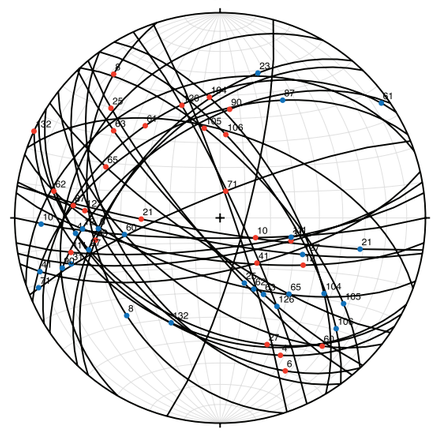

Kamb Contours, C.I. = 2 Sigma Symbols: • Slickenlines • B-axes

A-8. SB18 subsidiary fault data diagrams. The diagrams include: a) Fault poles; b) Slip vectors; c) B-axes; d) Long faults; e) Gouge and breccia zones; f) Iron-stained and/or iron-slickensided faults; g) Epidote-filled faults overprinted by iron-staining; h) Epidote-filled and/or Epidote-slickensided faults.

SB33 - All Faults

a. Fault Normals
n = 38

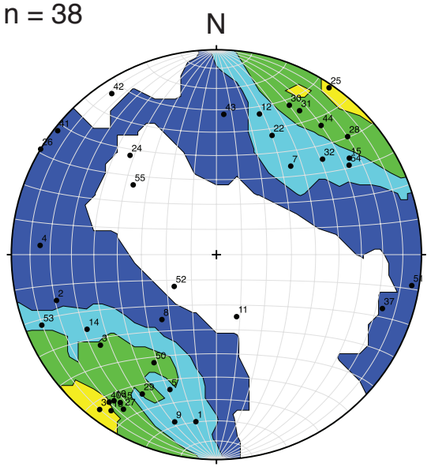

b. Fault Slip Vectors
n = 15

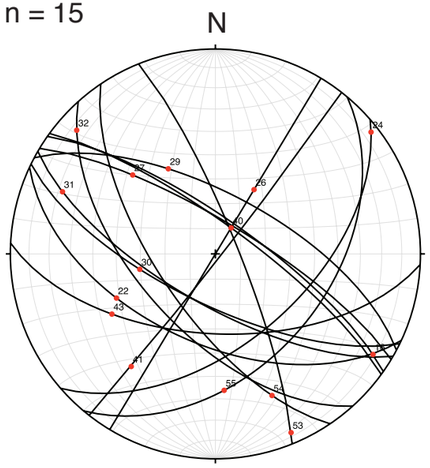

e. Gouge and Breccia Fault Normals
n = 12

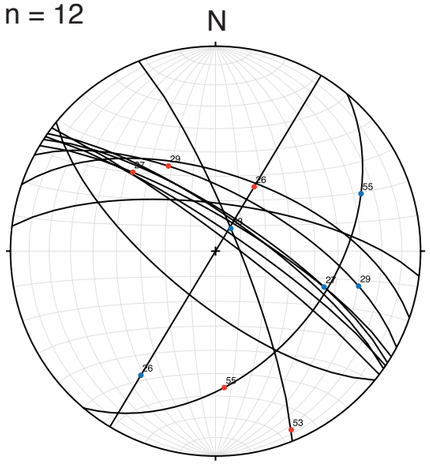

f. Fe Faults and Slickenlines
n = 5

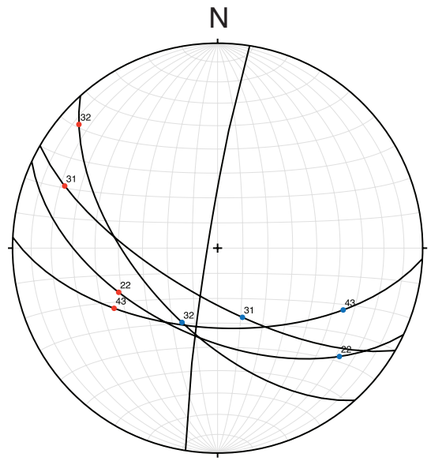

c. Fault B-Axes
n = 15

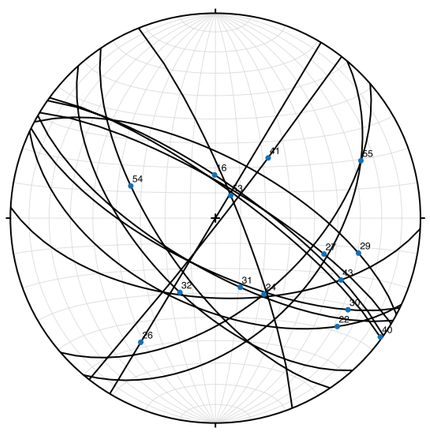

d. Faults, Large
n = 9

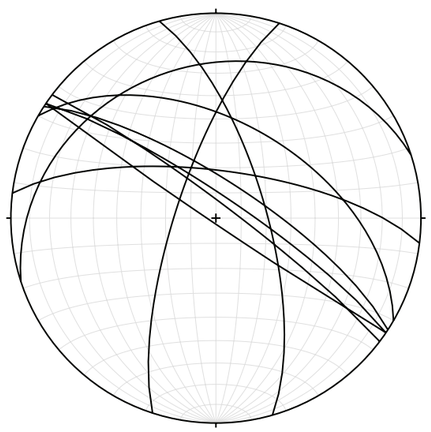

g. Epidote and Fe Faults and Slickenlines
n = xx

N/A

h. Epidote Faults and Slickenlines
n = 1

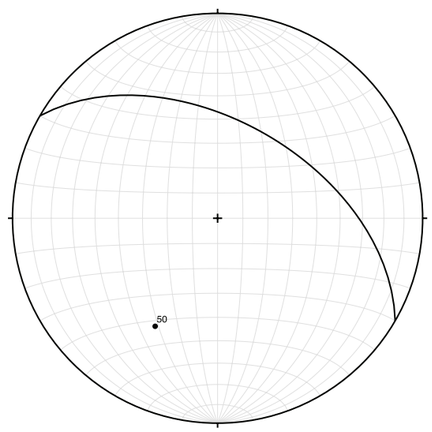

Kamb Contours, C.I. = 2 Sigma Symbols: • Slickenlines • B-axes

A-9. SB33 subsidiary fault data diagrams. The diagrams include: a) Fault poles; b) Slip vectors; c) B-axes; d) Long faults; e) Gouge and breccia zones; f) Iron-stained and/or iron-slickensided faults; g) Epidote-filled faults overprinted by iron-staining; h) Epidote-filled and/or Epidote-slickensided faults.

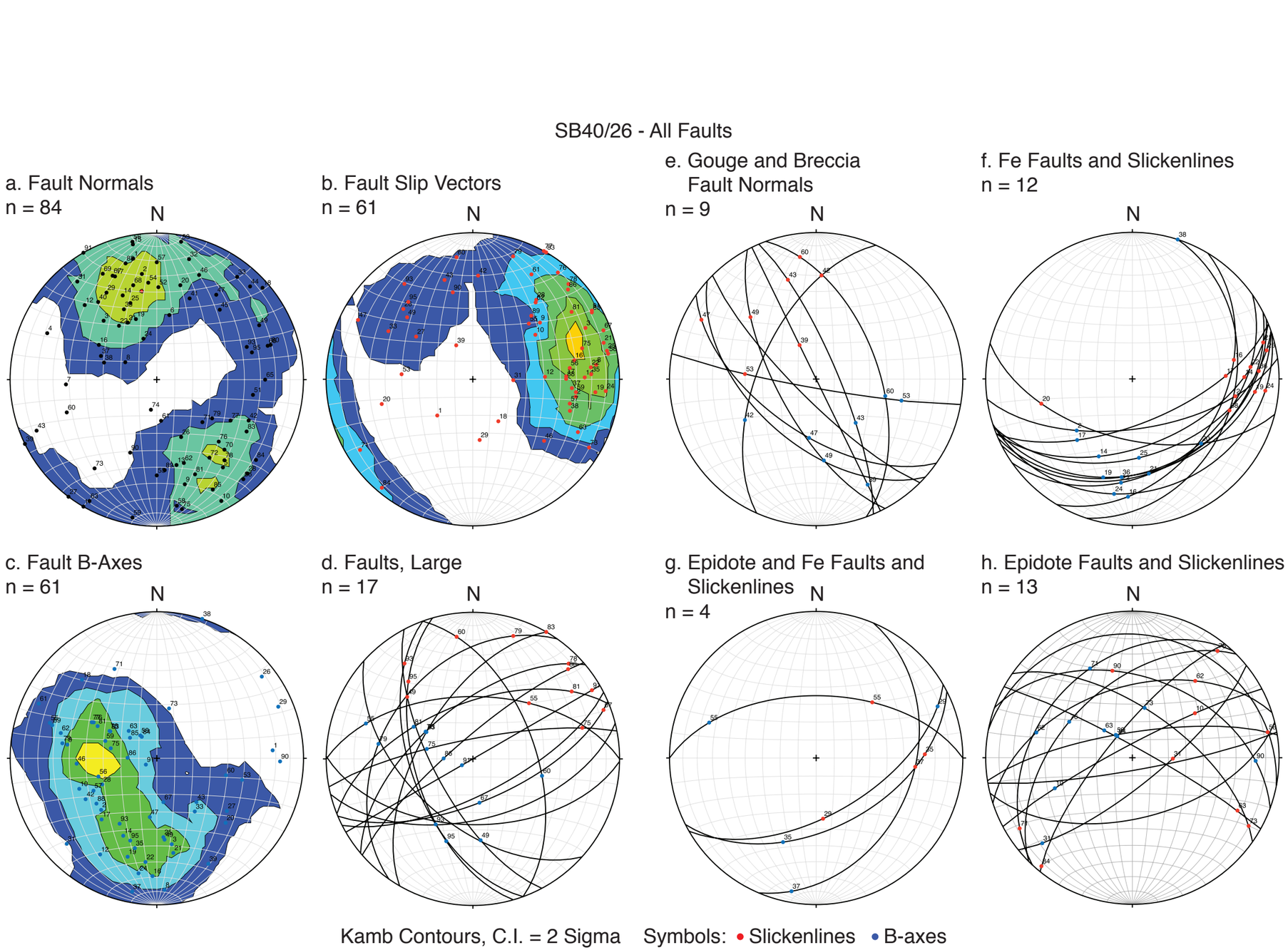

A-10. SB40/26 subsidiary fault data diagrams. The diagrams include: a) Fault poles; b) Slip vectors; c) B-axes; d) Long faults; e) Gouge and breccia zones; f) Iron-stained and/or iron-slickensided faults; g) Epidote-filled faults overprinted by iron-staining; h) Epidote-filled and/or Epidote-slickensided faults.

SB41/27 - All Faults

a. Fault Normals
n = 61

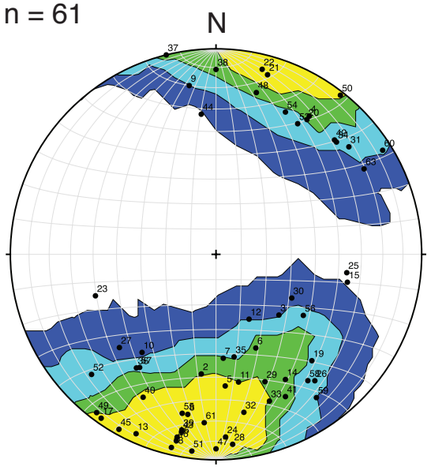

b. Fault Slip Vectors
n = 50

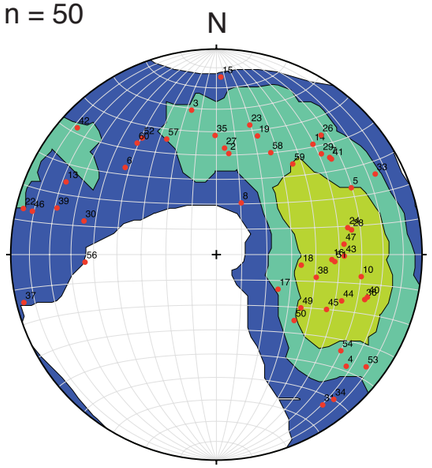

e. Gouge and Breccia Fault Normals
n = 10

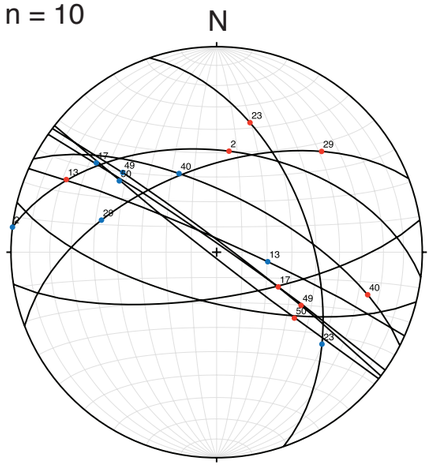

f. Fe Faults and Slickenlines
n = xx

N/A

c. Fault B-Axes
n = 50

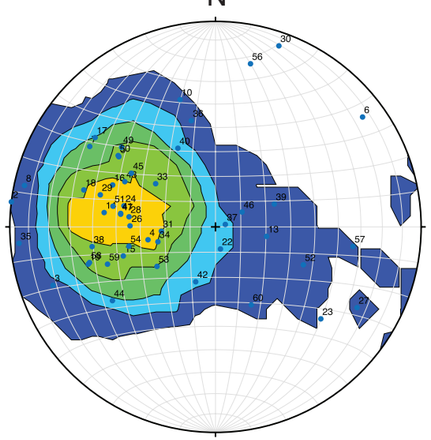

d. Faults, Large
n = 9

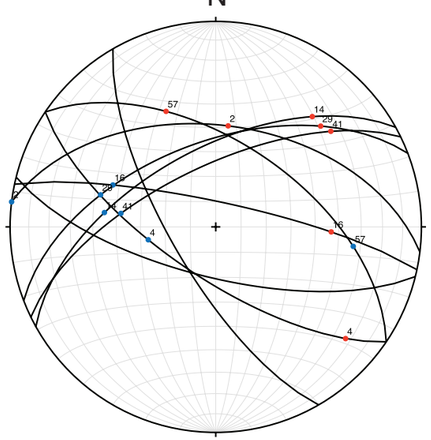

g. Epidote and Fe Faults and Slickenlines
n = xx

N/A

h. Epidote Faults and Slickenlines
n =11

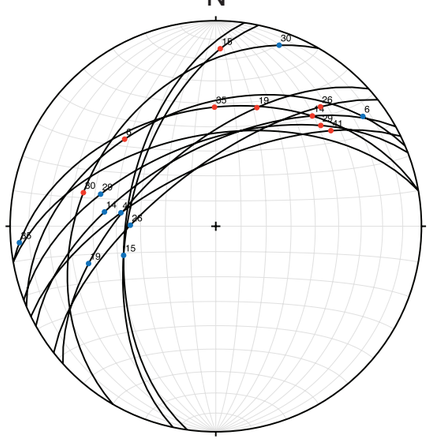

Kamb Contours, C.I. = 2 Sigma Symbols: • Slickenlines • B-axes

A-11. SB41/27 subsidiary fault data diagrams. The diagrams include: a) Fault poles; b) Slip vectors; c) B-axes; d) Long faults; e) Gouge and breccia zones; f) Iron-stained and/or iron-slickensided faults; g) Epidote-filled faults overprinted by iron-staining; h) Epidote-filled and/or Epidote-slickensided faults.

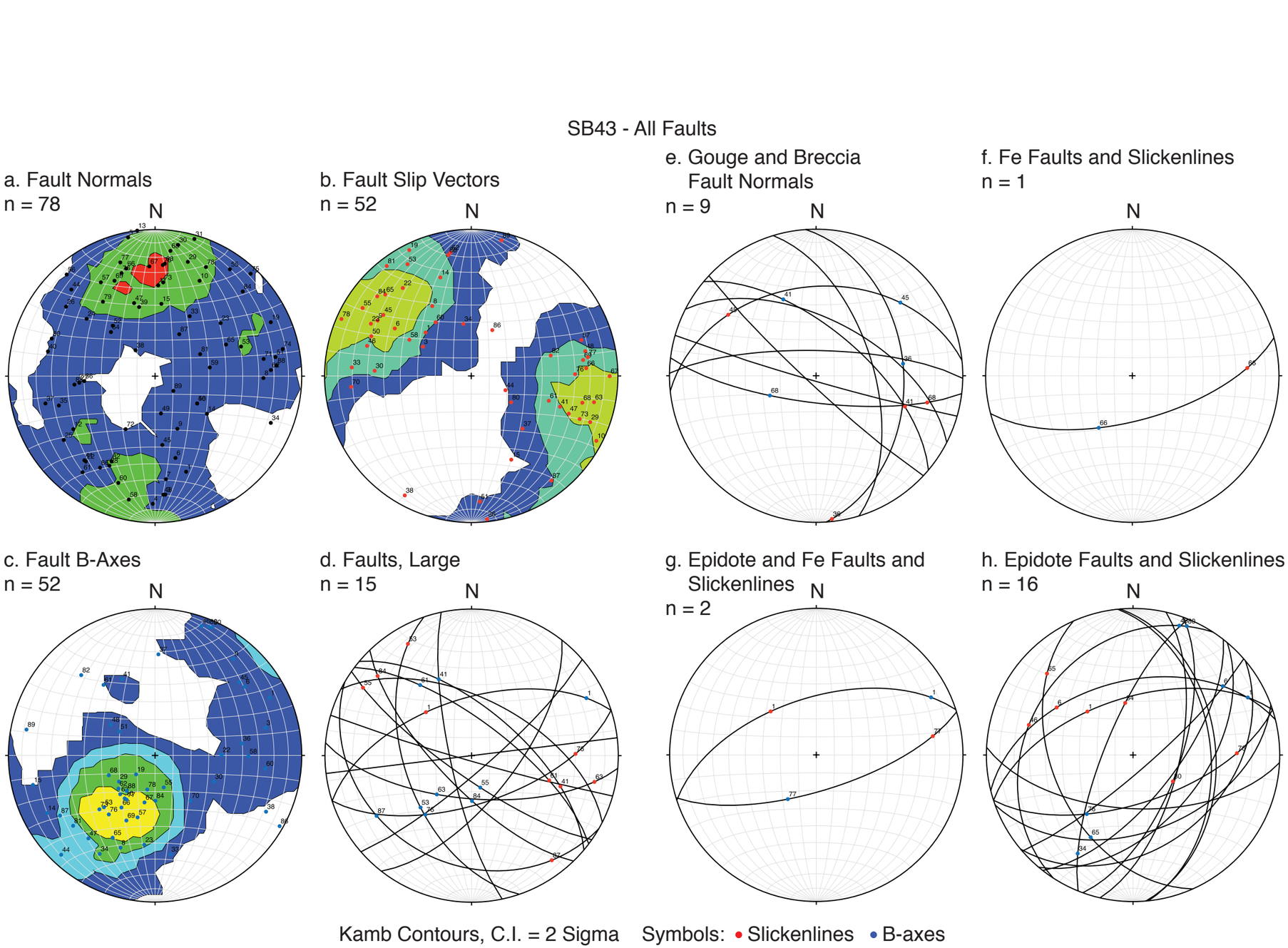

A-12. SB43 subsidiary fault data diagrams. The diagrams include: a) Fault poles; b) Slip vectors; c) B-axes; d) Long faults; e) Gouge and breccia zones; f) Iron-stained and/or iron-slickensided faults; g) Epidote-filled faults overprinted by iron-staining; h) Epidote-filled and/or Epidote-slickensided faults.

SB44 - All Faults

a. Fault Normals
n = 48

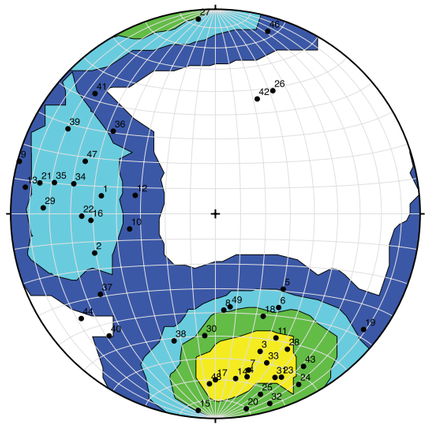

b. Fault Slip Vectors
n = 28

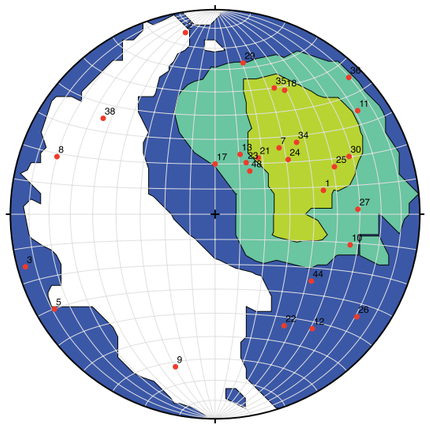

e. Gouge and Breccia Fault Normals
n = 8

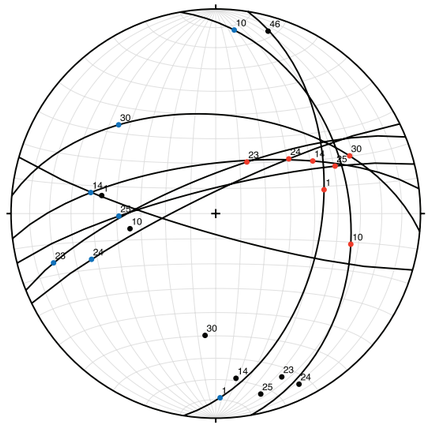

f. Fe Faults and Slickenlines
n = xx

N/A

c. Fault B-Axes
n = 28

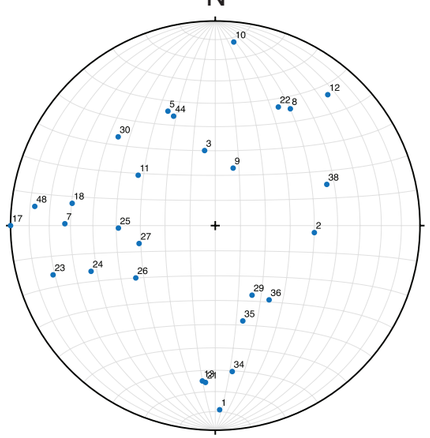

d. Faults, Large
n = 10

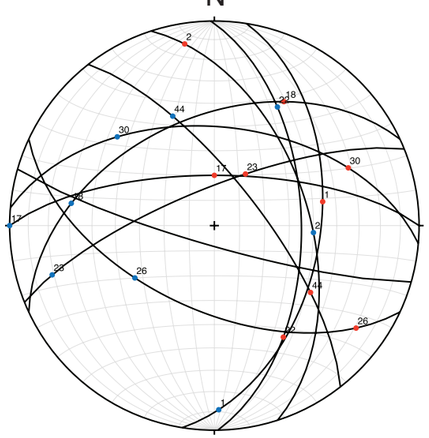

g. Epidote and Fe Faults and Slickenlines
n = xx

N/A

h. Epidote Faults and Slickenlines
n = 19

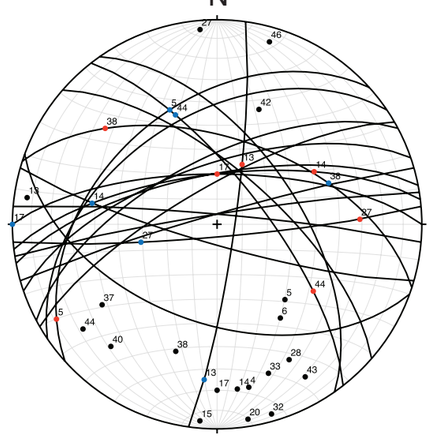

Kamb Contours, C.I. = 2 Sigma Symbols: • Slickenlines • B-axes

A-13. SB44 subsidiary fault data diagrams. The diagrams include: a) Fault poles; b) Slip vectors; c) B-axes; d) Long faults; e) Gouge and breccia zones; f) Iron-stained and/or iron-slickensided faults; g) Epidote-filled faults overprinted by iron-staining; h) Epidote-filled and/or Epidote-slickensided faults.

SB46 - All Faults

a. Fault Normals
n = 22

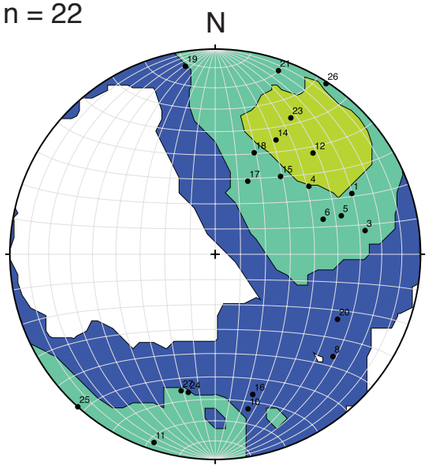

b. Fault Slip Vectors
n = 7

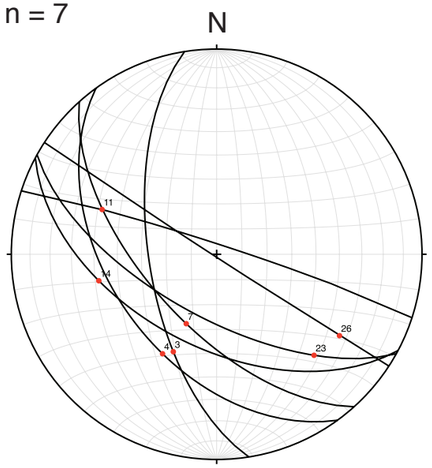

e. Gouge and Breccia Fault Normals
n = 5

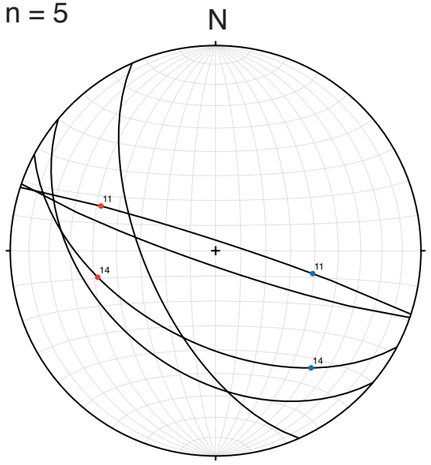

f. Fe Faults and Slickenlines
n = 1

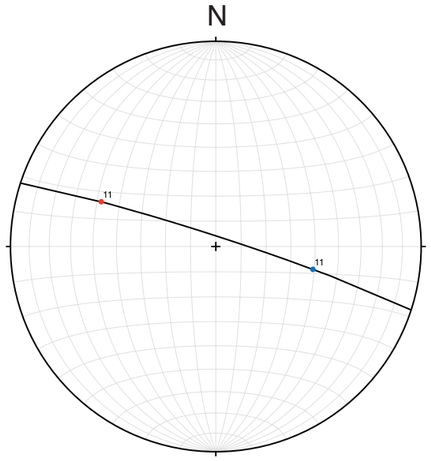

c. Fault B-Axes
n = 7

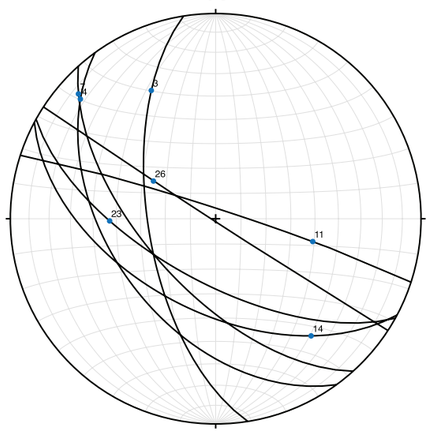

d. Faults, Large
n = 9

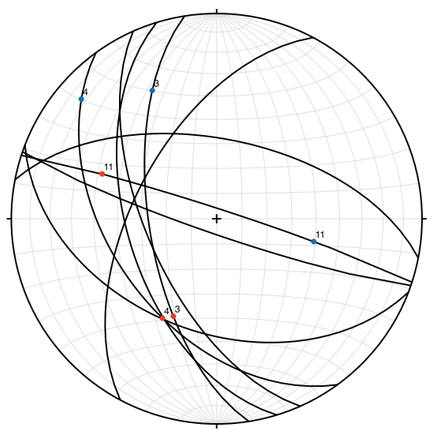

g. Epidote and Fe Faults and Slickenlines
n = xx

N/A

h. Epidote Faults and Slickenlines
n = xx

N/A

Kamb Contours, C.I. = 2 Sigma Symbols: • Slickenlines • B-axes

A-14. SB46 subsidiary fault data diagrams. The diagrams include: a) Fault poles; b) Slip vectors; c) B-axes; d) Long faults; e) Gouge and breccia zones; f) Iron-stained and/or iron-slickensided faults; g) Epidote-filled faults overprinted by iron-staining; h) Epidote-filled and/or Epidote-slickensided faults.

SB53 - All Faults

a. Fault Normals
n = 12

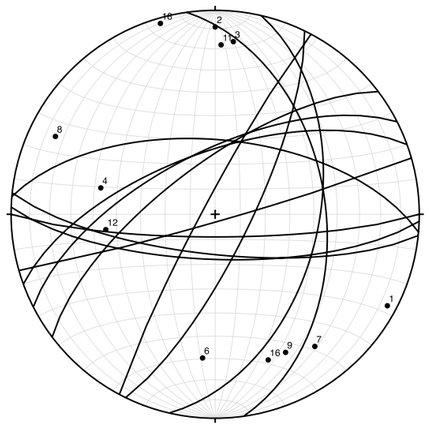

b. Fault Slip Vectors
n = 4

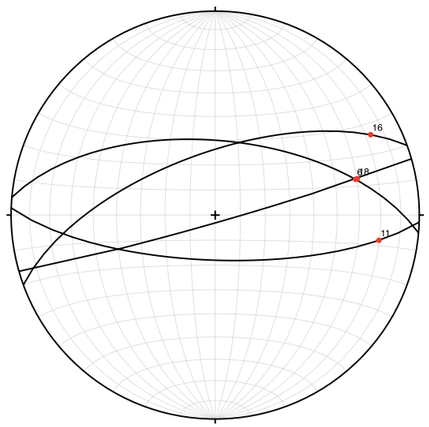

e. Gouge and Breccia Fault Normals
n = 3

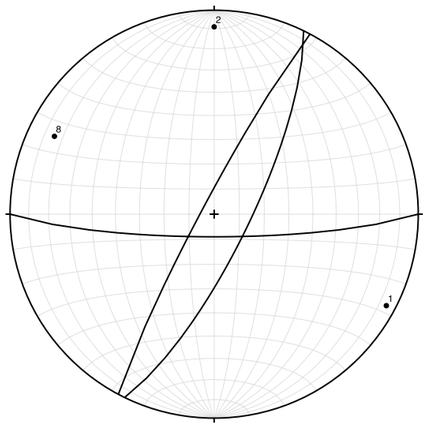

f. Fe Faults and Slickenlines
n = xx

N/A

c. Fault B-Axes
n = 4

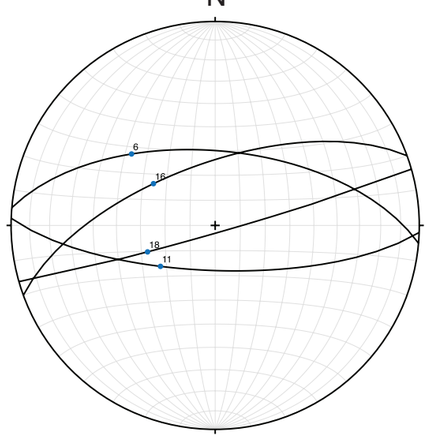

d. Faults, Large
n = 2

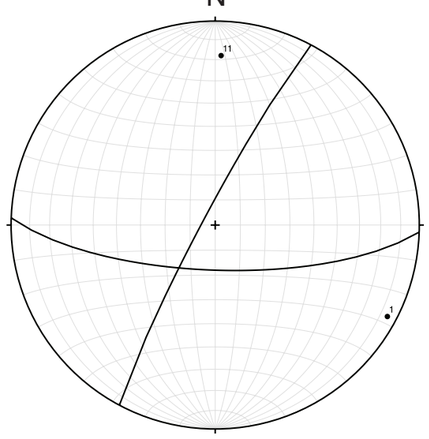

g. Epidote and Fe Faults and Slickenlines
n = xx

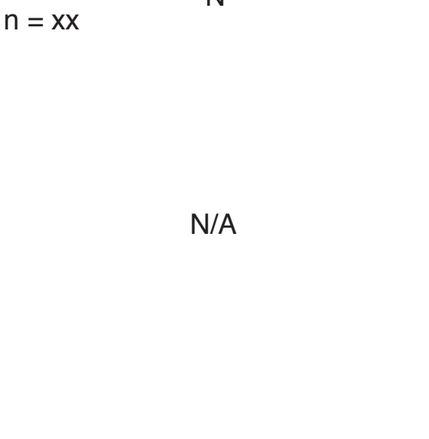

N/A

h. Epidote Faults and Slickenlines
n = xx

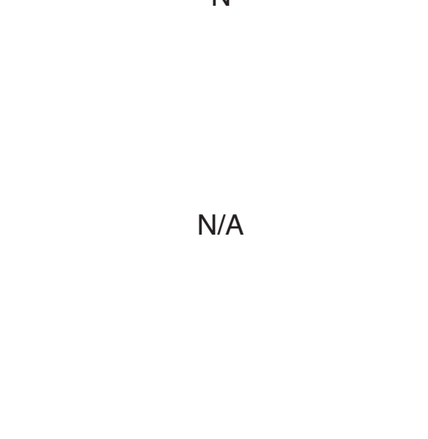

N/A

Kamb Contours, C.I. = 2 Sigma Symbols: • Slickenlines • B-axes

A-15. SB53 subsidiary fault data diagrams. The diagrams include: a) Fault poles; b) Slip vectors; c) B-axes; d) Long faults; e) Gouge and breccia zones; f) Iron-stained and/or iron-slickensided faults; g) Epidote-filled faults overprinted by iron-staining; h) Epidote-filled and/or Epidote-slickensided faults.

SB54 - All Faults

a. Fault Normals
n = 18

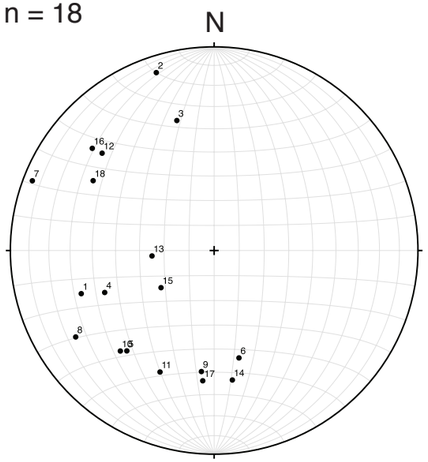

b. Fault Slip Vectors
n = 15

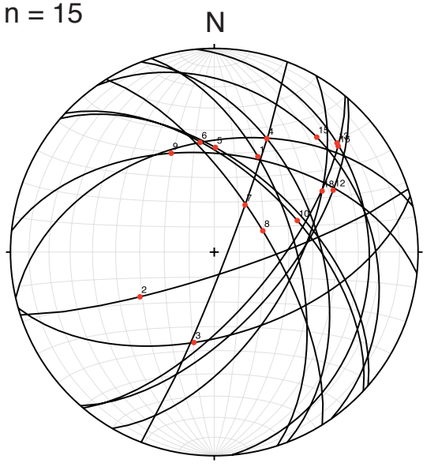

e. Gouge and Breccia Fault Normals
n = xx

N/A

f. Fe Faults and Slickenlines
n = 1

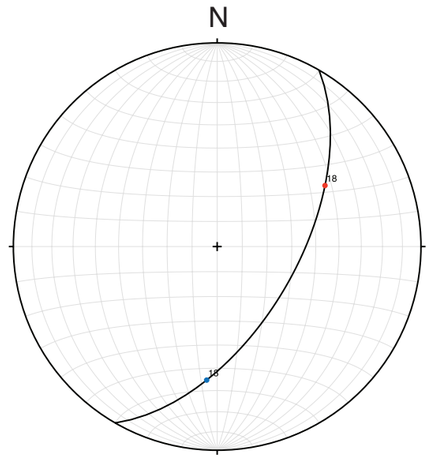

c. Fault B-Axes
n = 15

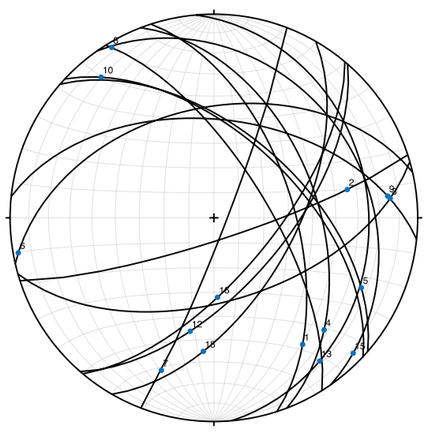

d. Faults, Large
n = 5

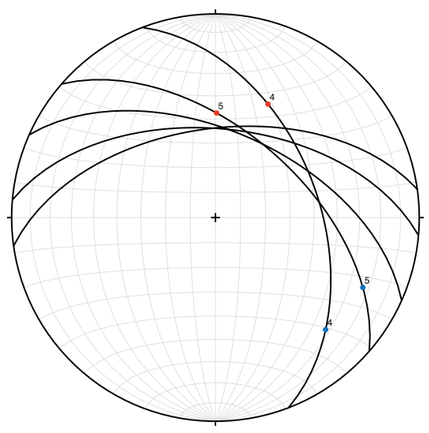

g. Epidote and Fe Faults and Slickenlines
n = 6

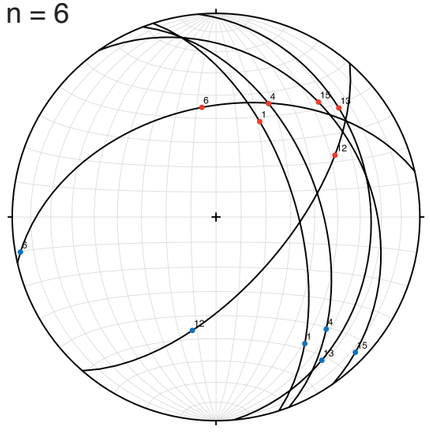

h. Epidote Faults and Slickenlines
n = 7

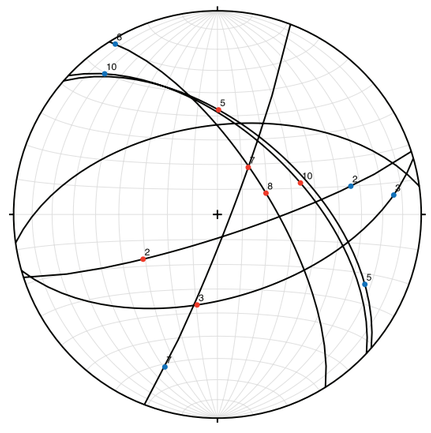

Kamb Contours, C.I. = 2 Sigma Symbols: • Slickenlines • B-axes

A-16. SB54 subsidiary fault data diagrams. The diagrams include: a) Fault poles; b) Slip vectors; c) B-axes; d) Long faults; e) Gouge and breccia zones; f) Iron-stained and/or iron-slickensided faults; g) Epidote-filled faults overprinted by iron-staining; h) Epidote-filled and/or Epidote-slickensided faults.

SB56 - All Faults

a. Fault Normals
n = 8

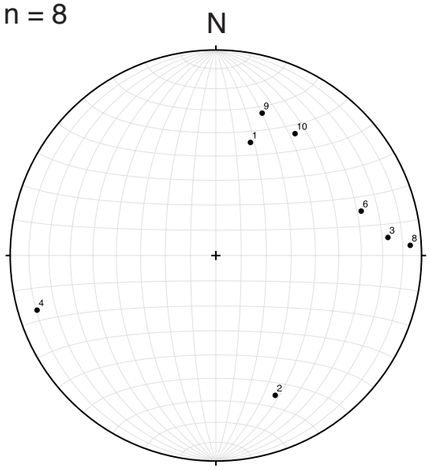

b. Fault Slip Vectors
n = 8

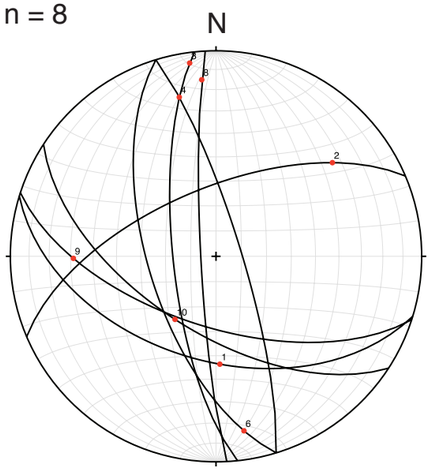

e. Gouge and Breccia Fault Normals
n = xx

N

N/A

f. Fe Faults and Slickenlines
n = 4

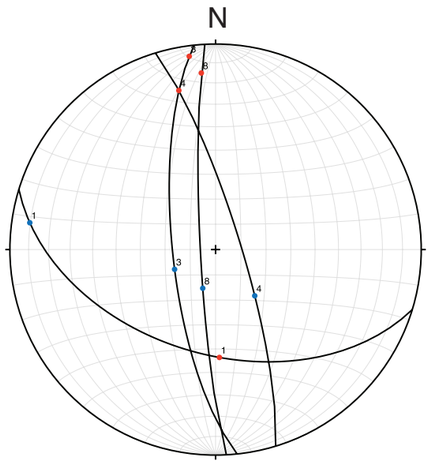

c. Fault B-Axes

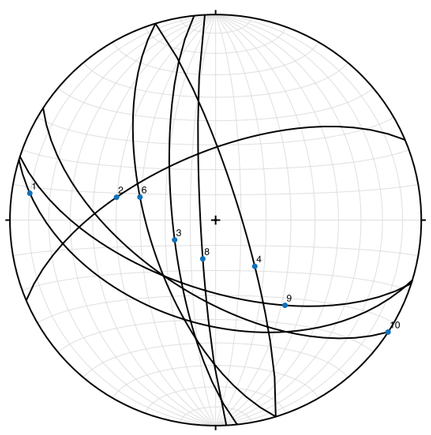

d. Faults, Large
n = 1

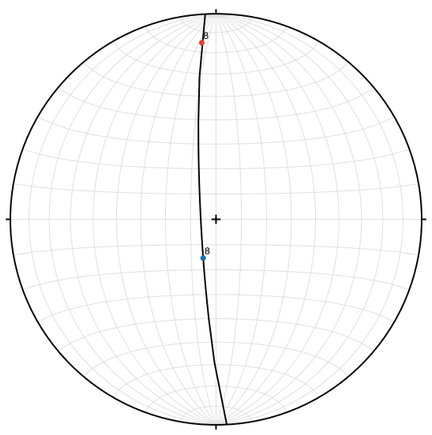

g. Epidote and Fe Faults and Slickenlines
n = xx

N

N/A

h. Epidote Faults and Slickenlines
n = 2

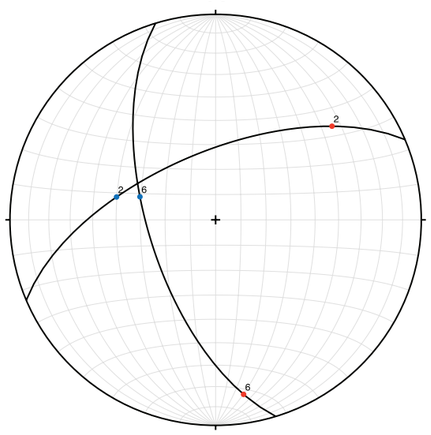

Kamb Contours, C.I. = 2 Sigma Symbols: • Slickenlines • B-axes

A-17. SB56 subsidiary fault data diagrams. The diagrams include: a) Fault poles; b) Slip vectors; c) B-axes; d) Long faults; e) Gouge and breccia zones; f) Iron-stained and/or iron-slickensided faults; g) Epidote-filled faults overprinted by iron-staining; h) Epidote-filled and/or Epidote-slickensided faults.

SB61-62-63-64 - All Faults

a. Fault Normals
n = 29

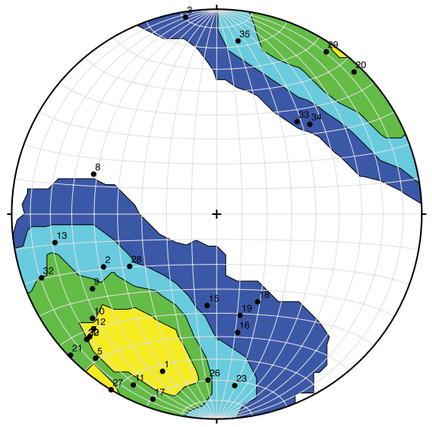

b. Fault Slip Vectors
n = 28

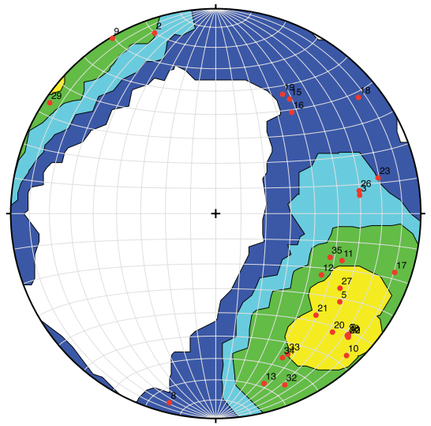

c. Fault B-Axes
n = 28

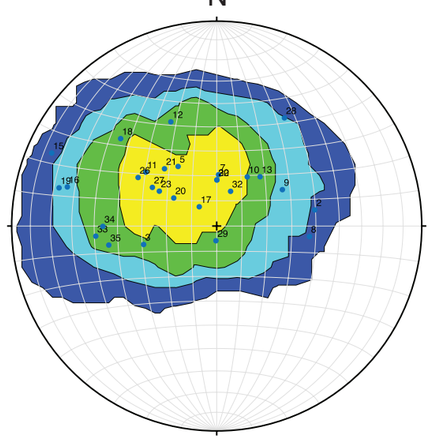

d. Faults, Large
n = xx

N

N/A

e. Gouge and Breccia Fault Normals
n = xx

N

N/A

f. Fe Faults and Slickenlines
n = xx

N

N/A

g. Epidote and Fe Faults and Slickenlines
n = xx

N

N/A

h. Epidote Faults and Slickenlines
n = xx

N

N/A

Kamb Contours, C.I. = 2 Sigma Symbols: • Slickenlines • B-axes

A-18. SB61-62-63-64 subsidiary fault data diagrams. The diagrams include: a) Fault poles; b) Slip vectors; c) B-axes; d) Long faults; e) Gouge and breccia zones; f) Iron-stained and/or iron-slickensided faults; g) Epidote-filled faults overprinted by iron-staining; h) Epidote-filled and/or Epidote-slickensided faults.

SB67-68 - All Faults

a. Fault Normals
n = 11

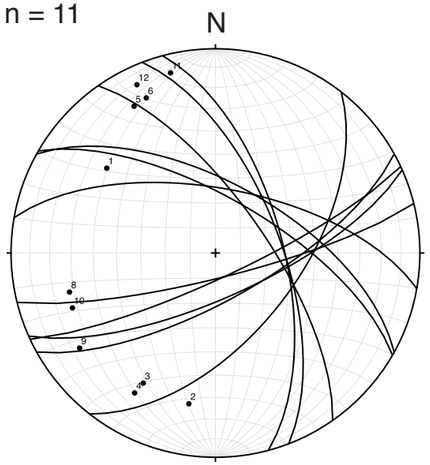

b. Fault Slip Vectors
n = 1

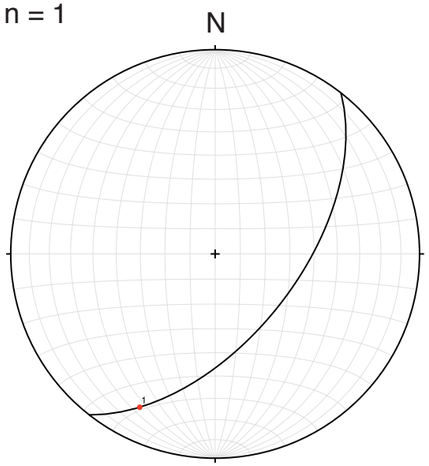

e. Gouge and Breccia Fault Normals
n = xx

N

N/A

f. Fe Faults and Slickenlines
n = xx

N

N/A

c. Fault B-Axes
n = 1

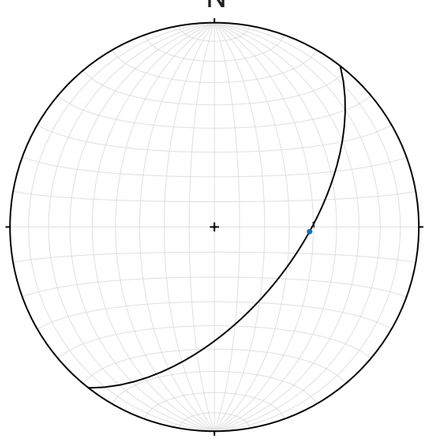

d. Faults, Large
n = xx

N

N/A

g. Epidote and Fe Faults and Slickenlines
n = xx

N

N/A

h. Epidote Faults and Slickenlines
n = 1

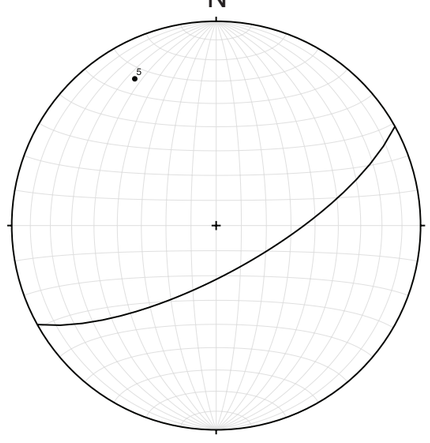

Kamb Contours, C.I. = 2 Sigma Symbols: • Slickenlines • B-axes

A-19. SB67-68 subsidiary fault data diagrams. The diagrams include: a) Fault poles; b) Slip vectors; c) B-axes; d) Long faults; e) Gouge and breccia zones; f) Iron-stained and/or iron-slickensided faults; g) Epidote-filled faults overprinted by iron-staining; h) Epidote-filled and/or Epidote-slickensided faults.

APPENDIX B

FIGURES

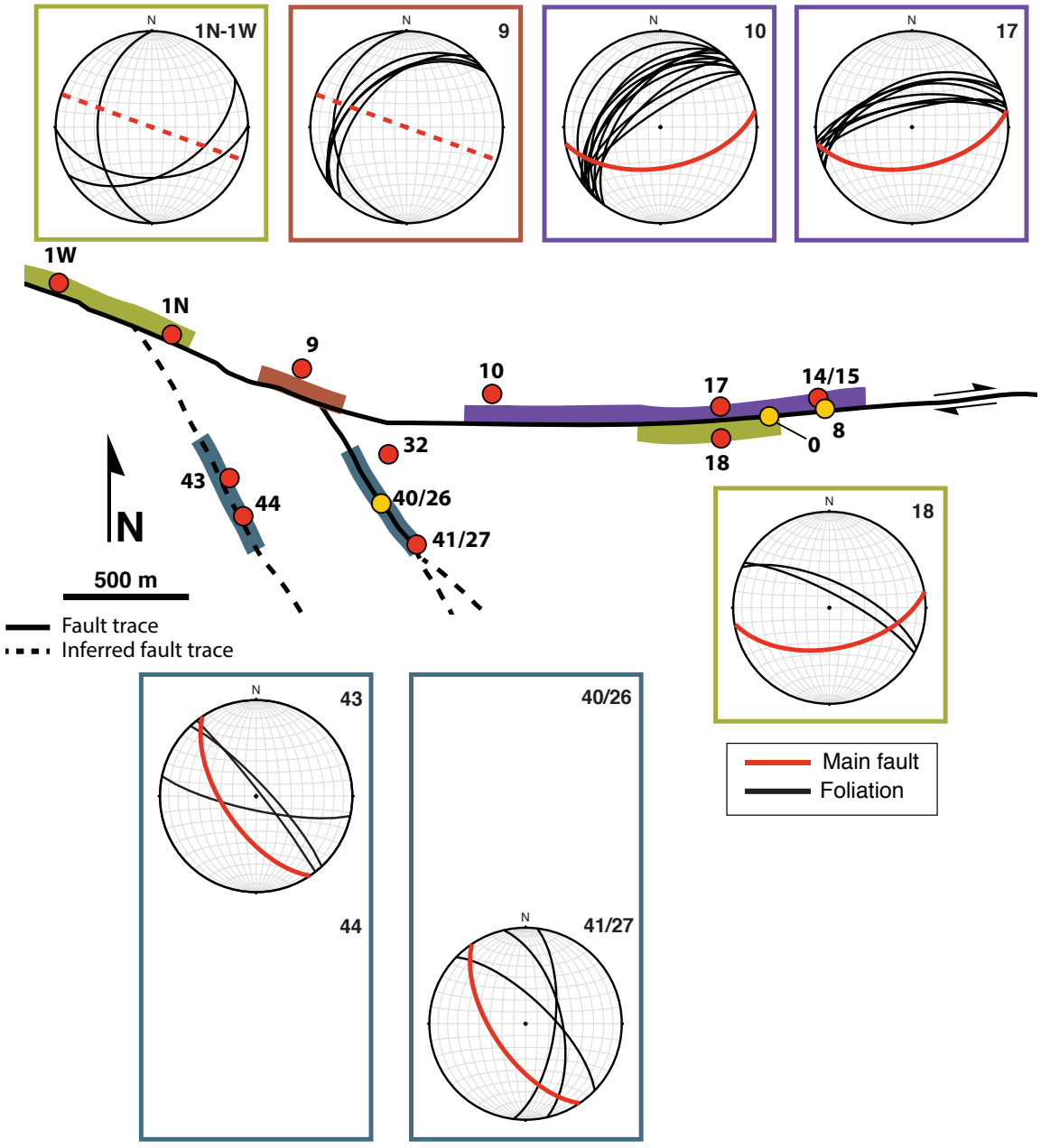

B-1. Distribution of foliation orientations in structural domains within the Mill Creek Canyon region.

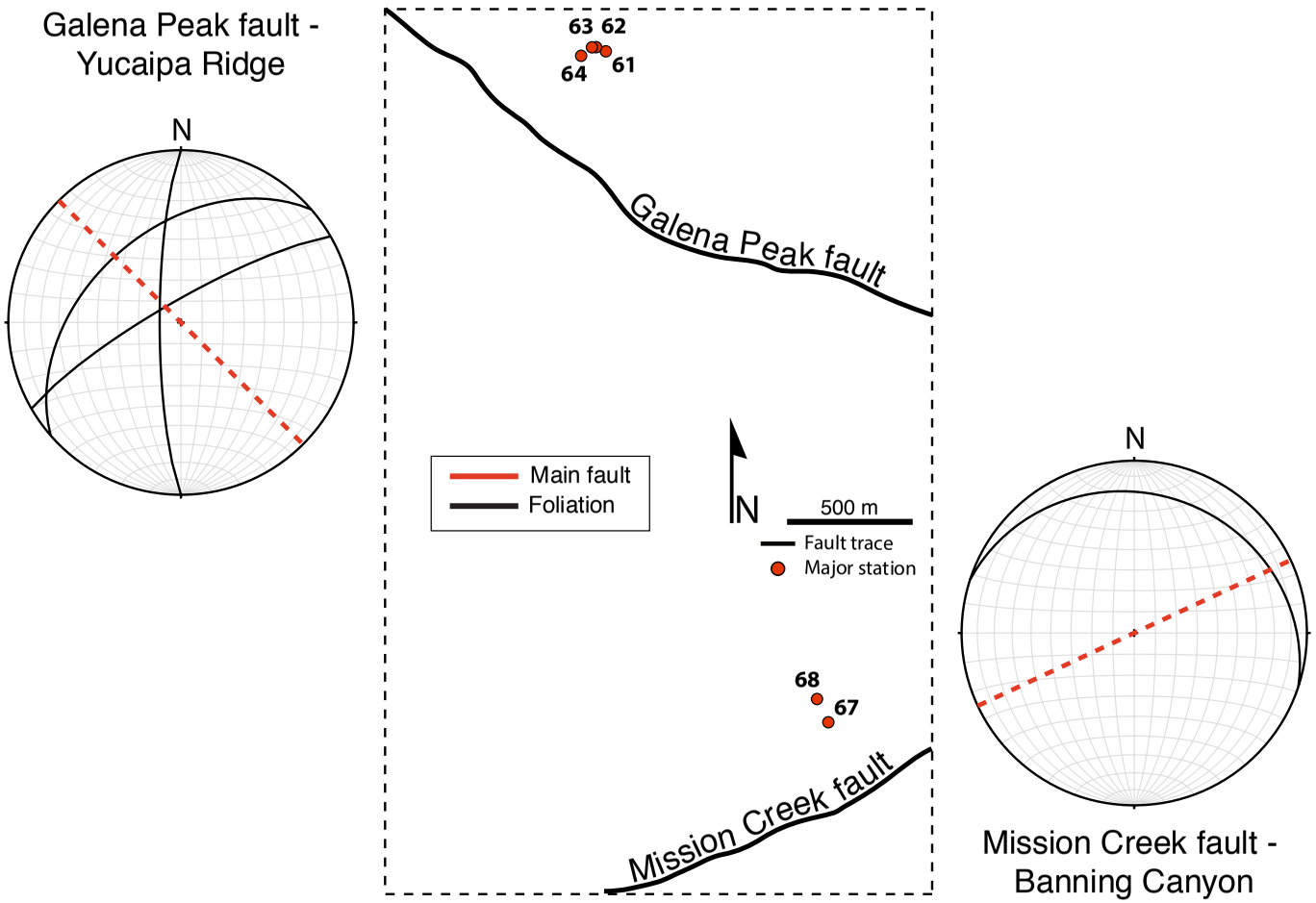

B-2. Distribution of foliation orientations in structural domains within the Yucaipa Ridge region.

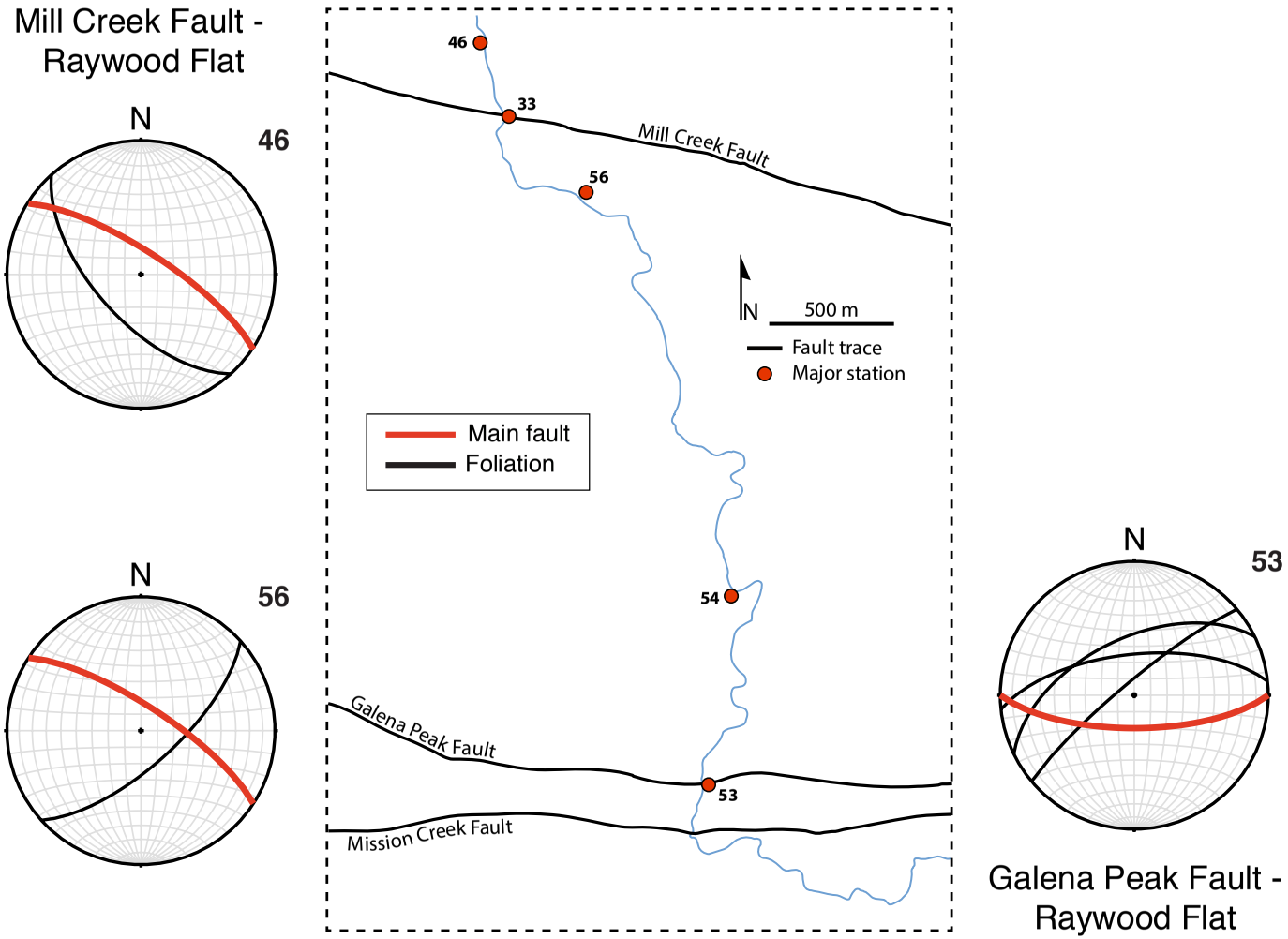

B-3. Distribution of foliation orientations in structural domains within the Raywood Flat region.

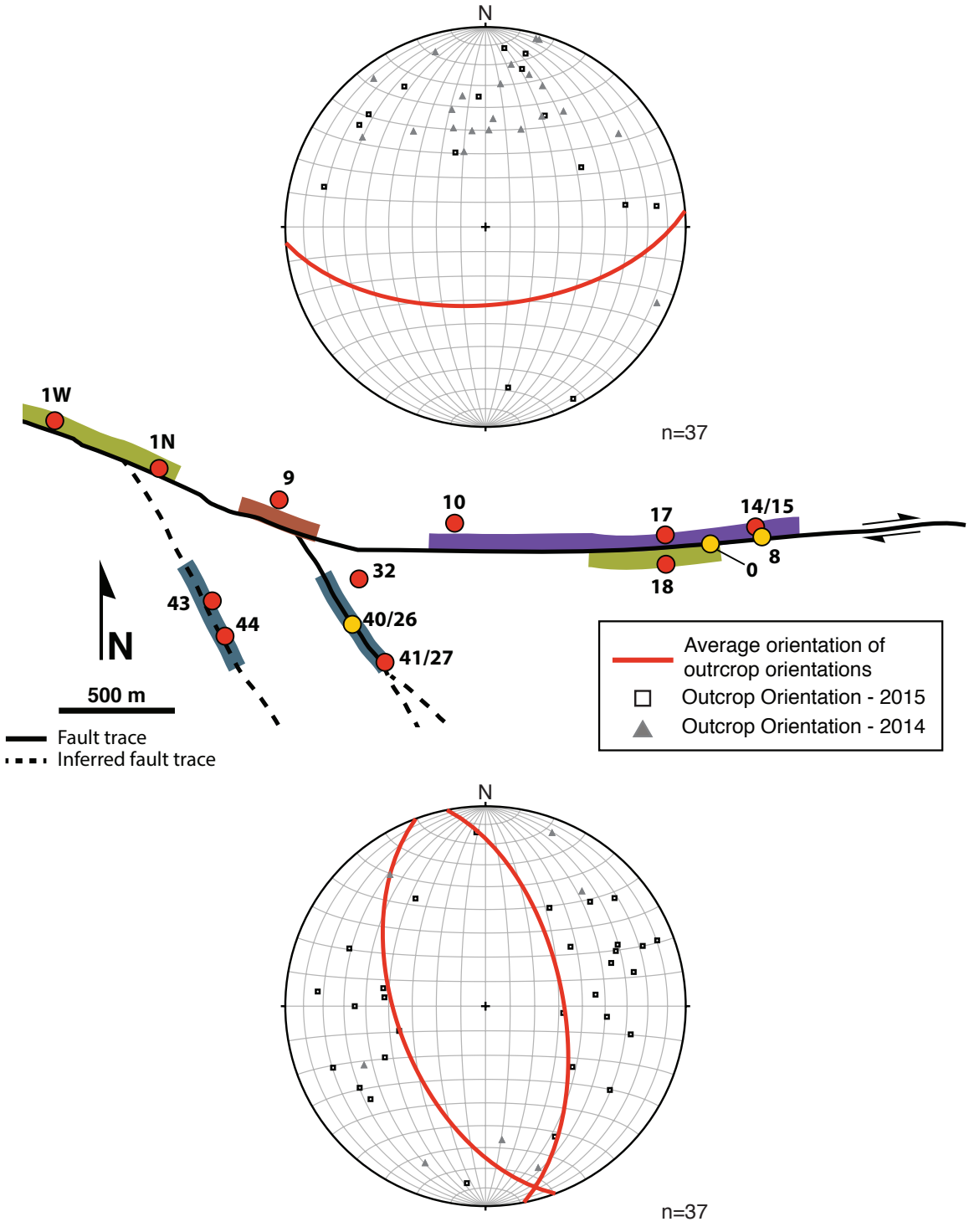

B-4. Distribution of outcrop orientations in the Mill Creek Canyon region. Outcrop orientations for the north (top) and south side of the fault (bottom).